UNIVERSITÀ DEGLI STUDI DI NAPOLI
"FEDERICO II"

DIPARTIMENTO DI FISICA

INTERNATIONAL PhD SCHOOL IN NOVEL TECHNOLOGIES FOR MATERIALS, SENSORS AND IMAGING

XXVIII COURSE

A reliable Raman-spectroscopy-based approach for diagnosis, classification and follow-up of B-cell acute lymphoblastic leukemia

Stefano Managò

TUTOR: Anna Chiara De Luca

ACADEMIC YEAR 2015-2016

CONTENTS

Introduction

The objective of this thesis is to present the development of Raman spectroscopy for label-free biochemical identification and classification of white blood cells as a potential diagnostic tool for acute lymphoblastic leukemia type B (B-ALL).

Leukemias are a diverse group of malignancies with a range of clinical presentations, prognoses and preferred treatment protocols. The B-ALL is a cancer of blood cells with the highest childhood cancer-related mortality, characterized by uncontrolled and *rapid* cell proliferation of immature B-cell progenitors that cannot mature properly into lymphocytic B cells [1][2]. Thus, its timely and accurate diagnosis is fundamental for successful clinical treatment.

A firm diagnosis of B-ALL requires first the identification of the leukemia cells, and second their classification based on the differentiation/maturation stage in which the lymphoblastic B cells are blocked. The conventional diagnostic approach as well as the monitoring response to therapy is performed through a combination of morphological and immunophenotypic analyses of bone-marrow or peripheral-blood cells. Morphological approaches allow the identification of B-ALL lymphoblasts and their classification into three main types (L1, L2 and L3) based on cell size, nuclear/cytoplasmic ratio, and nucleoli evaluations. However, in some cases of poorly differentiated B-ALL, morphological assessment provides low sensitivity and equivocal results [3]. Immunophenotypic detection of specific antigens that are related to the cell maturation stages might have prognostic or therapeutic implications, even within a single acute leukemia subtype. Therefore, multiparameter flow cytometry (up to six colours) is used to provide detailed determination of antigen expression profiles. Although the immunophenotypic analysis provides relevant information, the number of surface proteins that can be simultaneously detected, the photobleaching of the dye molecules and the interference with the fluorescence of the routine stains used in the cell morphology assessment limit its potentiality.

For these reasons, the development of novel diagnostic tools providing fast, highly sensitive and quantitative cell identification and differentiation from easily accessible body fluids is desirable [4].

In the last 10 to 15 years, Raman spectroscopy (RS) have emerged as powerful optical

tool that utilizes molecular-specific inelastic scattering of photons to interrogate biological materials [5]. A Raman spectrum represents a molecular fingerprint of a cell, providing specific information that is related to nucleic acids, proteins, carbohydrates, and lipids present within the cell. The technique has a high chemical specificity and its attractiveness comes from its ability to provide quantitative information about cell morphological and physiological states in a minimally invasive or non-invasive manner with almost no sample preparation [6]. Different cell types in different morphological states will vary in their overall molecular composition and this is reflected in the Raman spectra, as the intensity of the Raman bands depends upon the concentration of the bio-molecules [4-6]. Interrogation using RS minimally disturbs the native state of analysed cells and dynamic cellular processes at the single-cell level could be monitored, which is useful for assessing response to treatment. RS has wide potential in biomedical science as it can be applied to samples over a wide size range from single cells to intact tissue. The technique is well suited for studying living cells since water solution (buffers and culture media) do not interfere with the experiments and there is no need for cell labelling (HE stain or fluorescent probes) or other cell modifications. The other major benefit is that resolution is limited only by the diffraction limit of the laser spot (in our case smaller than 0.5 μm), thus allowing high quality images of cells to be obtained. Additionally, RS allows probing of the sub-cellular compartments Indeed, RS has been used recently as a novel technique to analyze precancerous tissues in the esophagus, colon, and cervix [7][8][9][10], as well for the identification, classification, and diagnosis of many cancer types [11][12][13][14][15][16][17].

The aim of my PhD research project was to develop an advanced optical technique, based on Raman Spectroscopy (RS) and its integration with other optical (e.g. fluorescence microscopy, flow cytometry, Raman imaging) and biological modalities (e.g. Western Blotting), in order to provide a fast and reliable procedure for identification and classification of single cells (hemogram) from peripheral blood of healthy donors as well as of cancer B-ALL patients.
The work can be divided into three main parts:

- Deep study of Raman spectroscopy literature with particular attention to its sensitivity, specificity and bio-applications.
- Development and characterization of the Raman microscope including the design of optics and development mathematical methods for analysis of the data (Principal Component Analysis). Since the aim of my thesis is to study living cells *in vivo*, with particular reference to normal and leukemia cells, the main challenges have been to

find correct laser wavelength and intensity, alignment and calibration of the Raman system and finally its application to demonstrate its usefulness.

- Completion of four experiments that demonstrate the suitability of Raman technique for studies of live normal and leukemia cells. Schematically, my research project concerns: (i) Raman identification and classification of three leukemia cell lines, that closely mimic the different differentiation/maturation stages of B-ALL cells; (ii) Spectroscopic regression assessment of leukemia after low- and not-cytotoxic dose treatments of methotrexate (MTX) and 6-mercaptopurine (6MP), two key drugs currently used in the B-ALL maintenance therapy; (iii) RS analysis of clinical samples collected from peripheral blood of patients with B-ALL; (iv) Raman identification and differentiation of the most important leukocyte populations isolated from peripheral blood of several human volunteers via conventional flow cytometry (granulocytes, monocytes, T cells, B cells and NK cells).

The results presented here demonstrate that RS in conjunction with multivariate statistical technique has potential for rapid label-free diagnosis, classification and follow-up after chemotherapy treatment of B-ALL based on the optical evaluation of spectral features of biomolecules.

The structure of my PhD thesis can be summarized as follow.

In chapter 1, I show the scheme of the blood cell formations (hematopoiesis) and the consequences of the scheme alterations. I introduce the concept of leukemias and the standard methods for leukemia diagnosis.

In chapter 2, I give an overview of the theory, show the pros and cons of the Raman spectroscopic technique and provide some examples of biomedical applications.

In chapter 3, I present the experimental Raman microscope developed to analyze single cells and its main characteristics. I introduce the supplementary techniques used to fully characterize the leukemia cells: Immunofluorescence, Western blot, Raman imaging and Flow Cytometry. Finally, I describe the Raman spectroscopic measurements, the spectral processing and statistical analysis.

In chapter 4, I describe the use of Raman spectroscopy to discriminate normal lymphocytic B-cells from three different B-leukemia transformed cell lines: namely RS4;11 and REH (both classified as L2 blast subtype) and the third cellular model system, MN60, is a more differentiated B-ALL cell type (classified as L3 blast subtype). In combination with immunofluorescence and Western blotting, I identify multiple intrinsic Raman peaks related to nucleic acid and protein molecular vibrations and I

show that these Raman markers reflect the relative changes in the potential biological markers from cell surface antigens, cytoplasmic proteins, and DNA content and correlate with the lymphoblastic B-cell maturation/differentiation stages.

In chapter 5, I describe the use of RS to analyze the biochemical features of these B-leukemia cell lines after low-dose and noncytotoxic treatments with methotrexate (MTX) and 6-mercaptopurine (6MP), the two key drugs used in current B-ALL maintenance therapy. To identify specific RS peaks that correlate with the different stages of these B-leukemia cells, I define the spectral changes after these B-ALL therapies in comparison with those seen under all-trans-retinoic acid (ATRA) treatment (used in the treatment of a different leukemia disease). Principal component analysis (PCA) is used to confirm the significance of these Raman spectral markers in the definition of the differentiation/maturation stages of B-ALL cells and in the detection of minimal residual disease.

In chapter 6, I extend the RS approach to discriminate between normal B-lymphocytes and B-lymphocyte-enriched fractions from patients with B-ALL. At first, I analyse these leukemic cells using standard multi-parametric flow cytometry in order to characterize them based on immunophenotypic classification: Pt-1 and Pt-2 where preliminary classified as “common B-ALL” and Pt-3 derived from the malignant transformation of a B cell progenitor intermediate between the pro-B and pre-B maturation stages. I demonstrate that the distinctive differences in the Raman spectra between normal and clinical patient samples confirm and further reinforce these observations.

In chapter 7, I show the feasibility of using RS and multivariate statistical approaches (PCA) to identify and discriminate leukocytes and, more in details, lymphocytes. I focused on five populations isolated from peripheral blood of several human volunteers via conventional flow cytometry: granulocytes, monocytes, T cells, B cells and NK cells.

Finally, the thesis includes the conclusions based on the performed experiments and a list of the publications related to my PhD cycle.

1

Leukemia classification and diagnosis

Leukemia is a group of different cancers of the blood cells that usually begin in the bone marrow and consist in proliferation of abnormal white blood cells. These white blood cells are immature cells and are called blasts or leukemia cells.

In my research activity, I focused my attention on the most abundant white blood cells and, in particular, I studied one of the most common childhood leukemia: B-cell acute lymphoblastic leukemia (B-ALL).

In the following chapter, I will show the scheme of the blood cell formations (hematopoiesis) and the consequences of the scheme alterations. I will introduce the concept of leukemias, the standard methods for leukemia diagnosis and show the advantages obtained by using the Raman Spectroscopy (RS), as novel and promising diagnostic technique.

1.1 Hematopoiesis

The hematopoiesis refers to a group of processes involved in the formation and maturation of the blood cells, starting from the hematopoietic stem cells (HSCs), as shown in Figure 1 [18]. They are found in the bone marrow and have the ability to start the maturation process of all the other blood cells. HSCs are self-renewing cells: during

proliferation, they show an asymmetric division in which some of their daughter cells remain as HSCs; the other daughters of HSCs (myeloid and lymphoid progenitor cells) cannot self-renew but they are able to start other differentiation pathways that lead to the production of one or more specific types of blood cells [19].

Therefore, HSCs give rise to both the myeloid and lymphoid lineages of blood cells.

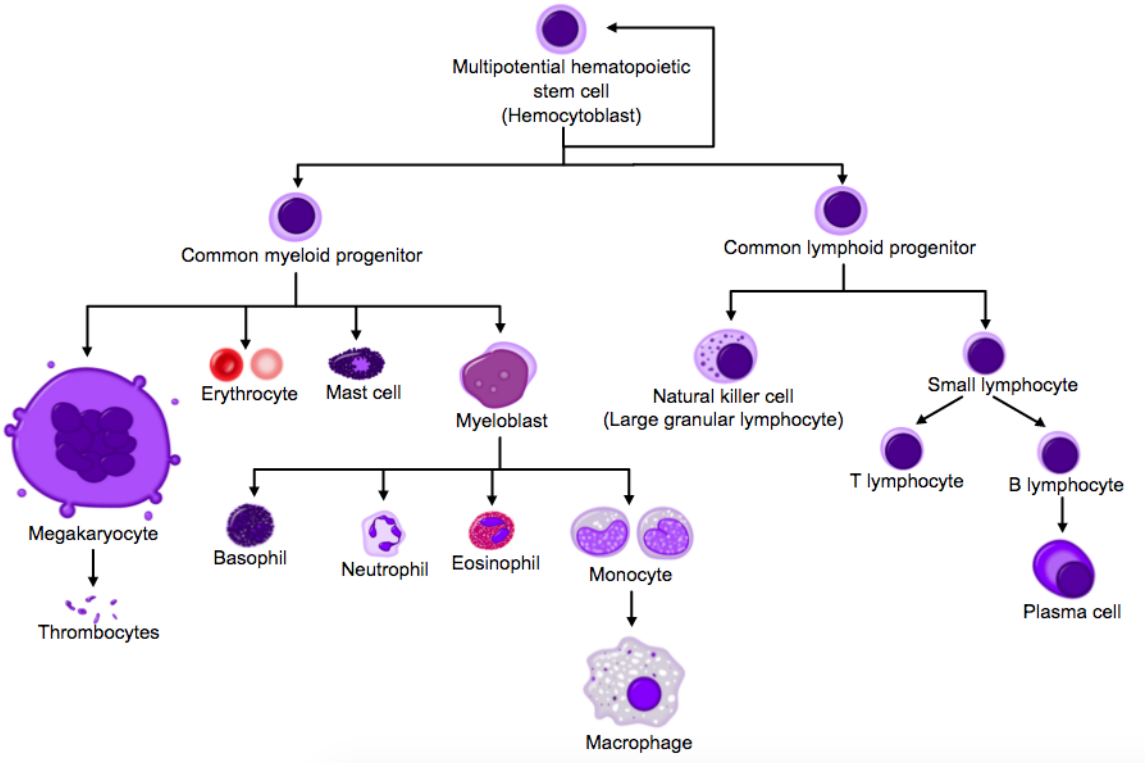

Figure 1: *Diagram showing the development of different blood cells from haematopoietic stem cell to mature cells.*

The lymphoid lineage is composed of three types of white blood cells, also known as lymphocytes: T-cells, B-cells and natural killer cells (NKCs). Lymphocytes are derived from common lymphoid progenitors and they are the cornerstone of the adaptive immune system.

The myeloid lineage is composed of megakaryocytes, granulocytes (basophil, neutrophil and eosinophil), erythrocytes (also called red blood cells - RBCs), monocytes and macrophages. They are derived from common myeloid progenitors and involved in a lot of different roles as innate immunity, adaptive immunity, and blood clotting.

Many of the stages of HSCs differentiation can be purified from the bone marrow or peripheral blood using characteristic cell surface markers, which has greatly facilitated the study of hematopoietic biology and revealed important molecular alterations in

haematological diseases [18]. An example is the leukemia, that is a neoplastic disorder characterized by the proliferation of immature leucocytes (blasts) that cannot carry their normal functions.

1.2 Leukemia classification

Leukemia is a group of haematological disease consisting in the proliferation of abnormal/immature white blood cells. Clinically and pathologically, leukemias consist of several different sub-types. The first classification classes are: acute and chronic leukemias [20].

Acute leukemia is characterized by a rapid and uncontrolled proliferation of immature blood cells. Under these conditions, the bone marrow is unable to produce healthy blood cells and, due to the rapid progression and accumulation of the malignant cells, the leukemic cells move into the bloodstream and spread to other tissues of the body. Acute forms of leukemia are the most common leukemia in childhood.

Chronic leukemia is characterized by the excessive increase of relatively mature, but still abnormal, white blood cells. Typically taking long time to progress, the cells are produced at a much higher rate than normal, resulting in many abnormal white blood cells. Chronic leukemia mostly occurs in older people, but can occur in any age groups.

The leukemia diseases are further classified into lymphoblastic or myeloid leukemias, according to which kind of blood cell is affected.

In the lymphoblastic leukemia, the malignant change takes place in a type of marrow cell that normally goes on to form lymphocytes, which are immune system cells. In myeloid leukemia, the malignant change takes place in a type of marrow cell that normally goes on to form red blood cells, some other types of white cells, and platelets.

The leukemia classification finally includes several subtypes depending on the specific precursor involved. A schematic summary of the current World Health Organization classification for acute leukemia is presented in Table 1.

Table 1: *World Health Organization classification for acute leukemia.*

Acute myeloid leukemia
AML with recurrent cytogenetic abnormalities
AML with myelodysplasia-related changes
Therapy-related myeloid neoplasms
AML NOS
Morphologic and immunophenotypic subtypes
Acute panmyelosis with myelofibrosis
Myeloid sarcoma
Myeloid leukemia associated with Down syndrome
Blastic plasmacytoid dendritic cell neoplasm
Acute leukemia of ambiguous lineage
Acute undifferentiated leukemia
Mixed phenotype acute leukemia with t(9;22)(q34;q11.2); *BRC-ABL1*
Mixed phenotype acute leukemia with t(v;11q23); *MLL* rearranged
Mixed phenotype acute leukemia, NOS (subclassify by phenotypes)
B-lymphoblastic leukemia/lymphoma
B-lymphoblastic leukemia/lymphoma with recurrent genetic abnormalities
B-lymphoblastic leukemia/lymphoma NOS
T-lymphoblastic leukemia/lymphoma

Abbreviations: AML, acute myeloid leukemia; NOS, not otherwise specified.

In this thesis, I will concentrate my attention on acute lymphoblastic leukemia type B (B-ALL), that is a neoplastic disorder that shows the highest childhood cancer-related mortality [1]. It is characterized by immature B-cell progenitors (i.e., lymphoid or lymphoblastic cells) that cannot mature properly into lymphocytic B cells [1][2]. B-ALL is a hematological malignancy that is characterized by uncontrolled and rapid cell proliferation. Thus, its timely and accurate diagnosis is fundamental for successful clinical treatment.

1.3 Leukemia diagnosis

A firm diagnosis of leukemia requires a gradual approach. Firstly, the identification of leukemia cells from the bone marrow or peripheral blood and the distinction of leukemia from other neoplastic disorders; secondly, the differentiation between myeloid (ML) and lymphoid (LL) leukemia; finally, the classification of ML and LL into sub-categories that define treatment and prognostic groups.

In the specific case of B-ALL, the diagnosis requires first the identification of the leukemia cells, and second their classification based on the differentiation/maturation stage in which the lymphoblastic B cells are blocked. B-ALL classification is primarily achieved by morphological and immunophenotypic analyses of cell samples from bone marrow or peripheral blood [1][2][21][22][23].

1.3.1 Morphology and cytochemistry in the leukemia diagnosis

Morphological analysis allows the identification of B-ALL lymphoblasts and their classification into three main types [24]:

- The L1 type is characterized by small (10- to 15-μ) and homogenous cells, with round, finely reticulated to coarse chromatin, some nuclear indentation, sparse slightly basophilic cytoplasm, high nuclear/cytoplasmic ratio and unclear nucleoli. L1 lymphoblasts are distinguished from normal mature lymphocytes by the homogeneity in their chromatin structure and their monotonous appearance.
- The L2 type is characterized by medium-sized (14- to 18-μ) cells with more heterogeneity in cell size. These lymphoblasts have fine chromatin, nuclear indentation and tight folding in some cells, basophilic cytoplasm, lower nuclear/cytoplasmic ratio and visible nucleoli. L2 lymphoblasts are distinguished from myeloblasts by the variation in size, more basophilic cytoplasm, and lack of granules.
- The L3 type is characterized by homogeneous, medium-sized to large cells with round, demarcated, and finely punctuated chromatin, no folding, deeply basophilic and vacuolated abundant cytoplasm, and nucleoli. Some apoptosis and fragmentation are usually seen. Vacuoles in the cytoplasm are not pathognomonic of Burkitt leukemia, and other features (eg, specific cytogenetic and immunologic characteristics) must be considered to make a definitive diagnosis.

In Table 2, French-American-British (FAB) classification and description of acute lymphoblastic leukemia are shown.

Table 2: *French-American-British (FAB) classification of acute lymphoblastic leukemia*

L1	Lymphoblasts with uniform, round nuclei and scant cytoplasm
L2	More variability of lymphoblasts Sometimes irregular nuclei with more cytoplasm than L1
L3	Lymphoblasts with finer nuclear chromatin and blue to deep blue cytoplasm that contains vacuoles

Figure 2 shows the images of three B-acute lymphoblastic leukemia cells according to the French-American-British (FAB) classification by using the May-Grünwald-Giemsa staining.

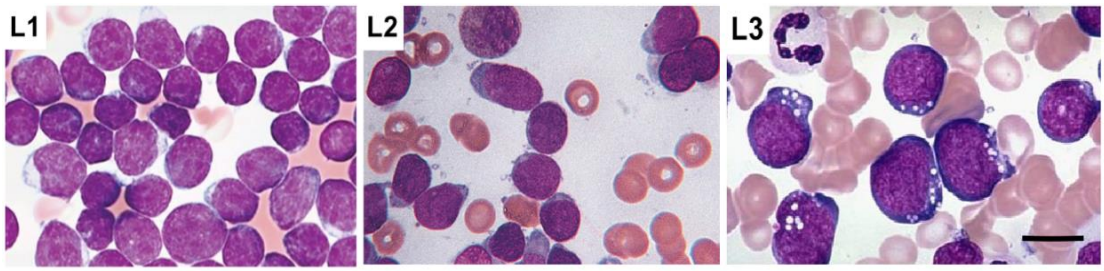

Figure 2: *Representative images of B-ALL cells using May Grünwald-Giemsa histochemical staining, according to FAB classification: L1 (top); L2 (middle); L3 (below). Scale bar: 10µm*

However, in some cases of poorly differentiated B-ALL, morphological assessment provides low sensitivity and equivocal results [3]. Although most cases can be diagnosed by this method, there is only a modest correlation between morphological categories, treatment responsiveness, and prognosis [3]. Detection of specific antigens that are related to these maturation stages might have prognostic or therapeutic implications, even within a single acute leukemia subtype.

1.3.2 Immunophenotyping in the leukemia diagnosis

The lineage of most cases of morphologically and cytochemically poorly differentiated acute leukemia can be accurately characterized by immunophenotyping.

The morphological approach can be combined with immunophenotypic B-ALL cell analysis of the arrested stage of B-cell maturation in terms of the surface expression of up to six to eight different B-cell–associated antigens by multi-parametric flow

cytometry [25][26][27][28]. Using this method, the B-ALL cell lineage is currently defined as:

- ‘pro–B-ALL’, when the cells originate from early pro–B lymphoblasts that express specific antigens (CD19 and CD38) at the plasma membrane;
- ‘common B-ALL’, when the cells originate from late pro–B lymphoblasts or intermediate B-cell precursors, as identified by the expression of CD19, CD38, CD10, and CD79a at the plasma membrane;
- ‘pre–B-ALL’, when the cells originate from more committed progenitors defined as pre–B lymphoblasts that express CD19, CD38, CD10, CD79a, CD20, CD22, and immunoglobulins at the plasma membrane [25].

However, this immunophenotypic analysis requires a panel of antibodies against several lymphoid-expressing antigens, and it is labor intensive and time consuming. Moreover, the use of fluorescent dyes is frequently limited by photobleaching of the dye molecule, the limited ability to detect multiple dyes, and interference with the fluorescence of the routine stains used in the cell morphology assessment [29]. Therefore, new approaches are required for rapid and sensitive diagnosis, classification, and prognosis of leukemias.

In the next section, I will introduce the Raman spectroscopy as novel diagnostic tool to address those questions.

2

Raman spectroscopy

The Raman spectroscopy is powerful tool for label-free spectroscopic and microscopic analysis of organic and biological materials: it allows to investigate single living cells in their natural environment.

In this chapter I will give an overview of the theory, show the pros and cons of the spectroscopic technique and provide some examples of biomedical applications.

2.1 Introduction to the Raman scattering

When a laser beam interacts with a sample, it is scattered from the molecules and the most photons are elastically scattered (Rayleigh scattering). These scattered photons have the same energy (frequency) and wavelength of the incident photons. On the other hand, a small fraction of the light (approximately 1 in 10^6 photons) is scattered at optical frequencies usually lower then the frequency of the incident photons. The process leading to this inelastic scatter is called Raman effect.

In 1923 Smekal discovered the inelastic scattering theoretically [30] whereas the effect of the inelastic scattering of the light was first reported by the Indian physicist C. V. Raman and independently by G. Landsberg and L. Mandelstam, in 1928 [31][32]. By monitoring the scattered light from various crystalline and amorphous solids, fluids and gases with a mercury arc lamp, Raman succeeded to identify the inelastic scattering

from the additional spectral bands. He described this discovery as a "spectrum of the new radiation", and considered it as the result of energy exchange between the incident light and the scattering medium. Raman has received the Nobel Prize in 1930 for his work and in 1998 the Raman effect was awarded, as recognition of its significance, an ACS National Historical Chemical Landmark as a tool for analysing the composition of liquids, gases, and solids.

The introduction and diffusion of the lasers in the 1960s allowed Raman spectroscopy to be more accessible to the scientific community [33][34][35]. In the 90's, Raman spectroscopy was being successfully used for biochemical analysis and characterization after the development of sensitive detectors, optical components and the employment of new generation lasers [36][37][38][39][40].

2.2 Classical theory

The Raman effect occurs when the incident light (monochromatic laser radiation) of γ_0 wavelength and frequency ν_0 impacts upon a molecule and interacts with the electron cloud of that molecule. The incident photon excites one of the electrons into a virtual state. As for the spontaneous Raman effect, the molecule will be excited from the ground state to a virtual energy state, and relax into a vibrational excited state (Stokes Raman scattering). If the molecule is already in an elevated vibrational energy state, the Raman scattering is then called anti-Stokes Raman scattering (Figure 3).

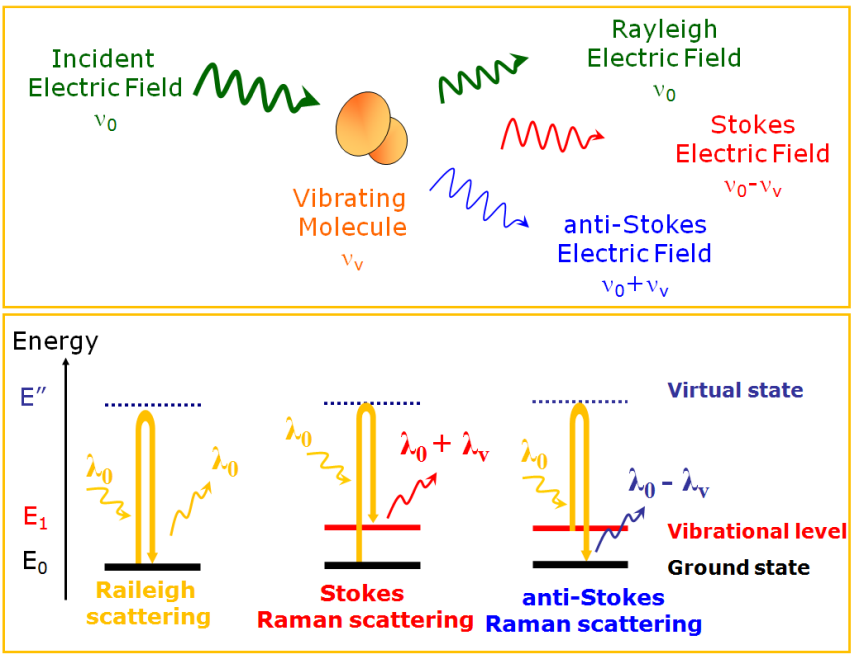

Figure 3: *Diagram of Raman scattering by molecules.*

The Stokes radiation occurs at lower energy (longer wavelength) than the Rayleigh radiation, and anti-Stokes radiation has greater energy. The energy increase or decrease is related to the vibrational energy levels in the ground electronic state of the molecule, and, the observed Raman shift of Stokes and anti-Stokes features are a direct measure of the vibrational energies of the molecule.

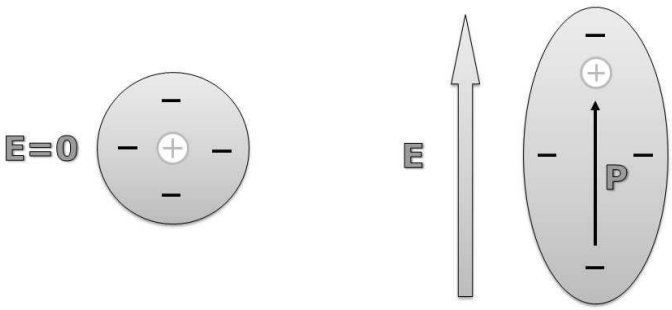

Figure 4: *Schematic of an induced dipole momentum by an electric field.*

A simple classical electromagnetic field description of the Raman spectroscopy can be used to explain many of the important features of the Raman scattering [41]. When a molecule is introduced into an electric field *E*, the latter induces an electric dipole momentum *P* in the molecule (Figure 4).

If α is the polarizability of the molecule, then the induced dipole moment is given by:

$$\vec{P} = \alpha\vec{E}. \qquad (1.1)$$

When electromagnetic radiation, at frequency ν_0, interacts with the molecule, this produces a varying electric field *E* whose dependence on the time *t* is given by:

$$\vec{E} = \overrightarrow{E_0} cos\omega_0 t\,, \qquad (1.2)$$

where E_0 is the equilibrium value of the electric field. So, from equations 1.1 and 1.2:

$$\vec{P} = \alpha\overrightarrow{E_0} cos\omega_0 t\,. \qquad (1.3)$$

Thus, the electromagnetic radiation induces a varying electric dipole moment, which then permits emission of light with the same frequency of the incident radiation. This phenomenon is called *Rayleigh scattering*.

For non-isotropic molecules the application of an electric field in a fixed direction induces a moment in different direction, and α becomes a tensor. In general, molecules

are non-isotropic, and the three equations, which take account of the unequal polarizability along different principal axes of the molecule, are:

$$P_x = \alpha_{xx}E_x + \alpha_{xy}E_y + \alpha_{xz}E_z\,, \qquad (1.4)$$

$$P_y = \alpha_{yx}E_x + \alpha_{yy}E_y + \alpha_{yz}E_z\,, \qquad (1.5)$$

$$P_z = \alpha_{zx}E_x + \alpha_{zy}E_y + \alpha_{zz}E_z\,, \qquad (1.6)$$

where, for example, P_x is the induced electric dipole moment in the direction of the x-axis. The tensor α is defined by these nine coefficients α_{xx}, α_{xy}, α_{xz}, … α_{zz}. Since $\alpha_{xy} = \alpha_{yx}$, $\alpha_{yz} = \alpha_{zy}$, $\alpha_{xz} = \alpha_{zx}$ the tensor α is really defined by six coefficients. If any of these six polarizability coefficients change during a rotation or a vibration, then the theory for a Raman spectrum is satisfied. For very small vibration amplitudes, the polarizability of the molecule is related to the normal vibrational coordinate q_n by the equation:

$$\alpha = \alpha_0 + (\frac{\partial\alpha}{\partial q_n})_0 q_n, \qquad (1.7)$$

where the label zero refers to the coordinate value at equilibrium configuration. Equation 1.7 is the same for each of the six coefficients that define α.

As is known, the normal coordinate q_v depends on the normal vibrational frequency v_v:

$$q_v = q_0 cos(\omega_n t)\,, \qquad (1.8)$$

where q_0 is the normal coordinate of the initial position. So, substituting eq. 1.2 in eq. 1.4, we obtain:

$$P_x = (\alpha_{xx}E_x^0 + \alpha_{xy}E_y^0 + \alpha_{xz}E_z^0)cos(\omega_0 t)\,. \qquad (1.9)$$

Taking α from eq. 1.7 and q_n from eq. 1.8, we have the following expression:

$$P_x = (\alpha^0{}_{xx}E_x^0 + \alpha^0{}_{xy}E_y^0 + \alpha^0{}_{xz}E_z^0)cos(\omega_0 t) + \left\{\left(\frac{\partial\alpha_{xx}}{\partial q_n}\right)_0 E_x^0 + \left(\frac{\partial\alpha_{xy}}{\partial q_n}\right)_0 E_y^0 + \left(\frac{\partial\alpha_{xz}}{\partial q_n}\right)_0 E_z^0\right\} q_n\, cos(\omega_n t)cos(\omega_0 t) \qquad (1.10)$$

Equation 1.10 may be easily converted into:

$$P_x = (\alpha^0{}_{xx}E_x^0 + \alpha^0{}_{xy}E_y^0 + \alpha^0{}_{xz}E_z^0)cos(\omega_0 t) + \frac{q_0}{2}\left\{\left(\frac{\partial\alpha_{xx}}{\partial q_n}\right)_0 E_x^0 + \left(\frac{\partial\alpha_{xy}}{\partial q_n}\right)_0 E_y^0 +\right.$$

$$\left(\frac{\partial \alpha_{xz}}{\partial q_n}\right)_0 E_z^0\Big\}\{cos(\omega_0 + \omega_n)t + cos(\omega_0 - \omega_n)t\} \qquad (1.11)$$

The first term of eq. 1.11 contains only one frequency factor ω_0 that is the one of the incident radiation. This term is interpreted in terms of the *Rayleigh scattering*. In addition to the incident frequency, the second term contains the frequencies $\omega_0 \pm \omega_n$. Thus, the induced dipole moment can also oscillate with two frequencies $\omega_0 \pm \omega_n$, interpreted as the vibrational frequencies. The $\omega_0 - \omega_n$ and $\omega_0 + \omega_n$ frequencies are known, respectively, as the *Stokes* and *anti-Stokes lines*.

Equation 1.11 is important since the α_0, in the first term, determines the properties of the Rayleigh radiation, while, in the second term, $(\partial\alpha/\partial q_n)_0$ determines the properties of the Raman scattering. In fact, it is clear that if $(\partial\alpha/\partial q_n)_0$ equals zero, so do the *Stokes* and *anti-Stokes* terms and there will be no Raman scattering. This gives a selection rule for the Raman-active motions: for a vibration to be Raman active, the polarizability of the molecule must change with the vibrational motion. Thus, Raman spectroscopy complements the IR spectroscopy (which is based on dipole moment changes).

Although very simple classical considerations can explain the presence of the *Stokes* and *anti-Stokes lines*, the classical theory is the most unsatisfactory. In fact, it predicts that the *Stokes* and *anti-Stokes lines* should be of equal intensity, whereas in practice the latter are very much less intense than the former.

For these reasons, a quantum mechanical approach is necessary to describe the intensity in the *Stokes* and *anti-Stokes lines*.

2.3 Quantum theory of Raman scattering

In the quantum theory, the Raman scattering process is considered as an excitation to a virtual state lower in energy than a real electronic transition with nearly coincident de-excitation and a change in vibrational energy (Figure 5) [42].

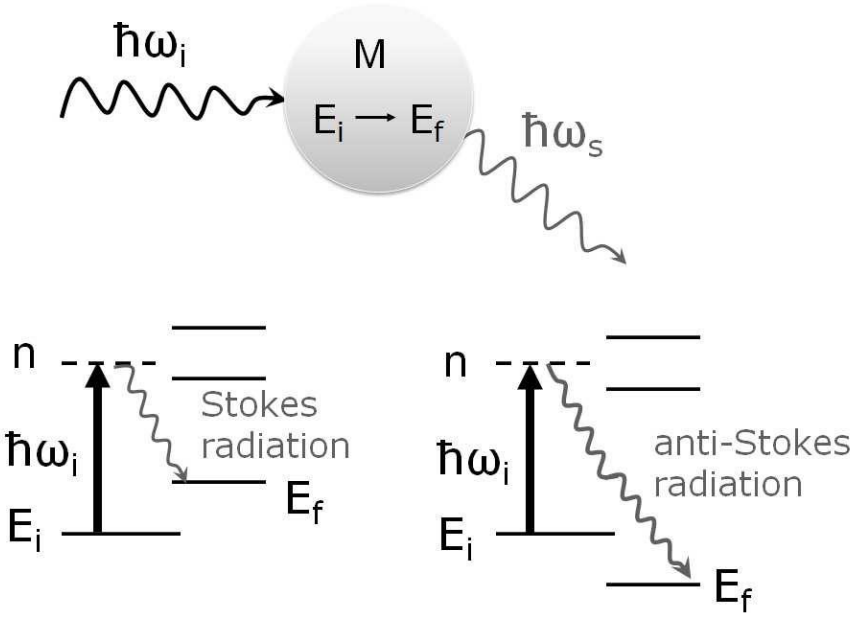

Figure 5: *Representation of the quantum theory for Raman scattering.*

The expectation value of the component α_{ij} of the polarizability tensor is given by:

$$\langle \alpha_{ij} \rangle_{ab} = \int u_b^*(q) \alpha_{ij} u_a(q) dq \,, \qquad (1.12)$$

where the function *u(q)* represents the molecular eigenfunctions in the initial level *a* and the final level *b*. The integration extends over all nuclear coordinates. This shows that a computation of the intensities of Raman lines is based on the knowledge of the molecular wave function of the initial and final states.

For small displacement q_n the molecular potential can be approximated by a harmonic potential, where the coupling between the different vibrational modes can be neglected. The functions *u(q)* are then separable into a product:

$$u(q) = \prod_{n=1}^{Q} \omega_n(q_n, v_n) \,, \qquad (1.13)$$

of vibrational eigenfunction of the n^{th} normal mode with v_n vibrational quanta, where $Q = 3N\text{-}6$ (or $3N\text{-}5$ for linear molecules) gives the number of normal vibrational mode for *N* nuclei. Using the orthogonality relation:

$$\int \omega_n \omega_m dq = \delta_{nm} \,, \qquad (1.14)$$

of the functions $\omega_n(q_n)$, it follows from eq. 1.12 and eq. 1.7:

$$\langle \alpha_{ij} \rangle_{ab} = a_{ij}^0 + \sum_{n=1}^{Q} \left(\frac{\partial \alpha_{ij}}{\partial q_n}\right)_0 \int \omega_n(q_n, v_a) q_n \omega_n(q_n, v_b) dq_n \qquad (1.15)$$

The first term is a constant and related to the Rayleigh scattering. For non-degenerate vibrations the integrals in the second term becomes zero unless $v_a = v_b \pm 1$. In this case its value is $[1/2(v_a + 1)]^{1/2}$ [43]. The basic intensity parameter of the vibrational Raman spectroscopy is the derivative $(\partial \alpha_{ij}/\partial q)$, which can be determined from the Raman spectra.

The intensity of a Raman line at a Stokes or anti-Stokes frequency ($\omega_0 \pm \omega_n$) is determined by the population density $N_i(E_i)$ at the initial level E_i, by the intensity I_L of the incident laser, and by the Raman scattering cross section $\sigma_R(i \rightarrow f)$ for the Raman transition $E_i \rightarrow E_f$:

$$I_{Raman} = N_i(E_i) \sigma_R(i \rightarrow f) I_L . \qquad (1.16)$$

At the thermal equilibrium, the population density $N_i(E_i)$ follows the Boltzmann distribution:

$$N_i(E_i) = \frac{N}{Z} g_i e^{-E_i/kT} \qquad (1.17)$$

with $N = \sum N_i$, the partition function $Z = \sum g_i e^{-E_i/kT}$, and g_i is the statistical weight.

In the case of the Stokes radiation, the initial state of the molecules could be the vibrational ground state, while for the emission of anti-stokes lines the molecules should have initial excitation energy. Due to the lower population density in these excited levels, the intensity of the anti-Stokes lines is lower by a factor:

$$\frac{I_{Stokes}}{I_{anti-Stokes}} = e^{-(\hbar\omega_n/kT)}. \qquad (1.18)$$

The scattering cross section depends on the matrix element of the polarizability tensor (equation 2.15) and contains furthermore the ω^4 frequency dependence. So, it can be written as follow [44]:

$$\sigma_R(i \rightarrow f) = \frac{8\pi\omega_S^4}{9\hbar c^4} \left| \sum_j \frac{\langle a_{ij} \rangle \hat{e}_L \langle a_{if} \rangle \hat{e}_S}{(\omega_{ij} - \omega_L - i\gamma_j)} + \frac{\langle a_{ji} \rangle \hat{e}_L \langle a_{jf} \rangle \hat{e}_S}{(\omega_{if} - \omega_L - i\gamma_j)} \right|^2 , \qquad (1.19)$$

where $\hat{e}_L$ and $\hat{e}_S$ are the unit vectors representing the polarization of the incident beam

and the scattered light. The fourth power dependence on the frequency indicates that the Raman intensities are 2^4=16 times higher for green excitation at 532 nm than for red excitation at 1064 nm. The sum extends over all molecular levels *j* with homogeneous width γ_j accessible by single-photon transitions from the initial state *i*. It can be seen from eq. 1.19 that the initial and the final states are connected by *two-photon* transitions: both states have the same parity. For example, the vibrational transitions in homo-nuclear diatomic molecules, which are forbidden for single-photon infrared transition, are accessible to Raman transitions.

2.4 Raman spectroscopy and imaging

Raman spectroscopy does not provide direct elemental composition of the sample. The change in frequency of the scattered photons provides chemical and structural information, which is characteristic of the chemical bonds or molecules present in the material. By plotting the intensity of the "shifted" light versus frequency results in a Raman spectrum of the sample. Generally, Raman spectra are plotted with respect to the laser frequency such that the Rayleigh band lies at 0 cm^{-1}. On this scale, the band positions will lie at frequencies that correspond to the energy levels of different functional group vibrations. The Raman spectrum can thus be interpreted similar to the infrared absorption spectrum and it provides information on the material chemical composition, state and aggregation of the sample and even in some cases details of factors such as stress, orientation and temperature.

Raman scattering can be observed microscopically using typical instrumentation used for laser fluorescence microscopy, but instead of the fluorescence signal, the Raman scattering signal is detected. The incident light is focused on the biological sample by means of a high numerical aperture (NA) objective lens to the resolution corresponding to the diffraction limit. Light scattered back from the illuminated spot on the sample is collected by the objective, is filtered and is directed to the spectrometer.

Raman imaging combines the spectral and spatial information. To create Raman images, the following steps have to be implemented:

a) The microscope has to be coupled to the Raman spectrometer.
b) Raman spectra of spatially resolved points have to be collected by a raster-scanning of the focused laser beam over the sample or by moving the sample through the laser focus in a raster pattern via a high-resolution microscope stage.

The resulting data sets of several thousand individual spectra can be converted into spectral images.

c) Spectral images have to be improved with different statistical methods, such as principal component analysis (PCA), vertex component analysis (VCA), and hierarchical cluster analysis (HCA) [45].

The total acquisition time depends on the number of spectra, the exposure time per spectrum, and the time for moving the stage.

2.5 Raman advantages and disadvantages

As a tool for characterization of chemical composition Raman spectroscopy is closely related to infrared (IR) spectroscopy. IR and Raman spectroscopy both measure the vibrational energies of molecules. In IR absorption spectroscopy the molecule absorbs light of a specific frequency that corresponds to the vibrational excitation. In Raman scattering the vibrating group in the molecule interacts with light. IR adsorption and Raman spectroscopy are complementary techniques (Figure 6), however they only yield a partial description of the internal vibrational motion of a molecule, as they are governed by different selection rules [46]. Raman effect is based on the inelastic scattering of photons by molecules and a change in the polarizability of the molecule occurs during the vibration. This means that the electron cloud of the molecule must undergo positional change. On the other hand, the infrared spectroscopy is based on absorption of light by vibrating molecules and the molecules undergo dipole moment change during vibration. So, when a molecule is symmetrical, e.g. O_2, we cannot observe any IR absorption lines because the molecule cannot change its dipole moment. It has been observed that molecules with a strong dipole moment are typically hard to polarize, and vice versa.

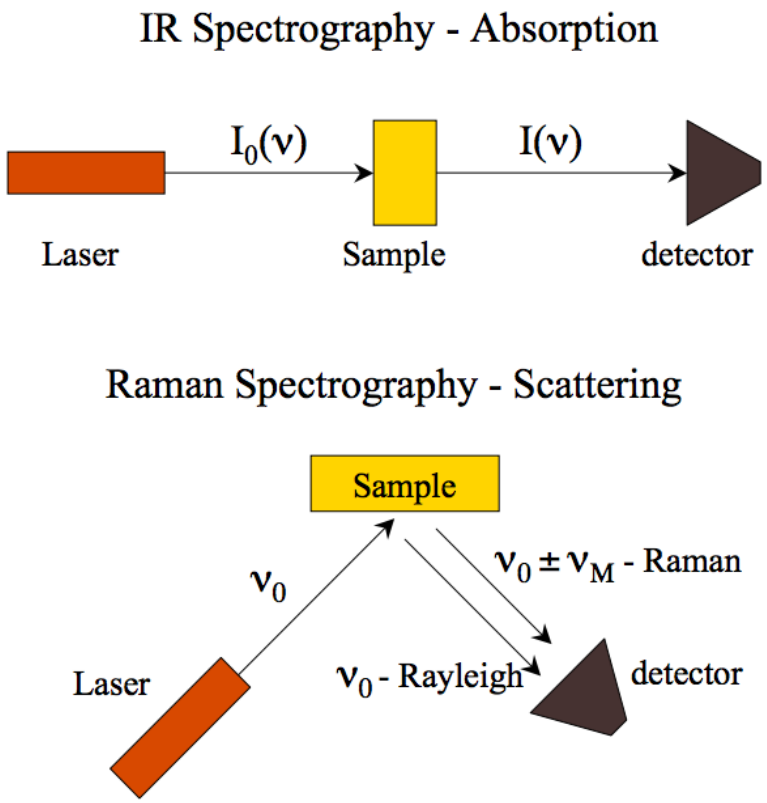

Figure 6: *Sketch of Infrared absorption and Raman scattering*

Regarding the excitation wavelength, the Raman technique uses a monochromatic beam or laser, in the visible, near infrared, or near ultraviolet range of the electromagnetic spectrum. The Raman signal intensity therefore depends inversely on the fourth power of the incident light wavelength, so that lasers with shorter wavelengths give a stronger Raman signal intensity. In IR spectroscopy, a monochromatic beam is used in the infrared region of the electromagnetic spectrum. The wavelength here increases or decreases over time, in order to observe all the absorption lines within a specific range of the infrared region.

Raman scattering is a rare event, this means that it takes a long time to get a signal, which can also be hidden by fluorescence or other background signals. The IR spectroscopy, could be more sensitive than Raman, however it does not work well for biological samples in aqueous solutions because it suffers from large water absorption effects.

Moreover, Raman does not suffer from these absorption effects and needs little or no sample preparation. It also has the added advantage that the concentration of the particular species is directly proportional to the intensity of spectral features shown. Infrared is only used for qualitative analysis, whereas quantitative and qualitative

analysis is possible by Raman spectroscopy: it gives clear and accurate information and does not require any type of label or chemicals to be added to samples. Characteristics IR and Raman spectra are shown in Figure 7.

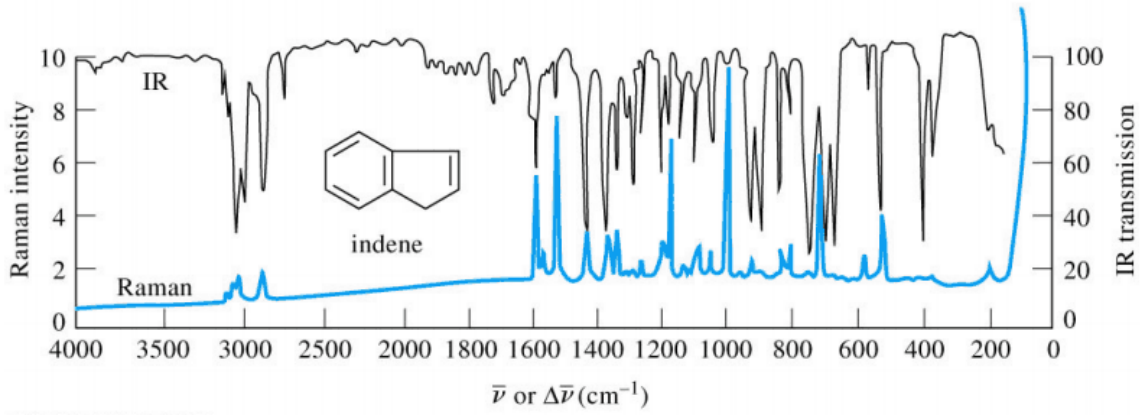

Figure 7: *Comparison of Infrared (black) and Raman (blue) spectra of a molecular sample*

Raman spectroscopy based techniques have many advantages, including a high chemical specificity and the ability to provide quantitative information about the sample in a minimally invasive or non-invasive manner with little or no sample preparation. The technique is well suited for studying live cells as water based solutions (buffer and culture media) do not interfere with experiments and there is no need for cell labelling or other cell modification as in fluorescence based approaches [47]. Raman microscopy has many advantages over fluorescence microscopy. First, Raman spectroscopy needs no external labelling and uses the induced polarizability (polarizability tensor derivative with respect to the normal coordinates) as a contrast in generating the vibrational spectra. Indeed, in a fluorescence process, the incident light should be completely absorbed by the sample and the system is transferred to an excited state. After a certain resonance lifetime it can go to different lower states. On the other hand, the Raman scattering is not a resonant effect and it can take place for any frequency of the incident light. In other words, while the fluorescence spectrum can be excited only with specific frequency of the incident light, whereas the Raman spectrum is independent from the excitation frequency. Second, biochemical signatures of the molecules are much richer as each component of the tissue, such as nucleic acids, lipids, biological chromophores, and proteins, provides its own pattern of vibrational behaviour in different spectral regions. Second, the new generation of Raman microscopes can offer a powerful non-destructive and noncontact method of sample analysis. One of the greatest benefits is the use of a confocal Raman microscope design. This enables a very small sample area or volume to be analysed down to the micrometer scale. Combining this micro Raman analysis with

automated focusing, XYZ movement makes possible production of “chemical” images of a sample with a higher spatial resolution than ever before.

Very small amounts of material can be studied at microscopic levels in the range of 10 microns. It can be used with solids, liquids or gasses. As mentioned above, no sample preparation is needed and it is a non-destructive technique. In terms of time, the spectra are stored relatively quickly. Further advantages include use of aqueous solutions, use of glass and the use of down fibre optic cables for remote sampling. On the other side, alloys or metallic materials cannot be used for Raman experiments. Because the Raman process is very weak, it leads to low sensitivity, making it difficult to measure low concentrations of a substance; for this reason the detection needs a sensitive and highly optimized instrumentation. Moreover, the intense laser radiation can destroy the sample and large background signals from fluorescence of impurities or of the sample can hide the Raman spectrum [46].

2.6 Applications in Biomedicine

The application of Raman spectroscopy to biological molecules has rapidly grown up since the early 1970s, presumably because of the development of lasers (monochromatic and coherent sources of light) and modern dispersive spectrometers. At first, the Raman application was completely focused on the collection of a spectral database recorded from different important biological molecules (proteins, nucleic acids, phospholipids and so on) in aqueous solutions, i.e. natural medium of biological molecules and systems. Later, Raman Spectroscopy has proved to be a promising and powerful technique to study more complex systems such as living cells and tissues [48]. The potential of conventional Raman spectroscopy as an interrogation method of cell structure and status is based on the fact that the Raman spectrum of a cell represents an information rich “fingerprint” of the overall biochemical composition of the cell. The information obtained is related to the intrinsic molecular composition of the cell, thus no labels or other contrast enhancing chemicals need to be used. The detection of time-dependent biochemical changes of cells has the potential to provide the additional level of information needed for quantification and discrimination of a wider range of toxic agents.

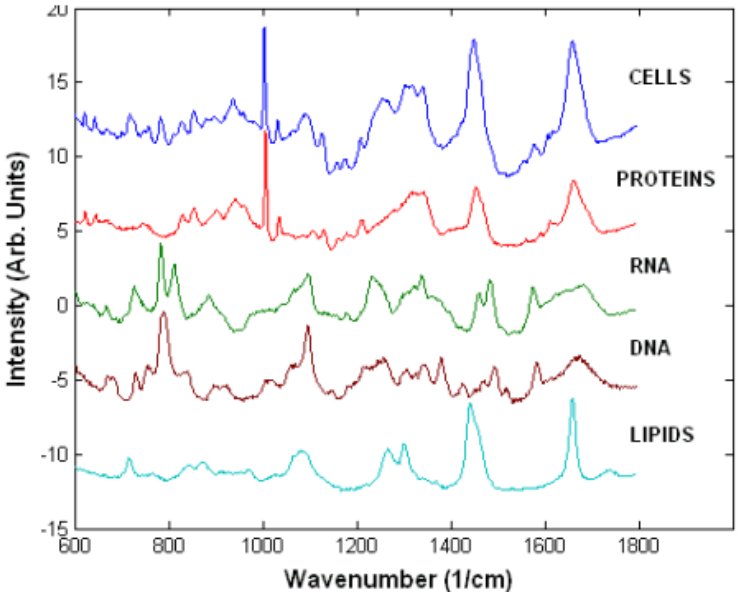

Figure 8: *Typical Raman spectrum of a cell and of main biopolymers found in cells.*

Table 3: *Peak assignment for Raman spectra of living cell.*

Peak (cm^{-1})	**Assignment**			
	Nucleic Acids	Proteins	Lipids	Carbohydrates
1736			C=O ester	
1680-1655		Amide I	C=C str.	
1617		C=C Tyr, Trp		
1607		C=C Phe, Tyr		
1578	G, A			
1480-1420	G, A, CH def	C-H	CH def	CH def
1342	A, G	C-H		CH def
1320	G	C-H		
1301			CH_2 twist	
1284-1220	T, A	Amide III	=CH bend	
1209		C-C_6H_5. Phe, Trp		
1176		C-H bend Tyr		
1158		C-C/C-N str.		
1128		C-N str.		C-O str
1095-1060	PO_2^- str.		Chain C-C str.	C-O, C-C str
1033		C-H in-plane Phe		
1005		Sym. Ring br Phe		
980		C-C BK str. β-sheet	=CH bend	
937		C-C BK str. α-helix		C-O-C glycos.
877			$C\text{-}C\text{-}N^+$ sym str	C-O-C ring
854		Ring br Tyr		
828	O-P-O asym.str.	Ring br. Tyr		
811	O-P-O str. RNA			
788	O-P-O str. DNA			
782	U,C,T ring br			
760		Ring breath Trp		
729	A			
717			$CN^+(CH_3)_3$ str	
667	T, G			
645		C-C twist Tyr		
621		C-C twist Phe		

Raman spectra of live cells consist of bands corresponding to all biopolymers found in cells (Figure 8). The peak assignment of these spectra is presented in Table 3 [49].
Nucleic acids can be identified by peaks characteristic of nucleotide and sugar-phosphate backbone vibrations. The main peaks are found at 1095 cm^{-1} (phosphodioxy group PO2-), 788 cm^{-1} (C5-O-P-O-C3 phosphodiester bonds in DNA) and 813 cm^{-1} (C5' -O-P-O-C3' phosphodiester bonds in RNA), 782 cm^{-1} (thymine, cytosine and uracil) and 1578 cm^{-1} (guanine and adenine). The phosphate peaks are particularly useful to determine the structure of DNA (A, B or Z forms) and also provide the main distinction between DNA and RNA. The spectra of proteins are dominated by peaks corresponding to the Amide I (1660-1670 cm^{-1}) and Amide III (1200-1300 cm^{-1}) vibrations, which have been shown to be sensitive to the secondary structure of the proteins. There are additional Raman peaks corresponding mainly to amino acids containing phenyl groups, such as phenylalanine (1005 cm^{-1}), tyrosine (854 cm^{-1}) and tryptophan (760 cm^{-1}) as well as C-H vibrations (1449 cm^{-1}). While it is difficult to distinguish between specific types of proteins on the basis of their Raman spectra, the Amide I and Amide III peaks are sensitive to subtle changes in the secondary structure of proteins. The strongest Raman peaks of lipids are present at 1449 cm^{-1}, 1301 cm^{-1} (C-H vibrations) and 1660 cm^{-1} (C=C stretching) and belong to vibrations of the hydrocarbon chains. Additional Raman peaks corresponding to head groups of phospholipids can also be found, such as the 719 cm^{-1} peak corresponding to the C-C-N+ symmetric stretching in phosphatidylcholine, a major constituent of cellular membranes. Carbohydrates can be identified and analysed reliably due to their characteristic Raman peaks of sugars, especially the C-O-C vibrations of the glycosidic bonds and sugar rings (800-1100 cm^{-1}).
Cells of different type or in different physiological states will show a different molecular composition. Raman spectra reveal the overall molecular composition, and so spectra will be different depending on the concentration of the molecules. Pathological changes in molecular composition or structure are shown by the spectra, allowing development of diagnostic tools based on Raman spectroscopy [50][51][52].

Although interesting spectral information has been obtained from suspensions of cells [53], single cell spectra offer important information concerning specific biological functions, cellular interactions with other cells, drugs, biomaterials and so on. Raman spectroscopy has been used to examine single fixed [54][55], dried [56], and living cells [57][58][59] grown or deposited on specific "Raman-transparent" substrates (usually quartz or CaF_2 slides). Recent reports showed the capability of Raman microscopy to study nucleic acids in cells under different conditions [53], to detect molecular changes

during cell death [60][61][62][63], to study the interaction of cells with toxic agents [64], to identify differences between active and non-active T-lymphocytes [65]. Since Raman spectroscopy methods have been used for many years, there are a a lot of recent excellent reviews of Raman spectroscopy as a tool for life science and biomedical research [49][66][67][68][69][70][71][72].

Raman spectroscopy was recently applied to achieve an early detection of cancers, to control the effect of various agents on the tissue, to identify and differentiate several pathogenic microorganisms found in blood infections [73]. Raman spectroscopy can also discriminate healthy tissue from diseased tissue, due to the chemical changes resulting from a disease. For instance Huang *et al*. used near infrared Raman spectroscopy to distinguish healthy bronchial tissue from tumor tissue [74]. Haka *et al*. demonstrated the potential of Raman spectroscopy to diagnose breast cancer lesions [75].

Furthermore, the progress in microcomputer manufacturing together with the elaboration of rapid mathematical and statistical algorithms, offer to Raman spectroscopy the possibility of acting as a powerful imaging tool. A Raman image, collected from a complex biological system, i.e. cell or tissue, can provide useful information on the localization or distribution of different constituting molecules [76].

Optical Raman imaging has emerged from the Raman spectroscopy technique as a new method which allows real time, non-invasive, high-resolution imaging of tissue, with a particular focus on cancer diagnosis. Recently, more sensitive detectors have become available, making the technique easily applicable [77].

Lately, Raman spectroscopy has been applied to investigate the differences between the leukocyte subtypes which have been obtained from healthy donors. Raman imaging was able to display the same morphological features as standard staining methods without using any labels and to separate Raman spectra of the two most abundant leukocytes, the neutrophils and lymphocytes ($CD4^+$ T-lymphocytes) [78].

It was also natural to use Raman spectroscopy as a tool for diagnosis, for instance in analyzing metabolic effects in biological fluids, or alterations induced in tissues upon cancer formation, such as changes in DNA, protein and lipid conformations, or molecular degradation. Thanks to the continuing technical progress, Raman spectrometers can be used in the future as a non-invasive tool for biomedical diagnosis.

3

Experimental methods and data analysis

In this chapter, I will present the experimental Raman microscope developed to analyze single cells and its main characteristics. I will introduce the supplementary techniques used to fully characterize the leukemia cells: Immunofluorescence and Western blot analysis. Finally, I will describe the Raman spectroscopic measurements, the spectral processing and statistical analysis.

3.1 Raman experimental setup

A sketch of the Raman setup, built up in the Biophotonics laboratory of Dr. A. C. De Luca, is shown in Figure 9 [79][80]. It consists of three major components:

1. Excitation source (laser).
2. Microscope and light collection optics (microscope, mirrors, filters and lenses).
3. Detection optics (Spectrometer and CCD).

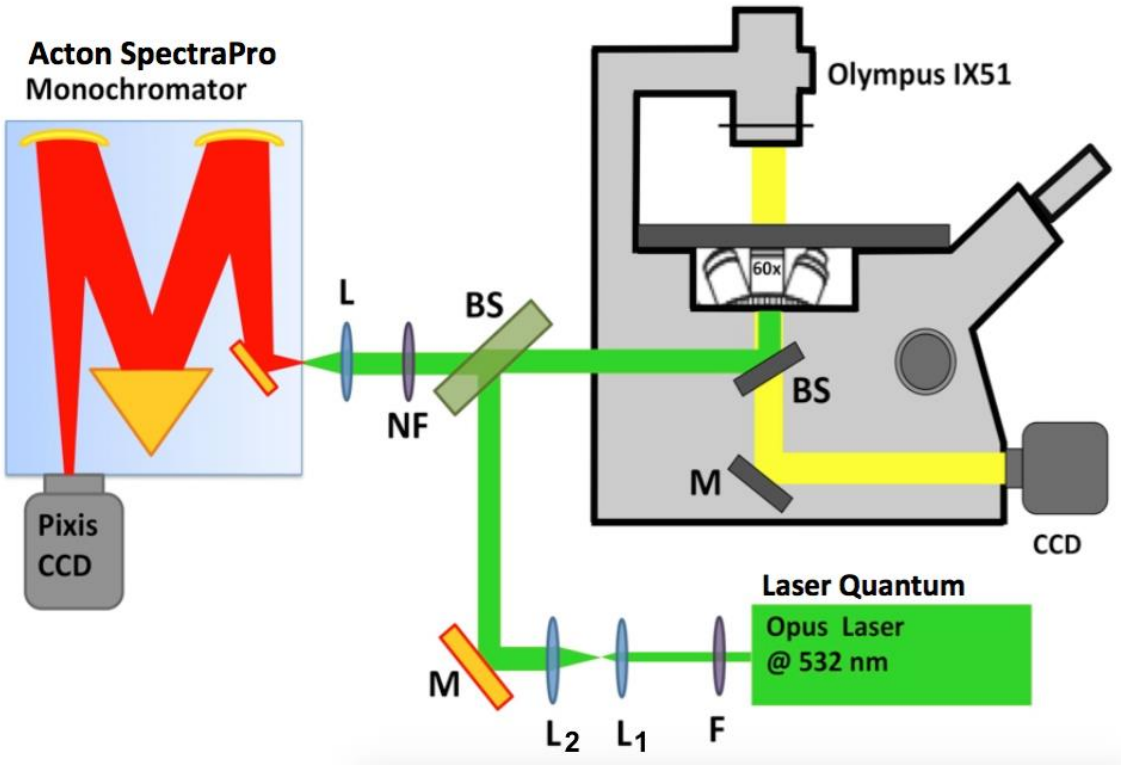

Figure 9: *Schematic of our Raman microscope system (M-mirror; L-lens; F-filter; BS-beam splitter; NF-notch filter; BPF-band pass filter).*

3.1.1 Laser

Cell biomolecules are sensitive to light and this makes the choice of laser parameters crucial for studying living cell. Three effects in particular need to be considered: cell photo-damage, which is a light-induced reduction in cell viability, excitation of sample/ medium autofluorescence and efficiency of the Raman scattering.
Considering these features, the Raman probe used was a green diode laser (Opus, Laser Quantum) at 532 nm. It provides a maximum power of 2 W and exhibits excellent beam parameters and power stability.

The average laser excitation power on the sample was 2 mW, to avoid cellular damage and degradation. Raman spectra were recorded using an integration time of 20 s.

The laser output characteristics are reported in the Table 4.

Table 4: *Opus 532 laser output specification*

Power	2 W
Wavelength	532nm
Beam Diameter	1.85mm ± 0.2mm
Spatial Mode	TEM00
Bandwidth	45 +/- 10GHz
Divergence	<0.44 +/- 0.07mrad
Power Stability	<0.2% RMS
Noise	<0.08% RMS
Noise Bandwidth	10Hz - 100MHz
Pointing Stability	<2μrad/°C
Polarisation Ratio	>100:1
Polarisation Direction	Horizontal
Coherence Length	0.7cm
Beam Angle	<1mrad
Operating Temp	15 - 40ºC
Umbilical Length	1.5m

3.1.2 Microscope and light collection optics

The laser beam at 532 nm was spatially filtered using a laser-transmitting filter (Maxline, Semrock) and expanded by a telescopic system. The telescopic system, formed by lenses L_1 (f_1 = 50 mm) and L_2 (f_2 = 150 mm), gives a linear magnification of $M = f_2/f_1 = 3$. As matter of fact, the laser beam diameter at the end of the telescope was around 6 mm. The laser beam was introduced in an inverted microscope (Olympus IX51) to illuminate the sample. The use of the inverted Raman micro-spectrometer offers more flexibility for performing Raman spectral imaging and time-course experiments on live cells, since cells are not disturbed during experiments. The most important component of the microscope in Raman microscopy is the objective: 60x objective lens (Olympus UPLSAPO 60XW, water immersion, numerical aperture 1.2). It focuses the laser beam onto the sample as well as collects the resultant Raman scattered light from the sample. For Raman spectral imaging of cells, the following characteristic of the objective was considered: i) high numerical aperture (NA) allowing high resolution and collection of light, ii) low background.

The back-scattered light from the sample was collected from the same objective and

filtered from a dichroic beam-splitter (RazorEdge 45° beam-splitter, Semrock), where the radiation at 532 nm was cut. The Raman light was filtered using a laser-blocking filter (RazorEdge 0° notch filter, Semrock) to eliminate the residual Rayleigh scattering and then focused onto the entrance slit of the monochromator (Acton SP2300, Princeton Instruments). The Raman scattered light was finally detected by using a back-illuminated CCD. The detector was interfaced to a personal computer, where spectra were stored and analysed.

Halogen lamps light, focused on the sample by a condenser (working distance = 27 mm and NA = 0,55), and a digital camera (Olympus Soft Imaging LC20), coupled to microscope, were used to image the sample on a display during the acquisition.

The sample chamber is made up by a 150 μm quartz coverslip (UQG Optics), a 100 μm spacer and a 1 mm quartz microscope slide; the chamber is sealed and mounted on the manual X-Y microscope stage.

3.1.3 The detection optics

The Raman radiation, coming from the sample, has been detected by using a monochromator (ACTON SP2300, Princeton Instruments) set at 250 μm to reject the off-focus light in order to increase the signal-to-noise (SNR) ratio and a back-illuminated charge-coupled device (PIXIS:400BR-eXcelon CCD, 1340x400 pixels, Princeton Instruments), and placed at the monochromator exit.

The spectrometer, consisting of two concave mirrors and one plano diffraction grating (f/3.9 Czerny-Turner configuration, Figure 10), separates the incident light into its component wavelengths so the relative amounts of radiation at each wavelength can be measured. A lens (f = 50 mm) is placed in front of the spectrometer to ensure the best focusing of the Raman photons onto the spectrograph slit. Focused light enters the spectrograph through an entrance slit (250 μm) and is then collimated and shone on a grating (1200 grooves/mm reflective diffraction grating, 750 nm blaze wavelength), which disperses the light providing an estimated spectral resolution of approximately 1 cm^{-1}.

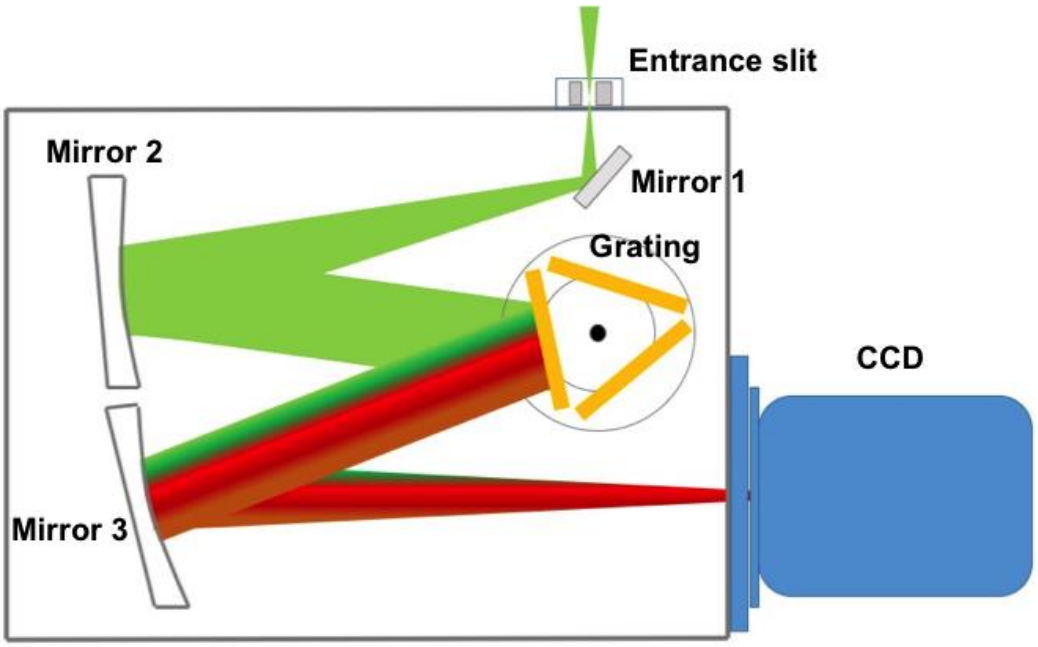

Figure 10: *Schematic of spectrometer (Czerny-Turner configuration).*

In Figure 11 the efficiency curve of the diffraction grating of the monochromator is shown.

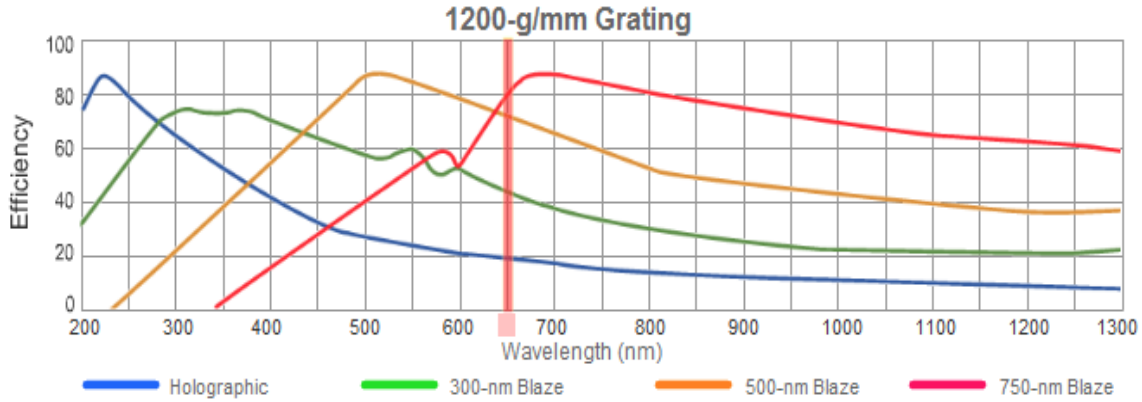

Figure 11: *Efficiency curve of 1200 lines/mm reflective diffraction grating (at 750 nm blaze wavelength).*

Finally, the dispersed light is collected from the CCD camera. The CCD used in our system is a back-illuminated CCD (PIXIS:400BR-eXcelon) thermoelectrically cooled at 70ºC. Thanks to the cooling technology, PIXIS camera offers extremely low dark current, which is a slow and steady growth of unwanted signal generated by the heat inside the detector. The advantage of back illuminated chips is that the surface is clear of obstruction (the back of the CCD has no electrodes), therefore is more sensitive. Moreover, the PIXIS eXcelon^{TM} technology increases the CCD sensitivity while

suppressing etalon interference fringes observed in the NIR with conventional back-illuminated devices (Figure 12).

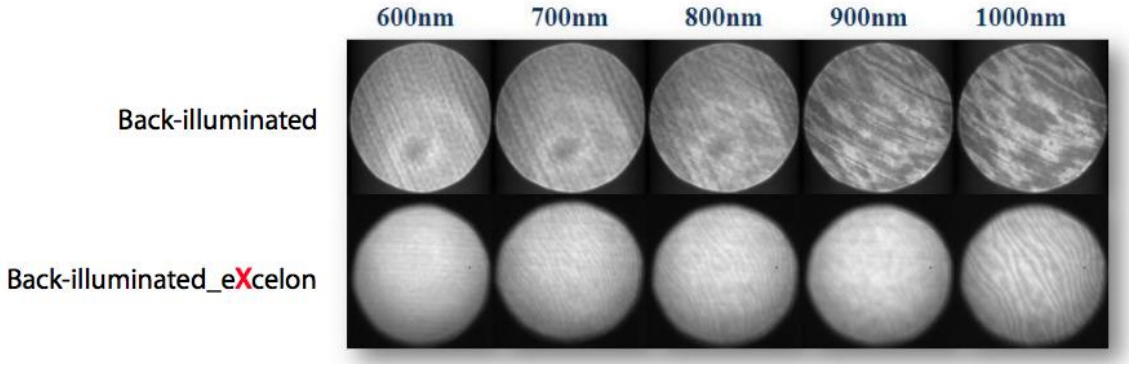

Figure 12: *Comparison of etaloning performance of eXcelon vs. back-illuminated CCDs.*

Figure 13 shows the quantum efficiency of PIXIS CCD with eXcelon™ technology.

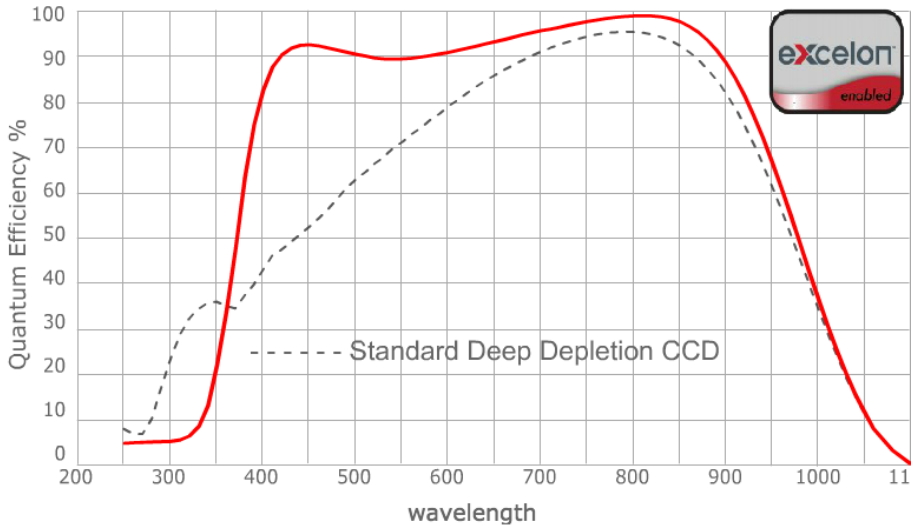

Figure 13: *Quantum efficiency of PIXIS back-illuminated CCD.*

3.2 Sample preparation

B-ALL cell lines. We used B-Acute Lymphoblastic Leukemia cells (B-ALL) as biological model in the Raman experiments: the RS4;11, REH and MN60 B-leukemia cell lines were obtained from Leibniz Institute DSMZ-German Collection of Microorganisms and Cell Cultures (Germany) (Figure 14). The RS4;11 cell line (an L2 subtype) was originally derived from a 32-year-old female patient with B-ALL at relapse [81][82]. The REH B-leukemia cell line was originally derived from a 15-year-old male patient with common B-ALL at relapse, and these are morphologically similar to the RS4;11 B-leukemia cells [83]. The MN60 B-leukemia cell line (an L3 subtype)

was originally derived from a 20-year-old male patient with B-ALL during remission phase [82]. The RS4;11 and MN60 B-leukemia cell lines [81] were maintained in α-MEM supplemented with 10% (v/v) fetal bovine serum, 2 mM L-glutamine, 50 U/mL penicillin and 50 µg/mL streptomycin. The REH B-leukemia cell line [36] was maintained in RPMI supplemented with 20% (v/v) fetal bovine serum, 2 mM L-glutamine, 50 U/mL penicillin and 50 µg/mL streptomycin. For the drug treatments, a 10 mM stock solution of 6MP in 1 M NaOH and 10 mM stock solutions of MTX and ATRA in dimethylsulfoxide were diluted in cell cultured medium, and the cells were treated for 72h before processing for Immunofluorescence or Western blotting. It is important to note that the final concentration of dimethylsulfoxide in these treatments was at least 100-fold below the described differentiating concentration for dimethylsulfoxide [85].

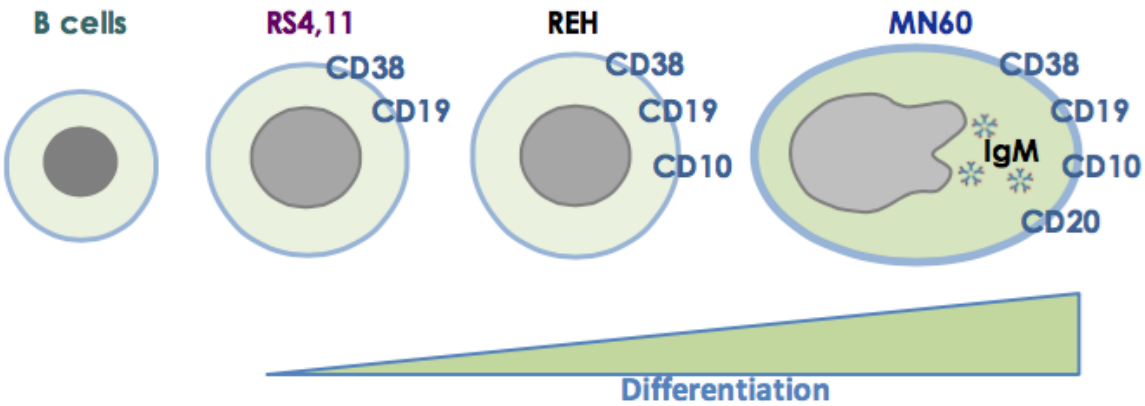

Figure 14: *Experimental model of B-ALL differentiation.*

B- and B-ALL cells. B lymphocyte populations were collected from peripheral blood of healthy volunteers or leukemia patients. Normal B-cell-enriched fraction of lymphocytes was obtained using EasySep Negative selection kits (Stemcell Technologies Inc) for heparinized venous blood obtained from healthy volunteers [86], and according to the manufacturer instructions. B-ALL cells were collected from the peripheral blood of three male patients with B-ALL (Age 22-, 5 and 23-years old for Pt-1, Pt2 and Pt3, respectively). Blood samples for all patients were withdrawn at diagnosis, prior to therapeutic regimen start. After the samples were collected, mononuclear cells were purified using Ficoll-Histopaque 1.077 g/mL density gradient centrifugation (Figure 15). As the B-ALL cells were then around 95% of the purified fraction, no further step was used for these B-ALL cells. Before the RS, the cells were treated with 10 mg/mL DNAse-I solution (Stemcell Technologies Inc) to digest the DNA from damaged cells.

This step was important to reduce viscosity, and to remove membrane-bound DNA fragments that could interfere with the RS analysis. Informed consent for the use of biological samples for research purposes was obtained from both the healthy volunteers and the patients with B-ALL. The lymphocytes in the B-enriched fractions were routinely >98% surface immunoglobulin positive, as assessed by flow cytometry.

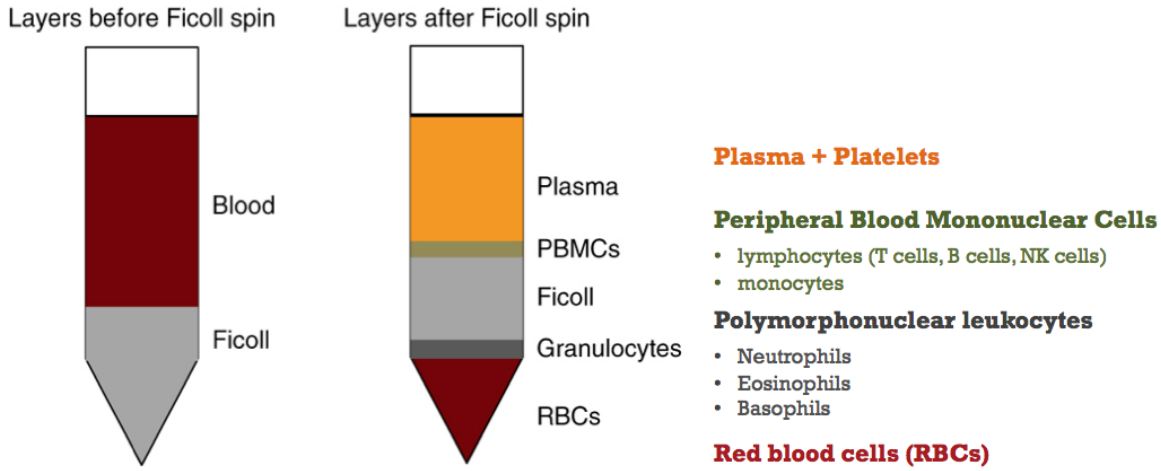

Figure 15: *Ficoll-Histopaque procedure for isolation of lymphocytes (B-cells).*

Leucocytes. An established protocol for leukocyte separation from peripheral blood of healthy donors based on Ficoll-Histopaque 1.077 g/mL density gradient centrifugation has been used. After the centrifugation, the granulocytes precipitate to the bottom of the Ficoll tube together with the majority of the red cells (Figure 15). The lymphocytes and monocytes remain in the middle of the tube (*buffy coat*). The monocyte and lymphocyte populations were separated by collecting the buffy coat and using a specific immunomagnetic separation procedure (EasySep Negative selection kit, Stemcell Technologies Inc) for monocytes, B cells, T cells and NK-cells, respectively, and according to the manufacturer instructions [86]. Instead, the granulocytes were obtained simply collecting the red pellet at the bottom of Ficoll tubes and lysing the red cells with ammonium chloride.

3.3 Raman wavelength calibration

The Raman spectrum of the polystyrene bead (5 µm-sized) was acquired for the wavelength calibration of the system. The standard software interface WinSpec is used to control and acquire data from CCD camera. After data acquisition (acquisition time

2s), the collected data are saved as ASCII files and analysed by using the Origin 9.0 software.

The Raman spectrum of the polystyrene bead was used to precisely set a wavenumber for each individual detector pixel. Indeed, the polystyrene Raman spectrum is well known: there is a collection of over 1000 Raman spectra of a wide range of compounds compiled by Professor Richard L. McCreery's research group, including polystyrene (Figure 16) [87].

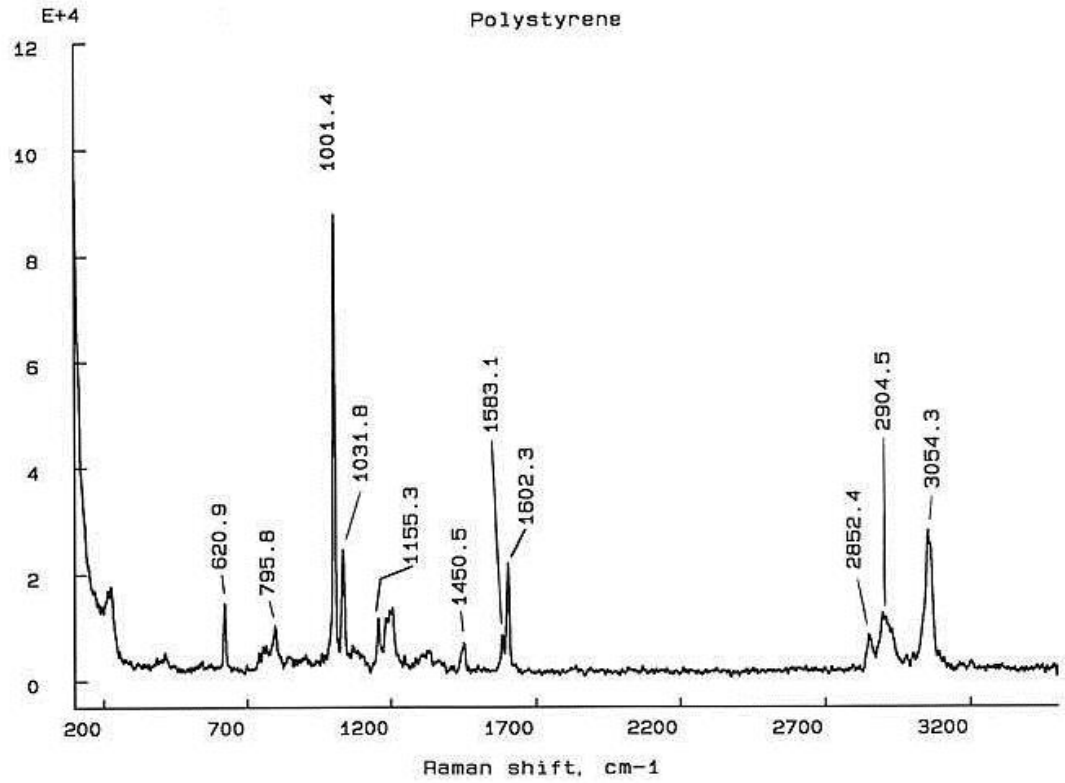

Figure 16: *Raman spectrum of polystyrene from McCreery group.*

As shown in Figure 17a, a straight line fits the calibration points distributed over the whole spectral region of interest. In this way, the pixels were associated to the appropriate relative cm^{-1} values. The final spectral resolution was 1 cm^{-1}. In Figure 17b we reported the acquired Raman spectrum of a polystyrene bead that was used for wavelength calibration of the system.

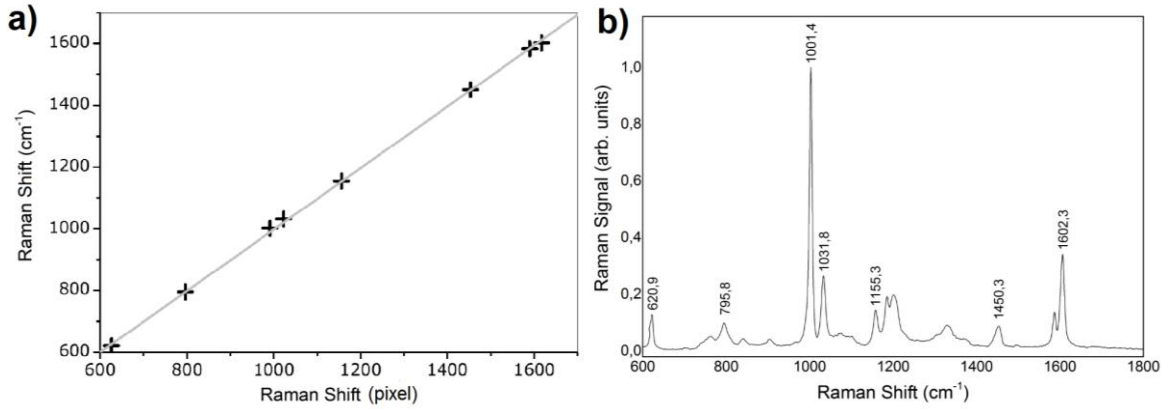

Figure 17: *(a) Raman peaks position in pixel as a function of the wavenumber values. A linear fit of the experimental data is also shown. (b) Calibrated Raman spectrum of a polystyrene bead. The acquisition time is 2 s. Laser power on the sample is 2 mW.*

3.4 Raman system spatial resolution

We experimentally measured the resolution of our system by acquiring the Raman signal of a 0.5 µm polystyrene bead and scanning the laser probe in the x (step size 20 nm) and z (step size 50 nm) directions, as shown in the figure below. We measured the FWHM from a Gaussian fit of the experimental data and the achieved resolution was $\sigma_x = \sigma_y =$ 0.9 µm and $\sigma_z = 4.0$ µm (along optical axis) (Figure 18). The axial resolution (σ_z) was further checked by measuring the variation of the Raman signal acquired from the center of polystyrene bead as a function of the bead size (Figure 19).

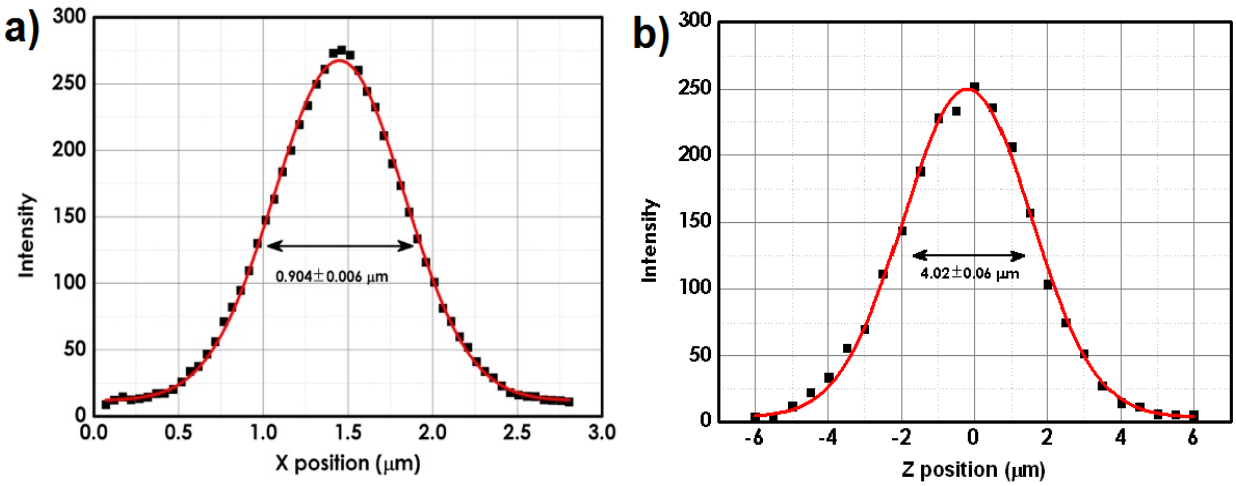

Figure 18: *(a) Resolution and FWHM value along X-axis. (b) Resolution and FWHM value along Z-axis.*

By moving from 4 μm to 5 μm -sized polystyrene bead the signal does not increase linearly, confirming that the axial resolution of the Raman microscope was about 4 μm. The probe volume, approximately calculated as the volume of a cylinder with a base diameter of 0.9 μm and a height of 4.0 μm, was about 2.54 μm^3.

Therefore, even if the laser position, during acquisition, was focused on the cell nucleus, we can conclude that a large volume of the cell is investigated including the cytoplasm and cell membrane.

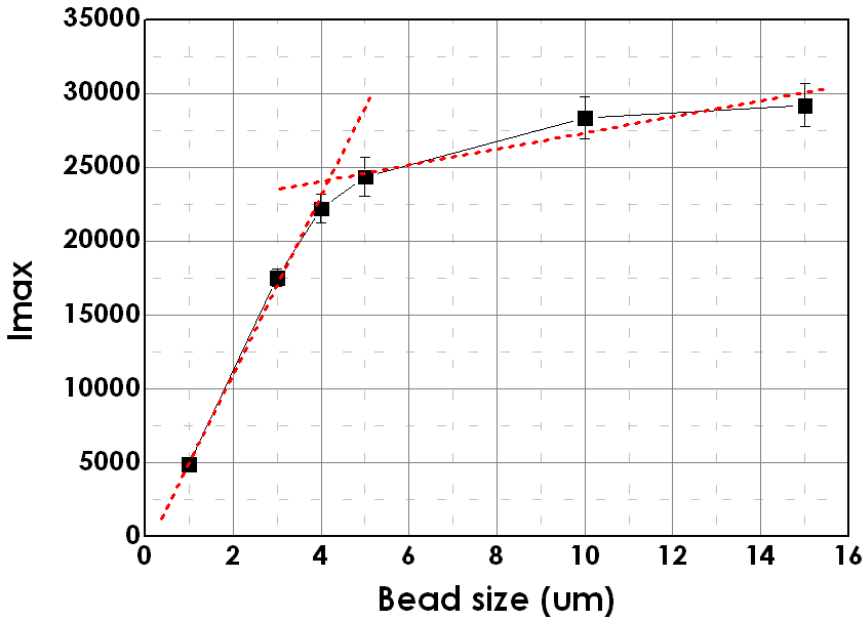

Figure 19: *Raman signal from the center of polystyrene bead as a function of the bead size.*

3.5 Raman measurements and spectral processing

All of the spectral signals were acquired taking into account four key experimental parameters.

i. During acquisition, the laser was focused on the lymphocyte nucleus to limit the spectral variability from individual cells.
ii. For each cell type, the cells analyzed were derived from different cultures, to ensure that the observed differences were the result of biological variations rather than variations in instrument background or cell culture conditions.
iii. For each experimental session, more than 50 cells were analyzed, to take into account possible biochemical differences in the spectral data due to variations in cell-cycle progression.

iv. The spectra that were obtained from cells with morphological alterations due to apoptotic status or that were in transition through the mitosis phase (visible and well defined under optical microscopy) were not included in the subsequent analyses.

The average laser excitation power on the sample was 2 mW, to avoid cellular damage and degradation. Raman spectra in the range between 600–1800 cm^{-1} were recorded using an integration time of 20 s and a spectral resolution of 1 cm^{-1}. To be suitable for Raman analysis, the cells were transferred to a quartz slide and the spectra measured within 1 h of the removal of the culture medium. A Matlab script was used to align the spectra to compensate for any small drift in the laser wavelength over the experimental period. All the spectra were corrected for the quartz coverslip and PBS solution Raman spectrum, by subtracting the background spectrum. The Raman spectra were background corrected by subtracting a third-order polynomial fit. The data were finally normalized with respect to the highest peak (Raman band at 1659 cm^{-1}).

3.6 Statistical analysis

Principal Component Analysis

For data analysis, a program developed in the Matlab platform based on Principal Component Analysis (PCA) was used. PCA is a multivariate technique that operates in an unsupervised manner and is used to analyse the inherent structure of the data [88].

Principal component analysis (PCA) is a statistical procedure that uses an orthogonal transformation to convert a set of correlated variables into a set of linearly uncorrelated variables called principal components (PCs). I will show below a detailed description of PCA using the covariance method.

The aim is to transform a given data set X of dimension p to an alternative data set Y of smaller dimension L << p.

The data are arranged as a set of n data vectors $\mathbf{x_1} \ldots \mathbf{x_n}$ and each $\mathbf{x_i}$ has p columns. We place the row vectors into a single matrix $\mathbf{X}$ of dimensions $n \times p$.

After that, we have to calculate the empirical mean along each dimension j = 1,…, p and place the calculated mean values into an empirical mean vector $\mathbf{u}$ of dimensions $p \times 1$.

$$u\,[j] = \frac{1}{n}\sum_{i=1}^{n} X[i,j]$$

Mean subtraction is an integral part of the solution towards finding a principal component basis that minimizes the mean square error of approximating the data. Therefore, we have to centre the data subtracting the empirical mean vector **u** from each row of the data matrix **X**. Then, we place mean-subtracted data in the $n \times p$ matrix **B**.

$$B = X - hu^T$$

where **h** is an $n \times 1$ column vector of all 1s:

$$h[i] = 1 \qquad \text{for } i = 1, \dots, n$$

At this point, we calculate the $p \times p$ empirical covariance matrix **C** from the outer product of matrix **B** with itself:

$$C = \frac{1}{n-1} B^* \cdot B$$

where the * is the conjugate transpose operator. If **B** consists of real numbers, the "conjugate transpose" is the same as the regular transpose.

To calculate the matrix **V** of eigenvectors which diagonalizes the covariance matrix **C**, we use the following formula:

$$V^{-1}CV = D$$

where **D** is the diagonal matrix of eigenvalues of **C**. Matrix **D** will have the form of an $p \times p$ diagonal matrix, where

$$D[k, l] = \lambda_k \qquad \text{for } k = l$$

is the *j*-th eigenvalue of the covariance matrix **C**, and

$$D[k, l] = 0 \qquad \text{for } k \neq l$$

Moreover, the matrix **V**, which has dimension $p \times p$, contains p column vectors, each of length p, which represent the p eigenvectors of the covariance matrix **C**.

Now, we have to select a subset of the eigenvectors as basis vectors. So, we take the first L columns of **V** and create a new $p \times L$ matrix **W**:

$$W[k, l] = V[k, l] \quad \text{for} \quad k = 1, \dots, p \qquad l = 1, \dots, L$$

where $1 \leq L \leq p$.

The Principal Components (PCs) correspond to linear combinations of the original variables, which are orthogonal to each other and designed in such a way that each one successively accounts for the maximum variability of the dataset. The final step is to project the original data onto new eigenspace and when the PC scores are plotted they

can reveal relationships between samples (groupings).

Leave-one-out cross validation

The leave-one-out method was used for cross validation of the model. In this method, we performed PCA of the whole dataset without one spectrum. The resultant model was used to predict the classification of the left-out sample spectrum. This cross validation approach was used for each spectrum in the set, and we constructed a confusion matrix that summarizes the correct and incorrect spectra classifications [89]. Each row of the confusion matrix gives the predicted classification for a specific cell type. The diagonal terms of the confusion matrix give the number of correct predictive classifications, and by taking into account the mean of these values, it is possible to obtain information on the efficiency of the method.

Empirical approach

Non-parametric diagnostic algorithms based on peak intensities, spectral bandwidths, and/or peak ratios have been widely employed in literature to correlate the variations of cell spectra with cancer cells in a simple and straightforward fashion [36][74][90]. In this thesis, the empirical diagnostic algorithm based on the ratio of the Raman peak intensity at 1447 cm^{-1} for CH2 proteins/lipids to the peak intensity at 785 cm^{-1} for DNA was selected for cell classification. The unpaired Student's t-test was used to test the difference of Raman intensity ratio (I_{1447}/I_{785}) between normal and leukemia cells.

3.7 Confocal Raman imaging (Xplora Horiba)

The inverted confocal Xplora microscope (Horiba, Jobin Yvonne) has been used for micro-Raman imaging experiments. The inverted confocal microscope is coupled to a full Raman module mounted above which includes: three laser sources, a 200 mm focal length spectrograph and a CCD camera.

The different excitation wavelengths are supplied by three internal lasers:

- A 532 nm solid state laser, maximum power 25 mW;
- A 638 nm diode laser, maximum power 30 mW;
- A 785 nm diode laser, maximum power 100 mW.

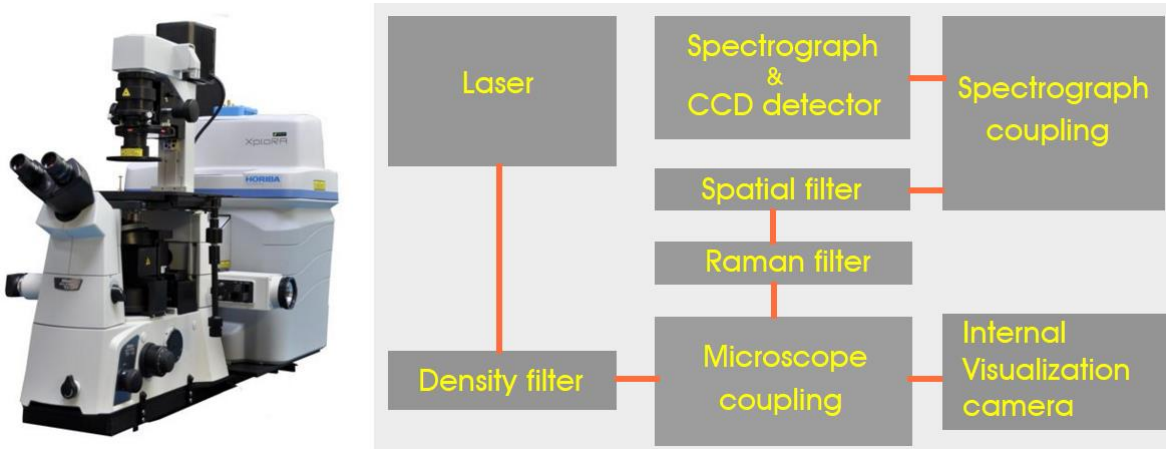

Figure 20: *XploRA inverted Raman microscope.*

The optical path is split into two parts: the illumination (laser) path and the collection (Raman signal) path (Figure 20). On the incoming laser path, the laser beam is reflected toward the microscope (Nikon, Ti-2000 Eclipse Series, including three objectives: 10x, NA = 0.3; 60x water immersion, NA = 1.2; 100x oil immersion, NA = 1.25) by the use of a special filter (dielectric edge rejection filter). It is used in injection/rejection mode which firstly directs the laser into the microscope and then filters out the Rayleigh scattered light as it returns to the spectrograph allowing only the Raman scattered light alone to be transmitted through to the confocal hole (motorized confocal pinhole with four allowed positions: 100, 300, 500 nm) and the entrance of the spectrograph (entrance slit positions: 50, 100, 200 µm). The integrated spectrometer is an asymmetric Czerny Turner design (F = 200 mm), which is optimized for a flat field output and with minimal optical aberrations. The following gratings are mounted on four position kinematic interchangeable grating turret: 600 gr/mm, 1200 gr/mm, 1800 gr/mm and 2400 gr/mm. This set of 4 gratings is used to cover the full spectral resolution and range of the instrument when configured with three lasers. In Table 5, dispersion, resolution and cut-off characteristics of the system are summarized.

A motorized XY stage (Stage travel 100mm x 120mm, steps= 100 nm) is used to move the sample under microscope.

The camera is an open-electrode CCD (Andor, iDus DU420A-OE325, 1024x255 pixels) cooled at –80°C. In Figure 21 the CCD quantum efficiency is reported.

Table 5: *Scheme of the dispersion, resolution and cut-off characteristics of the Xplora system.*

- **Dispersion:**

	532 nm	638 nm	785 nm
2400 gr./mm	6.5 cm^{-1}/mm	3.8 cm^{-1}/mm (restricted range)	NA
1800 gr./mm	9.2 cm^{-1}/mm	6.1 cm^{-1}/mm	4.2 cm^{-1}/mm (restricted range)
1200 gr./mm	14.2 cm^{-1}/mm	10 cm^{-1}/mm	6.5 cm^{-1}/mm
600 gr./mm	28.4 cm^{-1}/mm	20 cm^{-1}/mm	13 cm^{-1}/mm

- **Resolution (50 µm slit): from 2 cm^{-1} to 15 cm^{-1}**
  - With 532nm wavelength: ≤1.4 cm-1 with 2400 grooves/mm average measured between 2300- 3200cm-1
  - With 633nm wavelength: ≤ 1.2 cm-1 with 2400 grooves/mm average measured between 800 -1600cm-1
  - With 785nm wavelength: ≤ 1.2 cm-1 with 1800 grooves/mm average measured 1000-1600cm-1
  - Confocal resolution: ≤ 500nm lateral XY (with 532nm) and test sample
- **Cut-off:**
  - 532 nm: <60 cm^{-1}
  - 633 nm: <50 cm^{-1}
  - 785 nm: <50 cm^{-1}

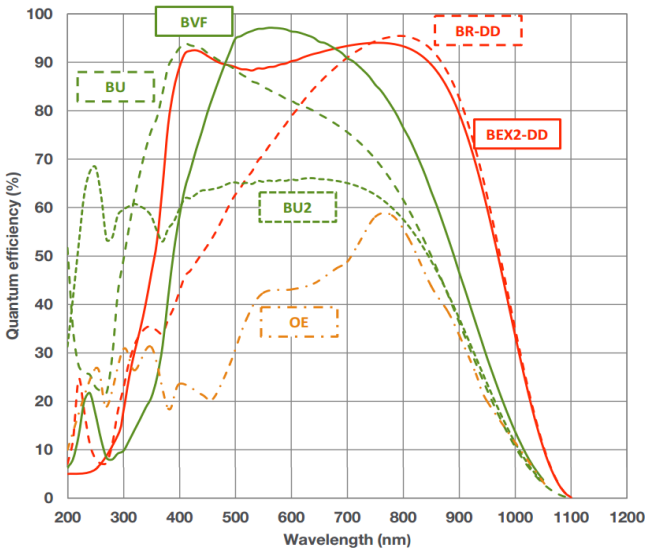

Figure 21: *Quantum efficiency of Andor OE-CCD camera (yellow curve).*

3.8 Immunofluorescence microscopy

Immunofluorescence (IF) microscopy is a relevant technique generally used to assess both the localization and expression levels of proteins of interest in cells. This technique

uses the antibodies to label a specific target antigen with a fluorescent dye (fluorophors or fluorochrome), and therefore allows to display the distribution of the target molecule through the sample by using a fluorescence microscope. Immunofluorescence can be used on tissue sections, cultured cell lines, or individual cells, and may be used to analyse the distribution of proteins and small biological and non-biological molecules. Moreover, it can be used in combination with non-antibody methods of fluorescent staining, for example, DAPI or Hoechst to label DNA. Several microscope designs can be used for analysis of immunofluorescence samples: epifluorescence and confocal microscope are the most widely used.

There are two categories of immunofluorescence techniques, primary (or direct) and secondary (or indirect). Primary immunofluorescence uses a single, primary antibody, chemically linked to a fluorophore. The primary antibody recognizes the target molecule (antigen) and binds to a specific region. After a laser light excites the attached fluorophore, it will emit a specific wavelength and can be detected by fluorescence microscopy. Secondary immunofluorescence uses two antibodies; the unlabelled first (primary) antibody specifically binds the target molecule, and the secondary antibody, which binds the fluorophore, recognizes the primary antibody and binds to it. This protocol is more complex and time consuming than the primary protocol but allows more flexibility because a variety of different secondary antibodies can be used to bind a specific primary antibody [91].

In the following paragraphs, I will describe the secondary immunofluorescence protocols used for the leukemia cell preparations and some details concerning the confocal imaging analysis.

3.8.1 Sample preparation

The three B-ALL cell lines, RS4;11 (6×10^4), REH (1×10^5), and MN60 (3×10^4), were suspended in 1 mL culture medium, plated onto 15-mm coverslips in a 24-well plates for 24 h, and then fixed with 2% paraformaldehyde (supplemented with 2 μg/mL Hoechst 33342, as the DNA dye) overnight at 4 °C. The cells were washed three times with phosphate-buffered saline (PBS), incubated in blocking solution (0.5% BSA, 0.05% saponin, 50 mM NH_4Cl, in PBS, pH 7.4) for 20 min at room temperature, and then incubated with the specified antibodies (CD38 1:50; CD20, CD19 1:10) diluted in blocking solution, overnight at 4 °C. After three washes with PBS, the cells were incubated with an Alexa 546-conjugated anti-mouse goat antibody (1:400 diluted in blocking solution) for 45 min at room temperature, and then washed again three times

with PBS and twice with sterile water, to remove salt. The coverslips were mounted on glass microscope slides with Mowiol.

3.8.2 Immunofluorescence confocal imaging

Figure 22: *Confocal Zeiss inverted LSM700 microscope*

Confocal images were acquired and analyzed using an inverted confocal microscope system (Zeiss LSM700; Carl Zeiss) with a 63x oil-immersion objective with a resolution of 1024 × 1024 pixels, with the files exported as Tiff files (Figure 22). The images were cropped and optimized for brightness and contrast with Photoshop, and composed using Illustrator (Adobe Systems).

3.9 Western blotting

Western blotting is a widely used analytical technique detecting specific proteins in a tissue homogenate or cellular extract. In this technique a mixture of proteins is separated depending on molecular weight, and thus by type, through gel electrophoresis. The proteins are then transferred to a membrane (typically nitrocellulose or PVDF), producing a band for each of them. The membrane is then incubated with labels antibodies specific to the protein of interest. The unbound antibody is washed off while the bound antibodies are then detected by developing the film. As the antibodies only bind to the protein of interest, only one band should be visible. The thickness of the band corresponds to the amount of protein present [92].

In the following paragraph, I will present the Western blotting protocol used for the leukemia cell preparations.

3.9.1 Sample preparation

RS4;11 (6 ×104), REH (1 x105), and MN60 (3 ×104) cells were suspended in 2 mL cultured medium in 6-well plates for 72 h and then lysed with 100 µL Laemmli buffer. The total proteins were separated on 10% SDS-PAGE, transferred onto nitrocellulose, and subjected to Western blotting. The nitrocellulose filters containing the proteins of interest were incubated in TTBS buffer [0.05% (w/v) Tween 20, 150 mM NaCl, 20 mM Tris-HCl, pH 7.5, supplemented with 1% (w/v) BSA] for 1 h at room temperature, and then with the primary antibody (CD38, 1:1000; CD10, 1:250; CD19, 1:500 in the same buffer) for overnight incubations at 4 °C. The primary antibodies were then removed and the strips were washed twice in TTBS, for 10 min each. The strips were incubated for 1 h at room temperature with the HRP-conjugated anti-mouse secondary antibody (1:5,000 in TTBS buffer), washed twice in TTB for 10 min each, and twice in TBS buffer (150 mM NaCl, 20 mM Tris-HCl pH 7.5). After washing, the strips were processed for ECL-based detection, according to the ECL reagents manufacturer instructions.

3.10 Flow Cytometry

Flow Cytometry is a biophysical technology employed to measure and analyse multiple physical and chemical characteristics of single particles, usually cells in liquid samples, as they flow in a fluid stream through a light beam.

A flow cytometer is made up of three main systems: fluidics, optics, and electronics.

- The fluidics system transports particles in a stream to the laser beam for the detection.
- The optics system consists of one or more lasers to illuminate the particles in the sample stream and optical filters to direct the resulting light signals to the appropriate detectors.
- The electronics system converts the detected light signals into electronic signals that can be processed by the computer.

A flow cytometer is able to analyse any suspended particle or cell (from 0.2 to 150 um) and can measure important features including size, granularity or internal complexity, and relative fluorescence intensity. In the flow cytometer a laser beam (usually a 488nm

Argon ion laser) is directed onto a stream of fluid; when particles pass through the laser beam, they scatter laser light. A number of detectors are placed at the point where the stream passes through the light beam: a detector in line with the light beam (Forward Scatter or FSC) and several ones perpendicular to it (Side Scatter (SSC) and one or more fluorescent detectors (FL-1, FL-2, FL-3 and so on) (Figure 23).

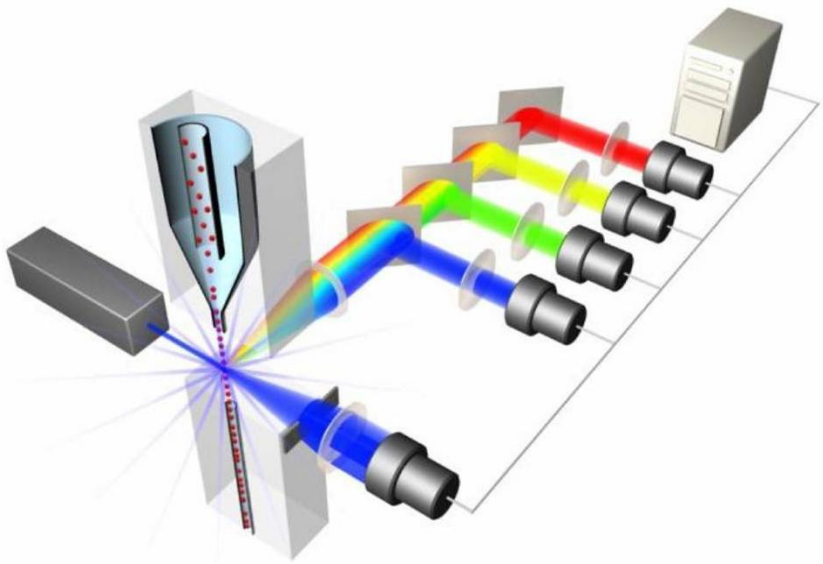

Figure 23: *Working diagram of a flow cytometry system.*

The detectors collect the scattered and fluorescent light and it is then possible to obtain a lot of information about the physical and chemical structure of each individual particle [93][94].

Forward Scatter light (FSC) is proportional to cell-surface area or size and represents mostly the diffracted light. Side-scattered light (SSC) is proportional to cell granularity or internal complexity and represents mostly the refracted and reflected light that occurs at any interface within the cell (SSC detector is at 90 degrees to the laser beam). Correlated measurements of FSC and SSC can allow for differentiation of cell types in a heterogeneous cell population. Major leucocyte subpopulations residing in human peripheral blood can be differentiated using FSC and SSC (Figure 24).

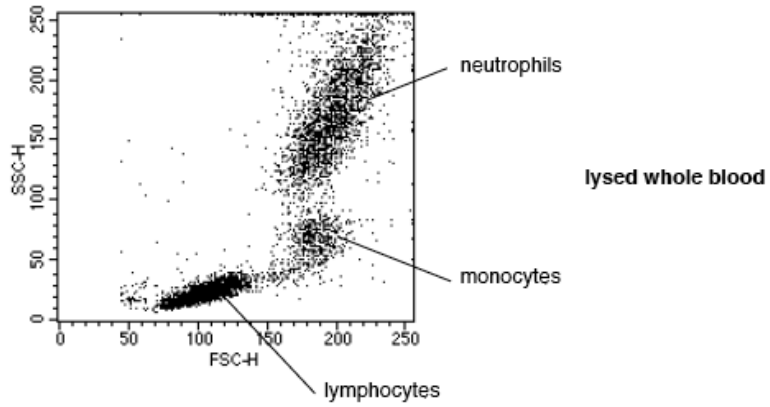

Figure 24: *Leucocytes differentiation by FSC and SSC signals.*

The ability of flow cytometry to distinguish different cellular populations is the reason why it is routinely used in the diagnosis of health disorders, especially blood cancers, but has many other applications in basic research, clinical practice and clinical trials [95].

In the next section, I will show the protocol used for flow cytometry analysis on leukemia cells. These procedures were performed at the IRCCS SDN laboratory, in Naples.

3.10.1 Sample preparation

RS4;11, REH and MN60 cell lines, 2 x10^5 cells were diluted in 100 µL of DPBS buffer supplemented with 1% BSA and incubated at 4°C for 30 min with appropriate amount of monoclonal antibodies, following the manufacturer instructions (provided by Beckman-Coulter). The combination of antibodies used are: i) anti-CD20 Fluorescein isothiocyanate with anti-CD19 Phycoerythrin; and ii) anti-CD10 Phycoerythrin with anti CD38 Phycoerythrin;-Cy7. All antibodies for flow cytometry analysis were provided from Beckman-Coulter. After incubation with these monoclonal antibodies, the cells were washed in DPBS with 1% BSA and diluted in 500 µL of the same solution for flow cytometry acquisition. At least 20.000 events were recorded for each experimental point on a FC-500 flow cytometer (Beckman-Coulter). Cells stained with irrelevant monoclonal immunoglobulin reagents conjugated with the same fluorochromes were used as negative controls.

4

Diagnosis and classification of B-ALL cells

Acute lymphoblastic leukemia (B-ALL) is a neoplastic disorder that shows high mortality rates due to immature lymphocyte B-cell proliferation. B-ALL diagnosis requires identification and classification of the leukemia cells. Here, I will describe the use of Raman spectroscopy to discriminate normal lymphocytic B-cells from three different B-leukemia transformed cell lines (i.e., RS4;11, REH, MN60 cells) based on their biochemical features. In combination with immunofluorescence and Western blotting, I will show that these Raman markers reflect the relative changes in the potential biological markers from cell surface antigens, cytoplasmic proteins, and DNA content and correlate with the lymphoblastic B-cell maturation/differentiation stages.

4.1 Introduction

Acute lymphoblastic leukemia type B (B-ALL) is a hematological malignancy that is characterized by uncontrolled and rapid cell proliferation of immature B-cell progenitors (i.e., lymphoid or lymphoblastic cells) that cannot mature properly into lymphocytic B cells [1][2]. Thus, its timely and accurate diagnosis is fundamental for successful clinical treatment.

A firm diagnosis of B-ALL requires first the identification of the leukemia cells, and second their classification based on the differentiation/maturation stage in which the lymphoblastic B cells are blocked, as above described (paragraph 1.3.1):

(i) L1 blasts, with small and homogenous cell size, high nuclear/cytoplasmic ratio, and unclear nucleoli;
(ii) L2 blasts, with medium cell size, lower nuclear/cytoplasmic ratio, with one or more visible nucleoli; and
(iii) L3 blasts, with larger and pleomorphic cell size, prominent nucleoli, and abundant cytoplasm.

However, in some cases of poorly differentiated B-ALL, morphological assessment provides low sensitivity and equivocal results [3]. Although most cases can be diagnosed by this method, there is only a modest correlation between morphological categories, treatment responsiveness, and prognosis [3].

As a consequence, this morphological approach can be combined with immunophenotypic B-ALL cell analysis of the arrested stage of B-cell maturation in terms of the surface expression of up to six to eight different B-cell–associated antigens by multi-parametric flow cytometry, as above quoted (paragraph 1.3.2) [25][26][27][28].

However, this immunophenotypic analysis requires a panel of antibodies against several lymphoid-expressing antigens, and it is labor intensive and time consuming. Moreover, the use of fluorescent dyes is frequently limited by photobleaching of the dye molecule, the limited ability to detect multiple dyes, and interference with the fluorescence of the routine stains used in the cell morphology assessment [29]. Therefore, new approaches are required for rapid and sensitive diagnosis, classification, and prognosis of leukemias.

In the present chapter, I will demonstrate that RS can be used to identify and classify three B-leukemia cell types that closely mimic the different differentiation/maturation stages of B-ALL cells (i.e., RS4;11, REH, MN60 cells) versus their normal B-cell counterparts.

4.2 Morphological and immunophenotypic identification and classification of B-ALL cells

The first two cell models that I used were originally derived from patients with B-ALL: the RS4;11 and REH cell lines, which are both classified as the L2-blast (i.e., B-cell precursor leukemia) subtype [81][82][83][113][114]. The third cell model was the MN60 cell line, which represents a more differentiated B-ALL cell type, as it is

classified as the L3-blast (i.e., B-cell leukemia) subtype [115][116][117]. To define these cell lines further, I initially carried out immunophenotypic and morphological characterization of the expression profiles of the sequential plasma-membrane antigens of these cell lines, as summarized in Figure 25.

a

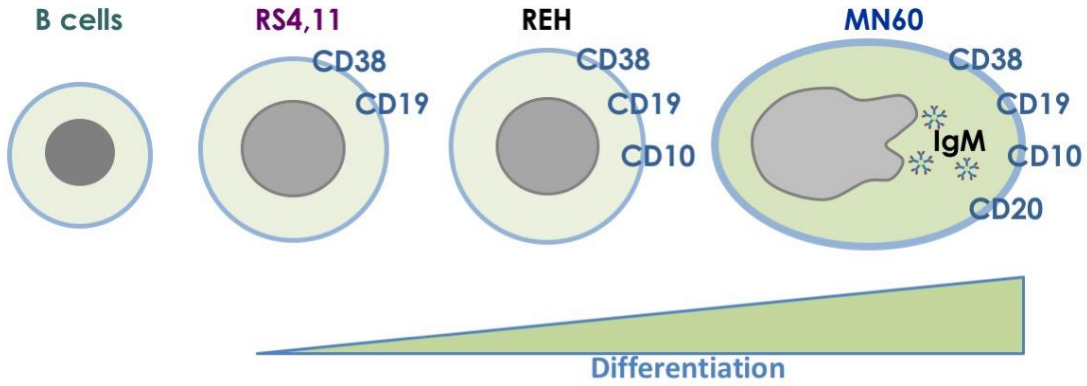

b

Cell type	RS4;11	REH	MN60
Cell size	small	small/medium	medium/large
Nucleus	• regular shape • finely dispersed chromatin • one/more nucleololi	• regular/indented shape • finely dispersed/coarsely condensed chromatin • one/more nucleololi	• irregular/lobulated shape • finely stipped/homoheneus chromatin • prominent, two/more nucleololi
Cytoplasm	• scanty/moderately abundant • variable vacuolation • slight/moderate basophilia	• scanty/moderately abundant • variable vacuolation • variable/deep basophilia	• moderately abundant • prominent vacuolation • Very deep basophilia
CD expression	**CD38+, CD19+** CD10-, CD20-, CD37-, CD80- sm/cylgM-	**CD38+, CD19+, CD10+,** CD20-, CD37-, CD80- sm/cylgM-	**CD38+, CD19+, CD10+,CD20+, CD37+, CD80+** **sm/cylgM+**

c

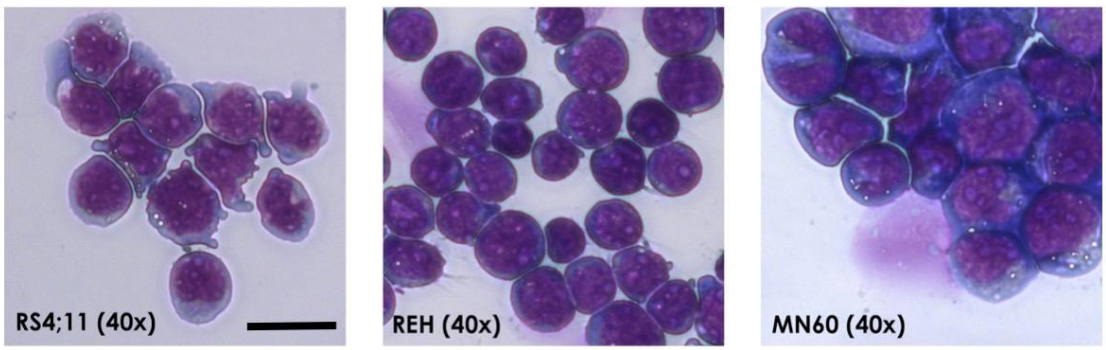

Figure 25: Differentiation scheme and morphology of the RS4;11, REH and MN60 B-leukemia cell lines. *(a) Immunophenotypic profile with the coordinate and sequential well-characterized plasma-membrane antigen expression. (b) Morphologic features and immunophenotypic expression pattern. (c) Representative images of the cell morphology using May Grunwald-Giemsa histochemical staining for DNA and RNA molecules. Scale bar: 10 µm.*

Thin-layer of the RS4;11, REH and MN60 B-leukemia cells for morphological analysis were prepared using a cytocentrifuge (Thermo Scientific Shandon Cytospin4; Thermo Fisher Scientific Inc, USA) according to manufacturer instructions, and then stained using the May-Grunwald-Giemsa staining protocol (SIGMA-Aldrich, St. Louis, MO, USA). The cells were then examined under light microscopy at 40× magnification for the morphological analysis. The RS4;11 and REH B-leukemia cells showed small to medium nuclear size, with a regular shape, finely dispersed chromatin, and one or more nucleoli. The cytoplasm was scanty, with slight or moderate staining and variable vacuolation. Instead, the MN60 B-leukemia cells showed medium to large nuclear size, with an irregular and lobulated shape, finely stippled chromatin, and two or more prominent nucleoli. There was moderately abundant cytoplasm, with prominent vacuolation and very deep staining, typical of the L3 subtype B-ALL cells (Figure 25b-c).

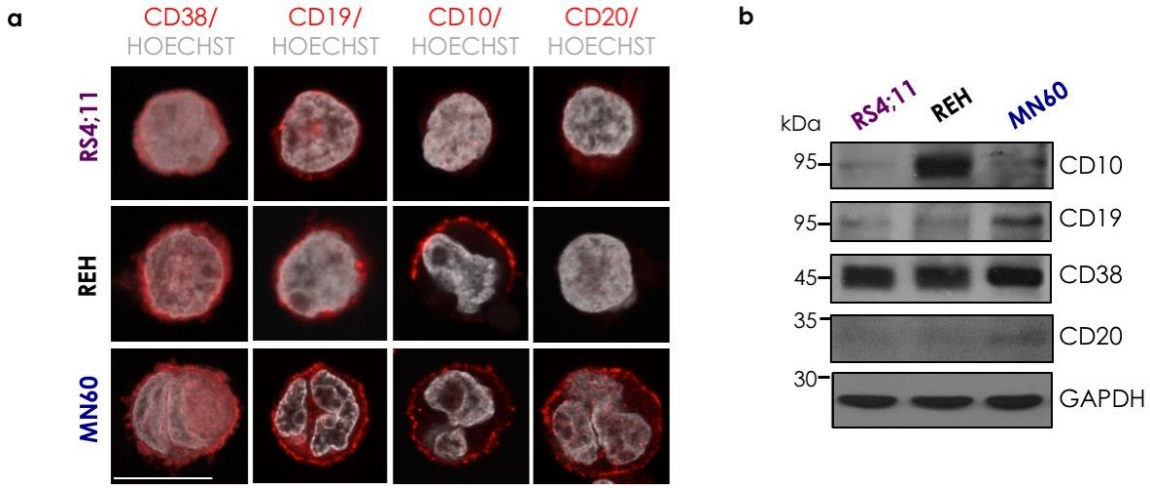

Figure 26: Identification and classification of acute lymphocytic leukemia cells. *(a) Representative confocal microscopy images of RS4;11, REH and MN60 B-leukemia cells fixed and processed for immunofluorescence analysis with anti-CD38, anti-CD19, anti-CD10 and anti-CD20 monoclonal antibodies (red), to monitor their expression levels. Gray, Hoechst-33258 nucleic-acid staining. Scale bar: 10 μm. (b) Representative immunoblotting of RS4;11, REH and MN60 cells with antibodies against CD10, CD19, CD20 and CD38 (as indicated). Glyceraldehyde 3-phosphate dehydrogenase (GAPDH) is shown for the internal protein levels and molecular weight standards (kDa) are indicated on the left of each panel. The blots have been run under the same experimental conditions.*

Using the well-defined quadruple CD38/ CD19/ CD20/ CD10 staining for leukemia cells [118][119], I first examined these cells under confocal fluorescence microscopy and by Western blotting (Figure 26). CD38 and CD19 were expressed on the surface of the plasma membranes of all of these three cell lines, and their expression increased for

the different differentiation stages from RS4;11 and REH cells to MN60 cells. CD20 was expressed only on the plasma membranes of the more differentiated MN60 cells [1][117] (Figure 26**Errore. L'origine riferimento non è stata trovata.**). Finally, CD10 expression increased for the differentiation from RS4;11 to REH, and then decreased in MN60 cells, as already described for the L2-blast and L3-blast subtypes [1][117]. These immunophenotypic analyses validated the RS4;11 and REH cells as a model for the L2 subtype and the MN60 cells as a model for the L3 subtype of B-ALL cells.

4.3 B-cell purity assessment

The purity of the B-cells was measured using flow cytometry after the cells had been stained with a fluorochrome-conjugated antibodies mix composed of: anti-CD45 (pan-leucocyte marker) conjugated with fluorescein isothiocyanate; anti-CD56 (natural killer cell marker) conjugated with Rodamine-1; anti-CD19 (B-cell marker) conjugated with phycoerythrin-Texas Red conjugate; and anti-CD3 (T-cell marker) conjugated with phycoerythrin-cyanine5 tandem. These antibodies were from Beckman-Coulter. The fluorescence intensities were measured with a flow cytometer (FC-500; Beckman-Coulter, Milan, Italy), according to the manufacturer instructions. Forward scatter and side scatter gates were established to exclude dead cells and cell debris. The percentage of B-cells (CD19+/CD45+), T-cells (CD3+/CD45+) and NK-cells (CD56+/CD45+) were assessed before the immunomagnetic procedure, as shown in Figure 27a, c and e, respectively. The percentage of B-cell enrichment was verified after the immunomagnetic separation procedure, according to Figure 27b. Contamination by T-cells and NK-cells was also determined (Figure 27d and f, and it was always negligible (<1.0%).

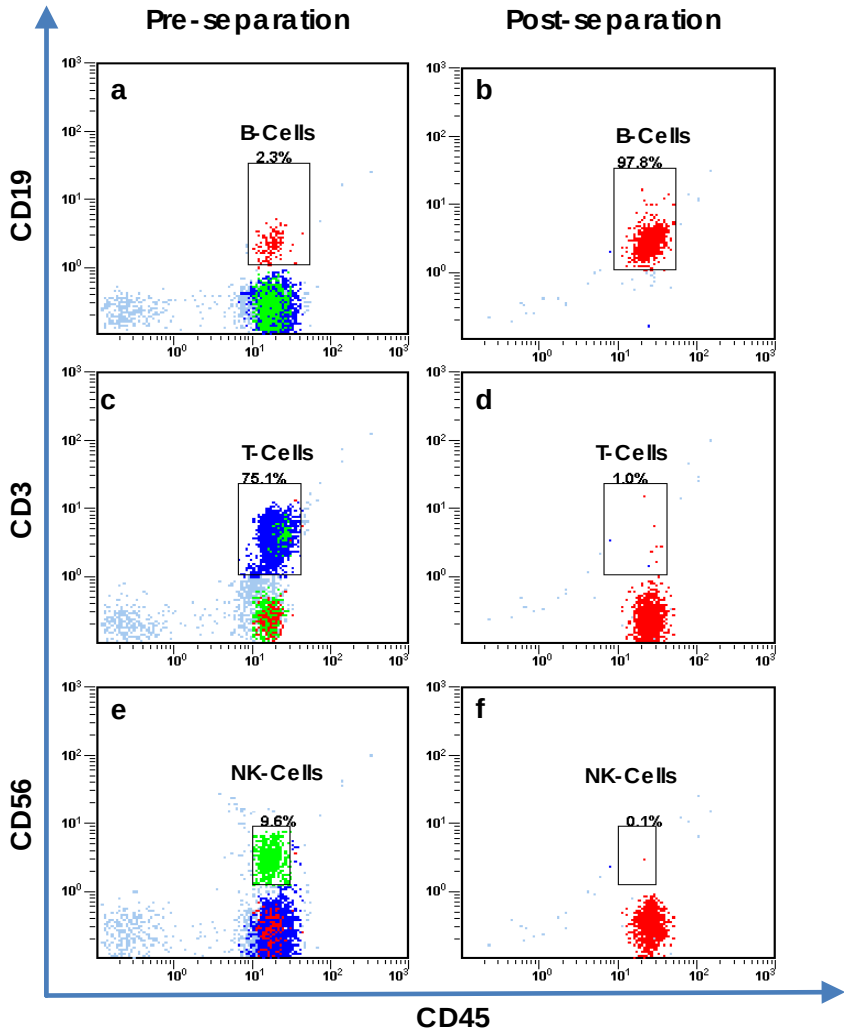

Figure 27: Dot plots for the determination of human B-lymphocyte purification by flow cytometry. *The percentage of B-cells (a, b, CD19+/CD45+, red events), T cells (c, d, CD3+/CD45+, blue events), and natural killer (NK) cells (e, f, CD56+/CD45+, green events) determined by flow cytometry, as pre-separation and post-separation through negative immunomagnetic selection. The content of the B-lymphocytes in the purified enriched fraction was routinely about 98% (as indicated) in all of the samples analyzed.*

4.4 Preliminary Raman spectra reproducibility analysis

Spectra obtained from nucleus, cytoplasm and membrane of the studied cells (B-cells and RS4;11, REH and MN60 B-leukemia cells) were preliminary analyzed. Figure 28 shows MN60 nucleus, cytoplasm and membrane spectra. The spectra have been calculated by acquiring three different spectra from the nucleus, cytoplasm and membrane within a cell and repeating the measurements on 20 different cells. The three spectra contain specific features for those regions of the cells, providing an intrinsic check for the region inside a cell from where the spectrum was obtained. However, no

qualitative differences were observed between spectra obtained from different cells or different nucleus, cytoplasm and membrane regions within a cell.

Moreover, it was possible to detect differences in the biochemical composition between nucleus, cytoplasm and membrane regions. The Raman spectrum of nucleus showed significant spectral features previously assigned to nucleic acid contributions such as the ring breathing modes of the nucleic acid bases (730 cm^{-1} adenine ring breathing, 780 cm^{-1} uracil, cytosine and thymine ring breathing, 1120 cm^{-1}, 1370 cm^{-1} and 1578 cm^{-1} guanine and adenine contributions) and from the O-P-O backbone (788 cm^{-1} and 1095 cm^{-1}) (Figure 28b - gray band). Additionally, the Raman spectrum of cytoplasm is characterized by intense vibrational bands in the spectral region around 1300-1350 cm^{-1} and 1400-1500 cm^{-1} (Figure 28b - cyan band) that have contributions from proteins and to a minor extent also from carbohydrates. The noisier Raman spectrum of membrane reveals strongest Raman peaks of lipids that are present at 1449 cm^{-1}, 1301 cm^{-1} (CH vibrations) and 1660 cm^{-1} (C=C stretching) and belong to vibrations of the hydrocarbon chains.

The position of the laser, during acquisition, was focused on the cell nucleus, as this is where the most relevant information is likely to originate, although with large volume, the system should also partially examine the membrane and cytoplasm above and below the nucleus. However, in the nuclear region slightly differences (about 5%) in the intensity ratio I_{1447}/I_{785} (representative of protein-DNA ratio) were found (Figure 28c).

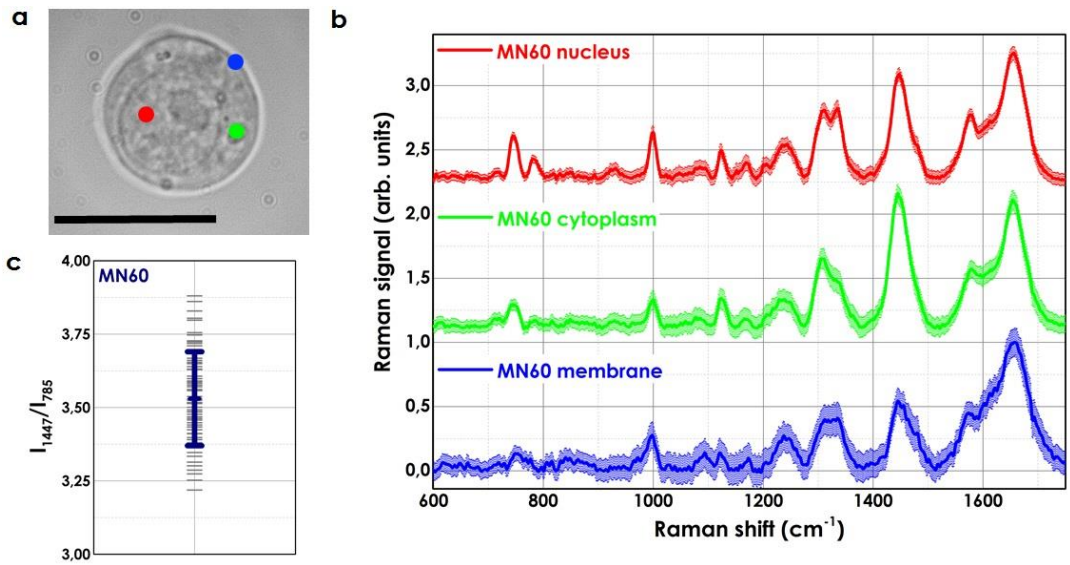

Figure 28: *(a) Representative optical image of MN60 B-leukemia cell. The Raman probe location during the spectra acquisition is also shown. Scale bar: 10 µm. (b) Mean Raman spectra of nucleus, cytoplasm and membrane of MN60 B-leukemia cells. Each spectrum is an average of 60 acquisitions. (c) Intensity ratio of the Raman signals at 1447 cm^{-1} and 785 cm^{-1}.*

A comparison of bright field image and false colour Raman image of MN60 B-leukemia cell is shown in Figure 29.

Before the Raman imaging, the sample was fixed with 0,4% paraformaldehyde (PFA) and was successively washed with PBS; for the Raman measurements, $1x10^6$ cells were suspended in 500 µl of PBS and coated onto quartz slides.

Raman image of the cell was recorded with an inverted confocal Xplora microscope (Horiba, Jobin Yvonne) equipped with a 600 gr/mm grating. The Raman signal was excited with a 532 nm diode laser, focused onto the cell through a 60x water immersion objective (Nikon, Ti-2000 Eclipse, NA = 1.2) and with a power of about 5 mW in the object plane. The Raman image was recorded by raster scanning the cell (square area 15 x 15 µm) trough the laser focus, with a step size of 0.4 µm, and acquiring a full spectrum (integration time of 0.5 s) at each position. A total of 2500 spectra were collected in almost 30 minutes. Specific spectral regions were used to reconstruct the false colour Raman map reported in Figure 29. Raman images in the spectral region between 700-800 cm^{-1} (in red) overlaps with the nuclear region of the cell, as visible by the comparison with the bright filed image of the MN60 cell. This indicates a significant presence of nucleic acids in this area. Raman map in the spectral region between 2800 cm^{-1} and 3000 cm^{-1} (in yellow) overlaps with cytoplasmic vesicle content. This is not surprising since vesicle are reach in phospholipids. The cell membrane Raman map (in blue) is additionally shown in Figure 29.

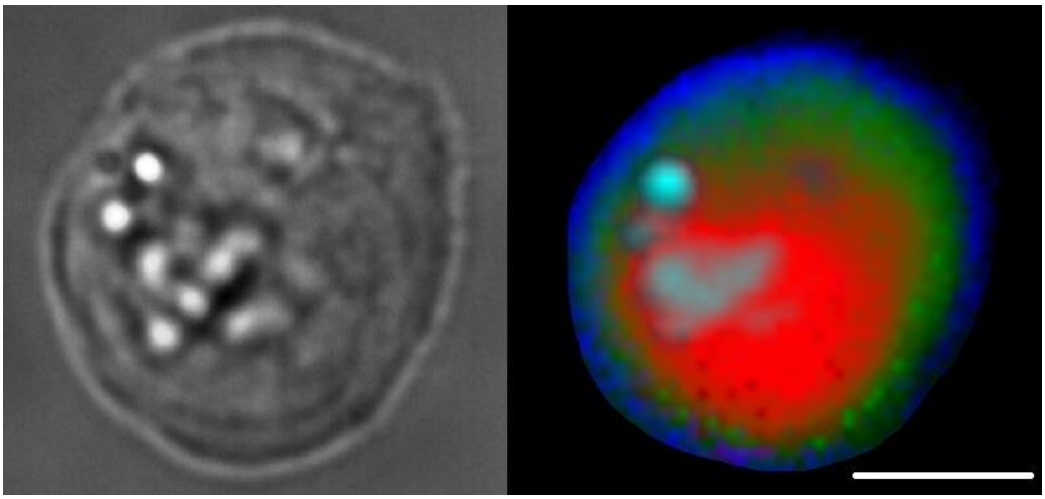

Figure 29: *Bright field image (left) and reconstructed Raman image (right) of a MN60 B-leukemia cell. Nucleic acid and proteins content is represented in red colour, the cytoplasmic vesicles in yellow colour. The blue colour corresponds to the background (extracellular region). Scale bar: 5 µm.*

4.5 Raman identification and classification of B-ALL cells

To evaluate the RS signatures that might specifically identify differences in the biochemical compositions of these L2 and L3 B-leukemia cells versus their normal B-cell counterpart purified from human peripheral blood, I acquired Raman spectra from these RS4;11, REH and MN60 transformed B-leukemia cells and from B lymphocytes (Figure 30) [120]. More than three hundred spectra for each cell type were recorded and evaluated.

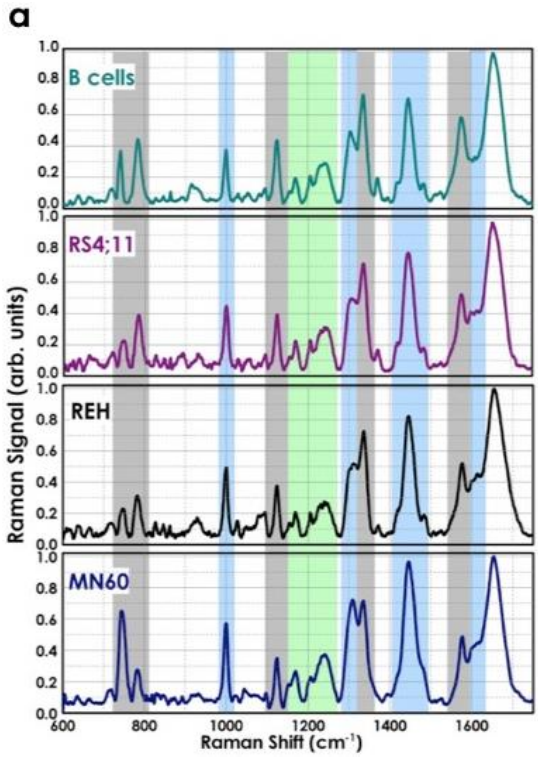

b

Raman band(cm^{-1})	Assignment	Classification
678	G, C-C twist	NA/P
720	A, C-C twist	NA
743	T, U	NA
746	T, C	NA
785	T, C, DNA bk	NA
929	BK, deoxyrib., C-C	NA/P
1004	Phe, C-C	P
1120	O-P-O sym str., BK	NA
1157	C-N str., C-C	P/L
1206	Amide III, =CH def	P/L
1252	Amide III, =CH def	P/L
1310	G, Amide III, CH_2	NA/P/L
1337	A,G,C-H def.	NA/P
1370	A,T,G	NA
1420	CH def., CH_3	P/L
1447	CH def	P/L
1485	A,G, CH def	NA/P
1510	A, CH def	NA/L
1577	A,G	NA
1607	Phe, Tyr, C=C	P
1617	Tyr, Trp, C=C	P
1659	Amide I, C=C	P/L

Figure 30: Identification and classification of acute lymphocytic leukemia cells. *(a) Mean Raman spectra of normal B lymphocytes and the three analyzed B-leukemia cell lines (as indicated). Each spectrum is an average of 300 cells. (b) Raman spectral classification and assignment [22][23]. Abbreviations: def, deformation; str, stretching; bk, vibration of backbone; sym, symmetric; A, adenine; C, cytosine; G, guanine; T, thymidine; U, uracil (ring breathing modes of DNA/RNA bases); Phe, phenylalanine; Tyr, tyrosine; Trp, tryptophan; NA, nucleic acids, P, proteins; L, lipids.*

The Raman spectrum of lymphocyte B-cells (Figure 30a) contained spectral features of DNA and RNA that arose from the individual bases (i.e., adenine, thymine, cytosine, guanine, uracil), as well as from the sugar-phosphate backbone of DNA (a, gray region; 700-800 cm^{-1}, 1120 cm^{-1}, 1370 cm^{-1}, 1577 cm^{-1}). The RS features of lipids arose from the stretching of the various CH2 and CH3 groups (Figure 30a, green region; 1150-1250 cm^{-1}). The RS features of proteins included contributions from the amide groups of the

secondary protein structures (e.g., α-helices, β-sheets, random coils), aromatic amino acids (e.g., tryptophan, tyrosine, phenylalanine), and stretching or deformation of carbon atoms bonded with hydrogen, nitrogen, and other carbon atoms (Figure 30a, cyan region; 1000 cm^{-1}, 1300-1350 cm^{-1}, 1400-1500 cm^{-1}, 1600-1650 cm^{-1}) [121]. The assignment of the Raman peaks is given in Figure 30b [106][120]. To identify the most important spectral differences, the spectra of the B-leukemia RS4;11, REH, and MN60 cells were directly compared to those of the normal B lymphocytes (Figure 30a), and their spectral differences were calculated (Figure 31).

This comparison revealed that these three transformed B-leukemia cell lines showed Raman spectra that were similar to the normal B-lymphocyte counterpart, although with significantly different mean intensities for some specific peaks. The spectra obtained showed negative differences around 785 cm^{-1}, 1370 cm^{-1}, and 1577 cm^{-1}, which are due to the ring breathing modes in the DNA bases [17][106][120] and near 1120 cm^{-1}, which is due to the symmetric PO2− stretching vibration of the DNA backbone [17][106][120] (Figure 31). Additionally, the MN60 Raman spectra revealed higher intensity of the peak around 743 cm^{-1}, which is generally assigned to RNA bases [13][106][120] (Figure 31). Positive difference peaks were also seen at 1420-1485 cm^{-1} (CH proteins/ lipids), 1310 cm^{-1} (amide III band), 1337 cm^{-1} (CH proteins/ nucleic acids), 1607-1617 (C=C vibrations), and 1650 cm^{-1} (amide I band) [13][17][106][120][122] (Figure 31). It can also be noted that the magnitudes of these changes generally appeared more pronounced from the RS4;11 to the MN60 cells (Figure 31). Therefore, the intensity variations in these specific Raman peaks appear to correlate well with the differentiation/maturation stages of these B-leukemia cells.

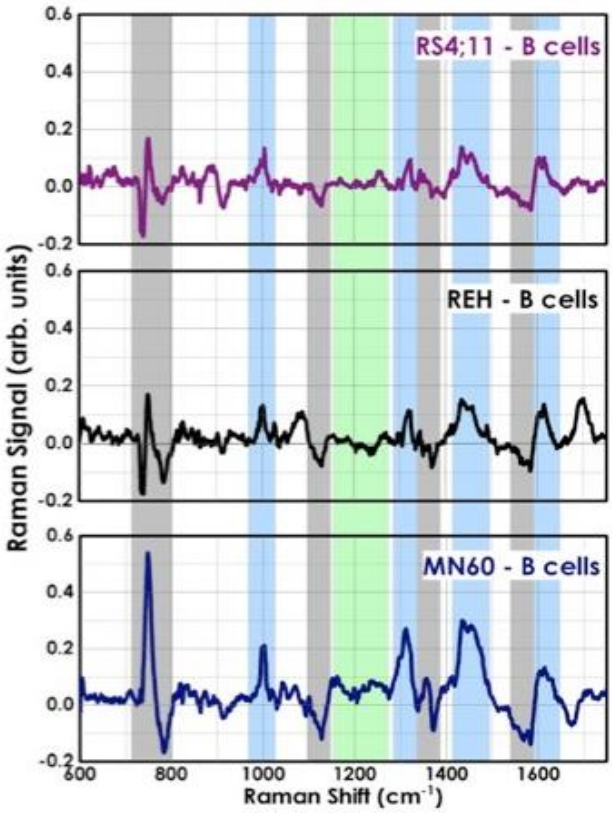

Figure 31: *Difference spectra between acute lymphocytic leukemia cells and normal B-cells.*

4.6 Principal component analysis for the Raman spectra

To define the efficiency and sensitivity of the proposed approach for single-cell cancer diagnosis and classification, I combined the RS analysis with a multivariate statistical method: PCA [123]. In the spectral range from 600-1800 cm^{-1}, each Raman spectrum consists of 1200 variables at 1 cm^{-1} spacing; however, only a fraction of these contain useful information for this cell classification. PCA was performed on the spectral data to define the new dimensional space in which the major data variance can be detected and represented by a few relevant parameters, known as the principal components (PCs). These PCs form a model through which the RS signal of individual cells can be assigned a score. Therefore, PCA can provide a chart of the PCA scores of individually analyzed cells where similar Raman spectra cluster together [13][120][121][123][124]. Indeed, the combination of RS with several multivariate statistical methods has been successfully applied to discriminate between healthy and cancerous tissues, as well as between healthy and tumorigenic cells [13][15][120][121][124].

Here, the first three PCs (PC1-3) accounted for close to 98% of the total variance, and so I used these to generate scatter plots, where the clusters of points represented different

cell groupings (Figure 32a). The significance of these selected PCs was initially evaluated in an analysis of the loading values, where they showed the largest deviations from zero. This PCA analysis shows that when PC2 and PC3 were plotted against PC1, these three B-leukemia cell types and the normal B-lymphocyte counterpart formed four distinct and well-defined groups (Figure 32a). The main result of this statistical analysis was then the creation of the confusion matrix that corresponds to the leave-one-out predictive classification for these normal and leukemia cells (Figure 32b) [124]. Here, the diagonal values of this confusion matrix indicate that 1167 out of 1200 cases were classified correctly, which thus resulted in an efficiency of 97.3%.

a

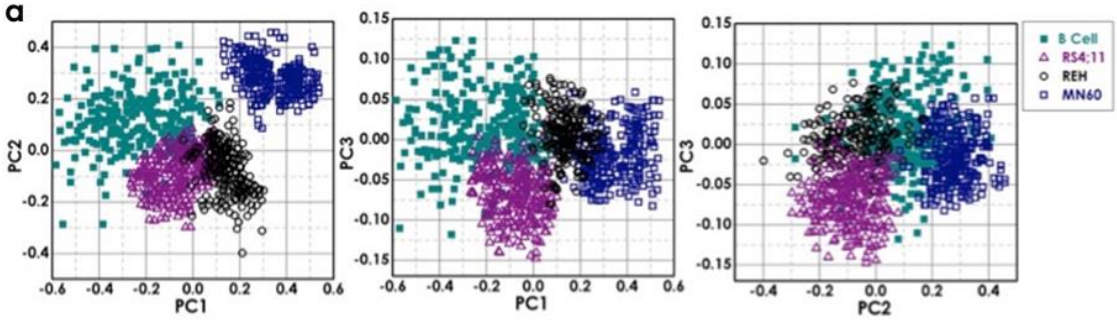

b

	B cells	RS4;11	REH	MN60
B cells	298	1	1	0
RS4;11	3	283	14	0
REH	2	11	**286**	1
MN60	0	0	0	**300**

Figure 32: Identification and classification of acute lymphocytic leukemia cells. *(a) PCA scatter plots comparing control B lymphocytes and B-leukemia cells. (b) Confusion matrix for the classification of the control B lymphocytes and the B-leukemia cells.*

4.7 Discussion and conclusions

This experimental chapter demonstrates the potential application of RS to the identification of three transformed leukaemia cell lines: RS4;11, REH and MN60 cells [1][114]. RS4;11 and REH B-leukemia cells are representative of the L2 B-ALL subtype, and the MN60 B-leukemia cells are representative of the L3 B-ALL subtype, the Raman spectra here reported clearly highlight these differences. For instance, the relative peak intensities at 785 cm^{-1}, 1120 cm^{-1}, 1370 cm^{-1}, and 1577 cm^{-1} (related to DNA bases) were lower in these B-leukemia cells compared to normal B-lymphocytes, which indicates a reduction in the nucleic-acid content of the cells. This effect might be due to breaks in and translocations of several chromosomes (e.g., in REH cells, the X-

chromosome is completely missing [125]) or to chromatin decondensation [126]. Of note, the Raman spectrum of the MN60 B-leukemia cells was slightly different from those of both the RS4;11 and REH B-leukemia cells, which also confirmed that these MN60 B-leukemia cells can be classified as a distinct B-leukemia cell subtype, as indeed is the case based on its more differentiated maturation stage. The Raman spectrum for the MN60 B-leukemia cells showed greater intensity of the peak around 743 cm^{-1}, which would appear to be due to an increase in ribosomal RNA content, which in turn correlates with higher synthesis and content of proteins. Indeed, the morphological assessment of these MN60 B-leukemia cells showed intense cytoplasmic staining that is indicative of the presence of large amounts of ribosomal RNA in the rough endoplasmic reticulum where the biosynthesis of immunoglobulins and other proteins takes place [82][127]. In addition, there were relative increases in the Raman spectra intensities for the bands related to amide III (1310 cm^{-1}), amide I (1650 cm^{-1}), and CH/CC (1337, 1420-1485, 1607-1617 cm^{-1}) proteins, which correlated with the protein structure in these three B-leukemia cell lines. The magnitudes of these peaks increased from the RS4;11 cells to the MN60 cells, in agreement with the extent of expression of plasma-membrane antigens, nucleus/cytoplasm ratio and cytoplasmic immunoglobulins during the B-cell differentiation/maturation process. I also explored PCA here, together with a leave-one-out cross-validation approach, for B-leukemia cell identification and classification [119], which provided a diagnostic efficiency of 97.3% for separating B-leukemia versus normal B-lymphocytes. The PCA also indicated larger spread of the normal B-cell cluster compared to the populations of B-leukemia cells, which was probably due to greater cell-to-cell variation for the different donors of the normal B-lymphocytes. Additionally, the MN60 cluster was completely separated from the others, which again confirms that this model system is more differentiated.

5

Follow-up after chemotherapeutic treatment of B-ALL cells

This study demonstrates the potential of the Raman technique for the identification of key biochemical changes of leukemia cells under chemotherapeutic treatments.

In this chapter, I will describe the use of RS to analyze the biochemical features of the B-leukemia cell lines (RS4;11, REH and MN60) after low-dose and noncytotoxic treatments with methotrexate (MTX) and 6-mercaptopurine (6MP), the two key drugs used in current B-ALL maintenance therapy.

To identify specific RS peaks that correlate with the different stages of these B-leukemia cells, I defined the spectral changes after these B-ALL therapies in comparison with those seen under all-trans-retinoic acid (ATRA) treatment (used in the treatment of a different leukemia disease). Principal component analysis (PCA) was used to confirm the significance of these Raman spectral markers in the detection of minimal residual disease.

5.1 Immunophenotypic analysis of B-ALL regression after low-dose maintenance therapy

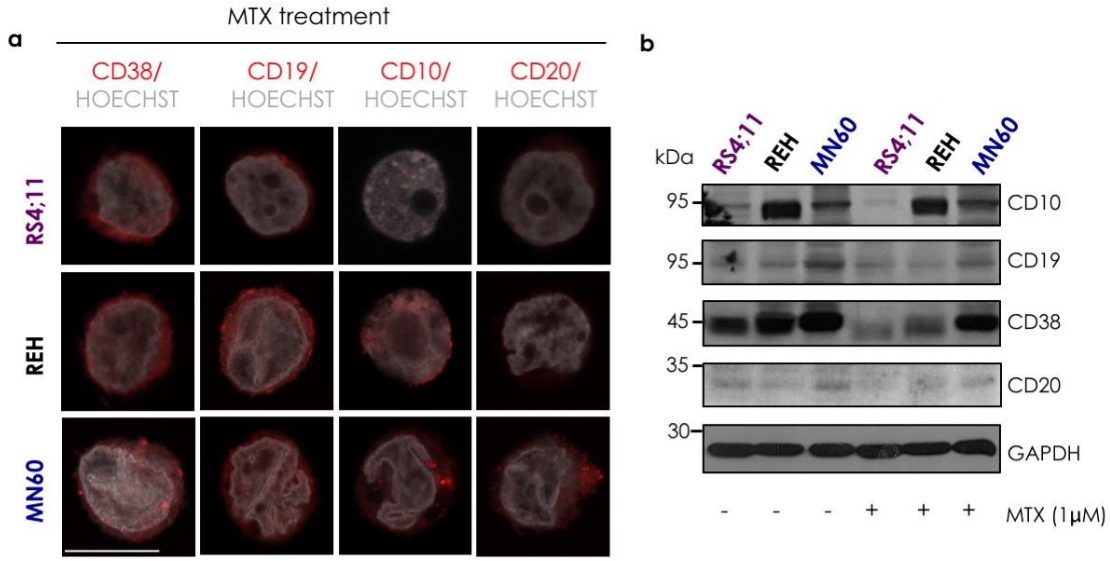

Figure 33: Acute lymphocytic leukemia regression through low-dose of MTX. *(a) Representative confocal microscopy images of RS4;11, REH and MN60 B-leukemia cells treated with 1 μM MTX for 72 h to mimic the clinical B-ALL maintenance therapy. Cells were fixed and processed for immunofluorescence analysis with anti-CD38, anti-CD19, anti-CD10 and anti-CD20 monoclonal antibodies (red) to monitor their expression levels. Gray, Hoechst-33258 nucleic-acid staining. Scale bar: 10 μm. (b) Representative immunoblotting of RS4;11, REH and MN60 B-leukemia cells treated as in a, with antibodies against CD10, CD19, CD20 and CD38 (as indicated). Glyceraldehyde 3-phosphate dehydrogenase (GAPDH) is shown for the internal protein levels and molecular weight standards (kDa) are indicated on the left of each panel. The blots have been run under the same experimental conditions.*

To provide a scenario as close as possible to the clinical setting, I analyzed the specific spectral variations of the cells under 'treatment' with two clinically demonstrated beneficial drugs that are used in maintenance chemotherapy of patients with B-ALL: MTX and 6MP. Low doses of MTX and 6MP that provide patients with peak plasma concentrations range from 0.01 μM to 1 μM [128] are used to induce specific B-ALL regression. MTX and 6MP are also specific treatments for patients with B-ALL, as they do not provide benefits for other leukemias, such as for regression of acute promyelocytic leukemia, where the maintenance therapy is primarily ATRA [128]. These three transformed B-leukemia cell lines were thus treated for 72 h with 1 μM MTX, 1 μM 6MP, or 1 μM ATRA (as the control) [41]. The cells were then analyzed by immunofluorescence microscopy and Western blotting to determine whether the B-ALL regression obtained in patients under similar conditions is associated with decreased

expression of particular B-leukemia antigens. This MTX treatment significantly reduced the plasma membrane staining of CD38 and CD19 in all of these B-leukemia cell lines, along with that of CD10 in the REH and MN60 cells, and of CD20 in the MN60 cells (Figure 33a versus non-treated control cells shown in Figure 26a). These immunofluorescence data were supported and confirmed by Western blotting (Figure 33b). Moreover, reduced intensity of nucleic-acid fluorescence staining was also observed in all three of these MTX-treated B-leukemia cell lines (Figure 33a versus non-treated control cells shown in Figure 26a).

Similar data for both antigen expression and nucleic acids (stained with Hoechst dye) were obtained with 6MP treatment (data not shown), while no effects were detected with ATRA treatment (Figure 34).

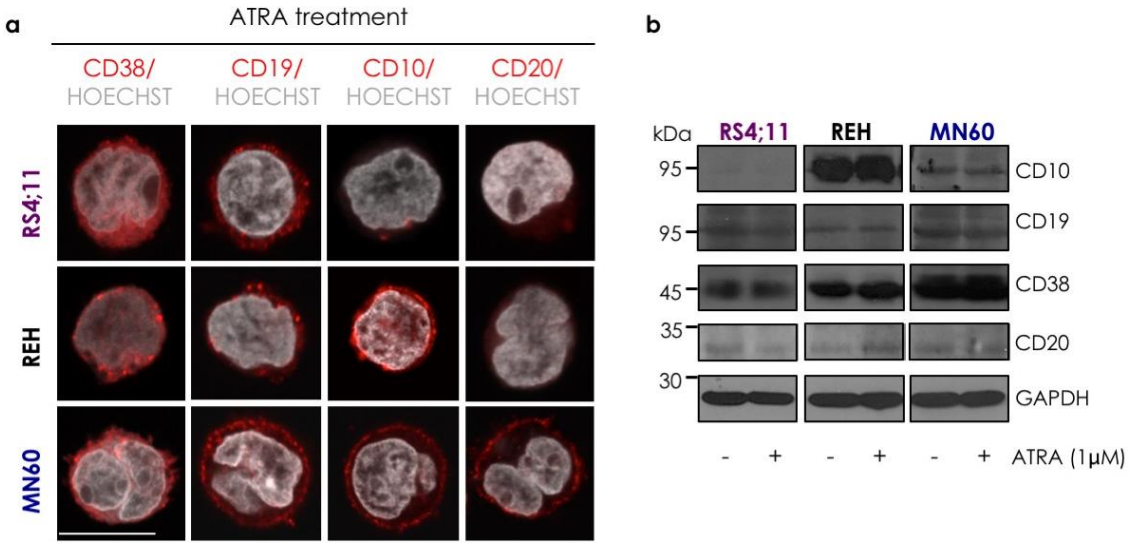

Figure 34: Effect of ATRA treatment on Acute lymphocytic leukemia cells. *(a) Representative confocal microscopy images of RS4;11, REH and MN60 B-leukemia cells treated with 1 μM ATRA for 72 h, and fixed and processed for immunofluorescence analysis with anti-CD38, anti-CD19, anti-CD10 and anti-CD20 monoclonal antibodies (red) to monitor their expression levels. Gray, Hoechst-33258 nucleic-acid staining. Scale bar: 10 μm. (b) Representative immunoblotting of RS4;11, REH and MN60 B-leukemia cells treated as in a, with antibodies against CD10, CD19, CD20 and CD38 (as indicated). Glyceraldehyde 3-phosphate dehydrogenase (GAPDH) is shown for the internal protein levels and molecular weight standards (kDa) are indicated on the left of each panel. The blots have been run under the same experimental conditions.*

Flow Cytometry analysis confirmed confocal microscopy study regarding the down-regulation of CD19, CD10 and CD38 differentiation antigens upon induction with MTX, while no effects were detected with ATRA treatment (Figure 35).

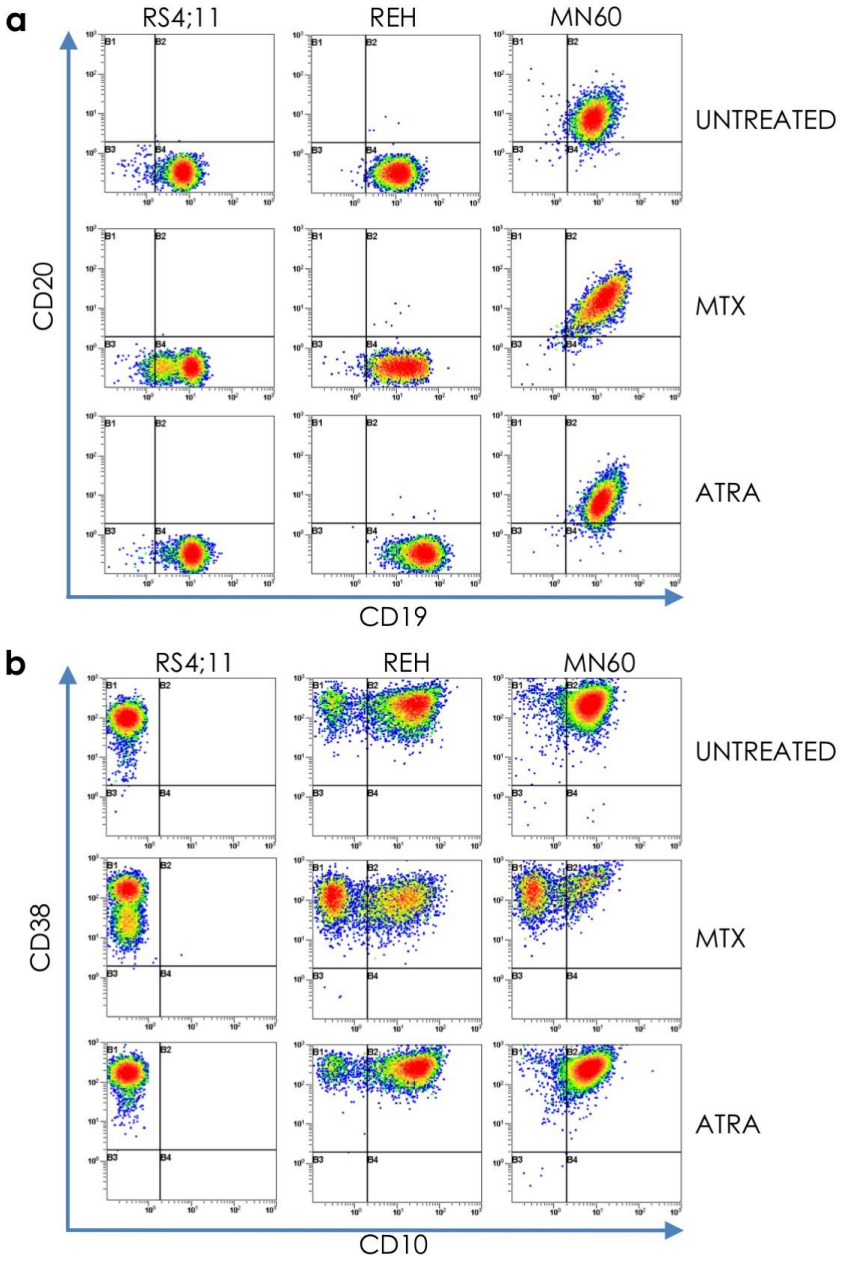

Figure 35: Flow cytometry analysis of RS4;11, REH and MN60 cell lines. *Panel A shows dot-plots analysis for the CD20 and CD19 surface expression on RS4;11, REH and MN60 cell lines in untreated conditions (Panel A, Upper Line), or treated for 72h with 1 µM of MTX (Panel A, middle line), or treated for 72h with 1 µM of ATRA (Panel A, bottom line). Panel B displays dot-plots analysis, for the CD38 and CD10 surface expression on RS4;11, REH and MN60 cell lines treated as in panel A.*

These preliminary analyses indicate that MTX treatment specifically reverted the B-cell differentiation process for these L2 (RS4;11 and REH cells) and L3 (MN60 cells) subtypes of B-leukemia cells (Figure 33), while as expected, the ATRA acute

promyelocytic leukemia treatment had no effect (Figure 34). Of note, under these conditions, no drug-mediated apoptotic effects were detected, as indicated by the nucleolus and chromatin staining with the Hoechst 33258 dye (Figure 33a, Figure 34a) [129].

5.2 Raman analysis of B-ALL regression after low-dose maintenance therapy

Figure 36 shows the comparison of the mean Raman spectra of these B-leukemia RS4;11, REH, and MN60 cells before and after the 1 μM MTX treatment, and the difference spectra obtained by subtraction of the MTX-treated spectra from the untreated cell spectra. The MTX-treated cells showed lower Raman intensities of the peaks related to nucleic acids, as can be seen at 785 cm^{-1}, 1120 cm^{-1}, 1370 cm^{-1}, and 1577 cm^{-1}. These reductions in the Raman bands suggest that the levels of nucleic acids are lower after the chemotherapy in these B-leukemia cells. Interestingly, the Raman spectra of the 6MP-treated B-leukemia cells showed similarly lower Raman intensities of the peaks related to nucleic acids as seen for the MTX-treated cells (Figure 37). As well as these peaks, the MTX-treated and 6MP-treated cells showed lower peak heights in the bands at 1004 cm^{-1} (CC ring breathing mode of phenylalanine) and 1447 cm^{-1} (CH2 deformation mode of proteins). The intensity of 1447 cm^{-1} Raman band is insensitive to the protein structure and depends only on the number of proteins, which indicated that these MTX and 6MP treatments induced specific reductions in the cell protein content [129]. Conversely, the ATRA-treated cells did not show reduced expression of CD10, CD19, CD20, and CD38 at the plasma membrane and nucleic-acid fluorescence staining intensity (Figure 34), and in turn, did not show significant modifications in the Raman spectral region related to protein-DNA ratio (around 1447 and 785 cm^{-1}; Figure 38). In general, the difference spectra between the ATRA-treated and nontreated B-leukemia cells show only slight spectral variations.

These specific spectral modifications should be explained by the mechanisms of action of the chemotherapeutic drugs used in this study. The reduced nucleic acid content can be explained by the inhibition of the enzyme dihydrofolate reductase through MTX-derived metabolites [130]. The dihydrofolate reductase inhibition arrests the synthesis of both purines and thymidine, which alters DNA replication and RNA synthesis, and thus, in turn, the nucleic acid cell content. Similarly, the mechanism of action of 6MP consists of inhibition of the de-novo pathway for purine ribonucleotide synthesis [131] that is required for DNA repair, methylation, and mitotic duplication. On the other hand, the

reduced protein content can be explained by the decreased expression of plasma membrane antigens (e.g., CD10, CD19, CD20, CD38) and cytoplasmic immunoglobulins. Interestingly, both MTX and 6MP treatments similarly affected the Raman spectra of these three B-leukemia cells, with reduced intensities of peaks related to DNA, RNA and protein content. To demonstrate the specific ability of this RS approach for the detection of the anti-leukemic effects of MTX and 6MP treatments on these B-leukemia cells we used ATRA treatment as a control. The Raman spectra of the ATRA-treated and nontreated B-leukemia cells did not show any significant differences. Indeed, the relative variations in the Raman band intensities were much smaller than those observed between normal B-lymphocytes and the B-leukemia cells, or between MTX-treated or 6MP-treated and nontreated B-leukemia cells.

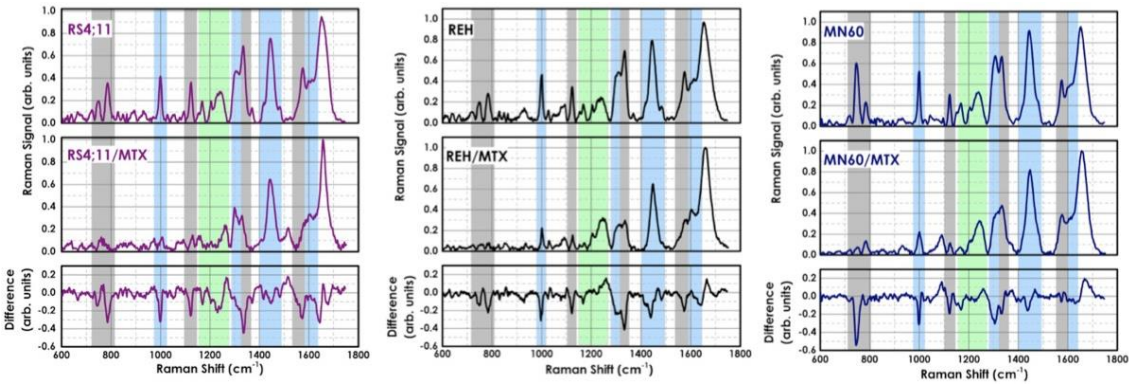

Figure 36: Acute lymphocytic leukemia regression through low-dose of MTX. *Raman spectra of three B-leukemia cell lines recorded without and with MTX treatment as in a. The difference spectra were obtained by subtracting the untreated from the treated spectra (bottom panels).*

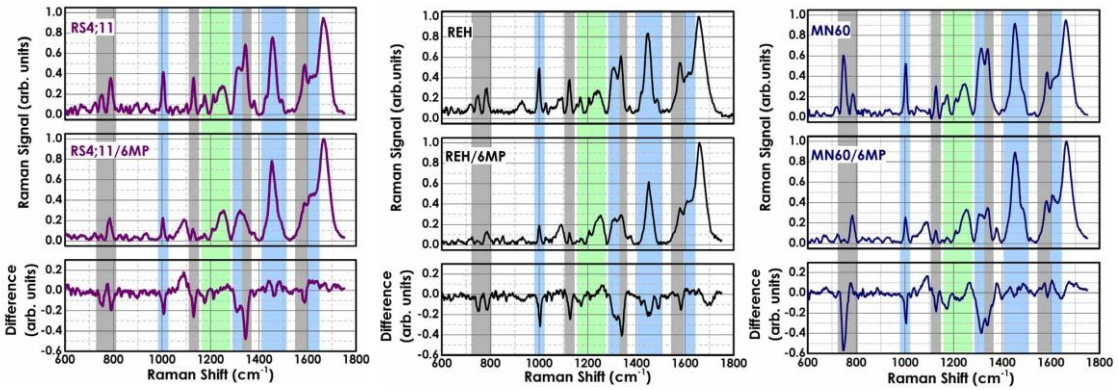

Figure 37: Acute lymphocytic leukemia regression through low-dose of 6MP. *Raman spectra of the three B-leukemia cell lines recorded without and with 1 μM 6MP for 72 h. The difference spectra obtained by subtracting the B-leukemia cell spectra from the 6MP-treated B-leukemia cell spectra are also shown (bottom panels).*

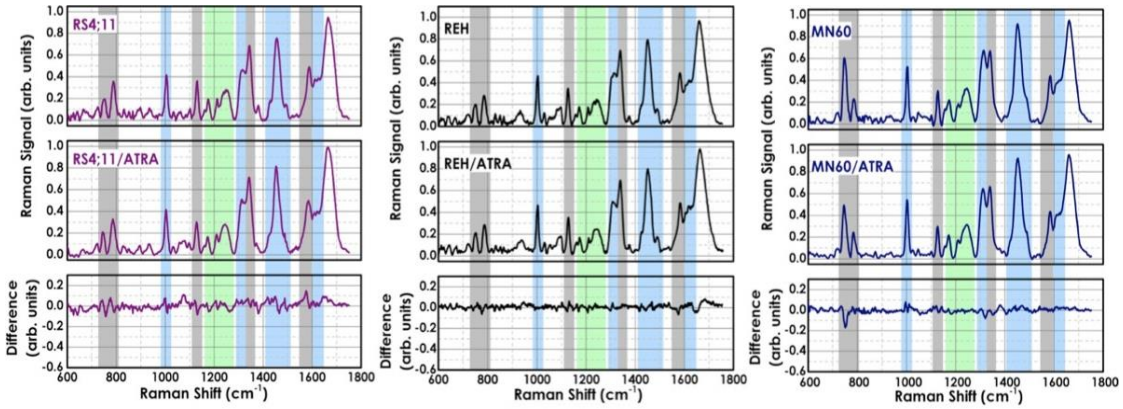

Figure 38: Effect of ATRA treatment on Acute lymphocytic leukemia cells. *Raman spectra of three B-leukemia cell lines recorded without and with ATRA treatment as in a. The difference spectra were obtained by subtracting the untreated from the treated spectra (bottom panels).*

To further highlight the ability of RS to specific follow the drug-induced biochemical changes in leukaemia cells, I additionally analysed the spectral changes of the considered cell lines (RS4;11, REH and MN60 cells after low-dose and noncytotoxic treatments with methotrexate (MTX) at three different concentrations (0.01 µM, 0.1 µM and 1 µM).

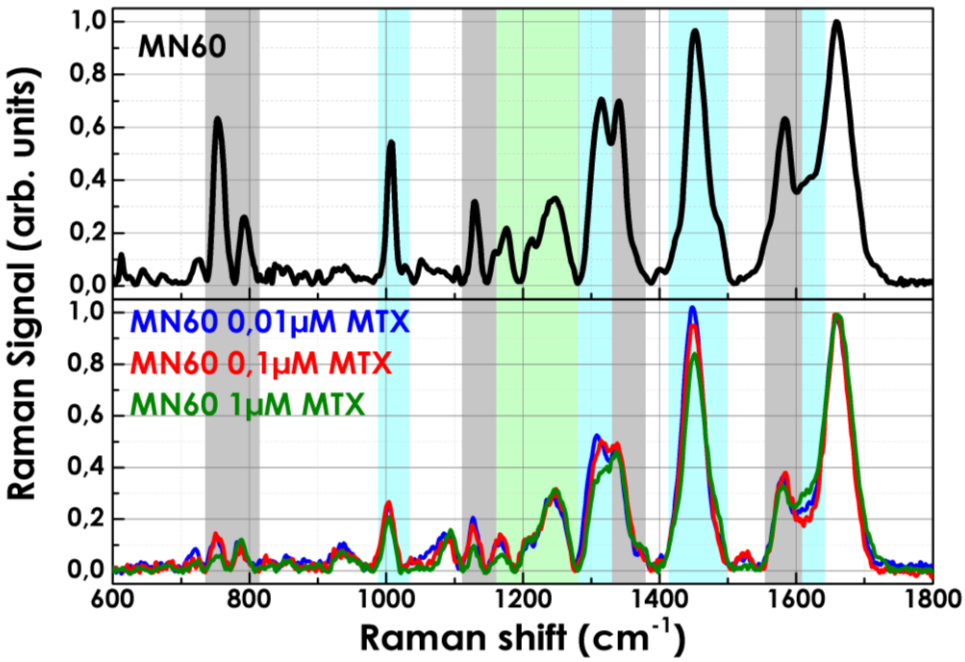

Figure 39: *Effect of MTX-treatment at concentration of 0.01, 0.1 and 1 µm on MN60 cells.*

Figure 39 shows the mean Raman spectrum of MN60 cells before MTX treatment and the Raman spectra of MN60 after the MTX treatment at three different concentrations. The MTX-treated cells showed a gradual decrease of intensities of Raman peaks related to nucleic acids (785 cm^{-1}, 1120 cm^{-1}, 1370 cm^{-1}, and 1577 cm^{-1}) and, similarly, a progressive decrease of Raman bands related to proteins (1004 cm^{-1}, 1300-1350 cm^{-1}, 1400-1500 cm^{-1}); these reductions in the Raman bands are proportional to the increase of MTX concentrations, from 0.01 μM to 1 μM.

These findings confirm that very specific Raman markers can be used to discriminate normal from both leukemia cells and leukemia cells under maintenance treatment, which suggests that RS can be used in the detection of minimal residual disease.

5.3 PCA analysis of B-ALL regression

Finally here, I used PCA to evaluate the discrimination between the drug-treated versus the normal B cells according to the RS. Figure 40a shows the PCA scatter plots of the scores of PC1-3 of 300 of each of the control B cells and MTX-treated B-leukemia RS4;11, REH and MN60 cells. The control B cells can be easily distinguished from the MTX-treated B-leukemia cells by this PCA, as shown by the distinct group of the B lymphocytes. The data reported in the confusion matrix (Figure 40b) indicate that 1172 out of 1200 of these cells were correctly classified, which gives an efficiency of 98.8%. Similar data were obtained with the 6MP-treated leukemia cells. On the other hand, by comparing the Raman spectra of the B-leukemia cells to those of the ATRA-treated B-leukemia cells using PCA, there was large overlap according to the PC1 versus PC2 plots, and thus little, if any, effects of ATRA on these PCs (Figure 41).

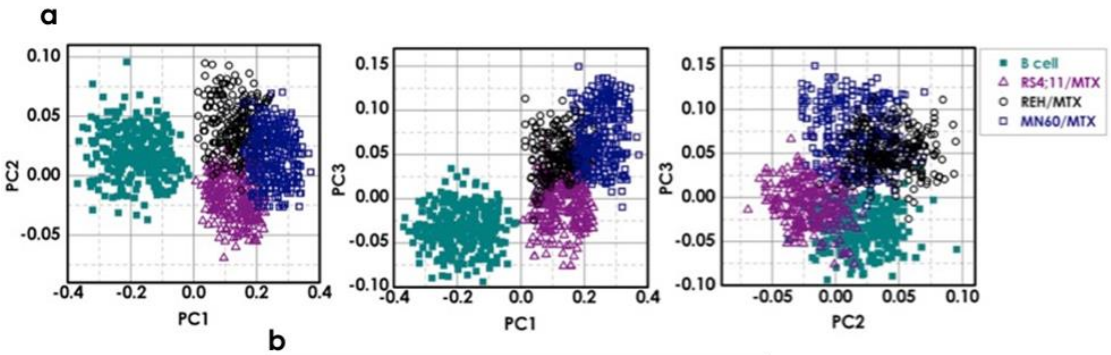

b

	B cells	RS4;11 /MTX	REH/ MTX	MN60 /MTX
B cells	300	0	0	0
RS4;11/MTX	0	290	7	3
REH/MTX	0	6	289	5
MN60/MTX	0	2	5	293

Figure 40: Acute lymphocytic leukemia regression through low-dose of MTX. *(a) PCA scatter plots comparing the untreated and MTX-treated B-leukemia cells. (b) Confusion matrix for the classification of the untreated and MTX-treated B-leukemia cells.*

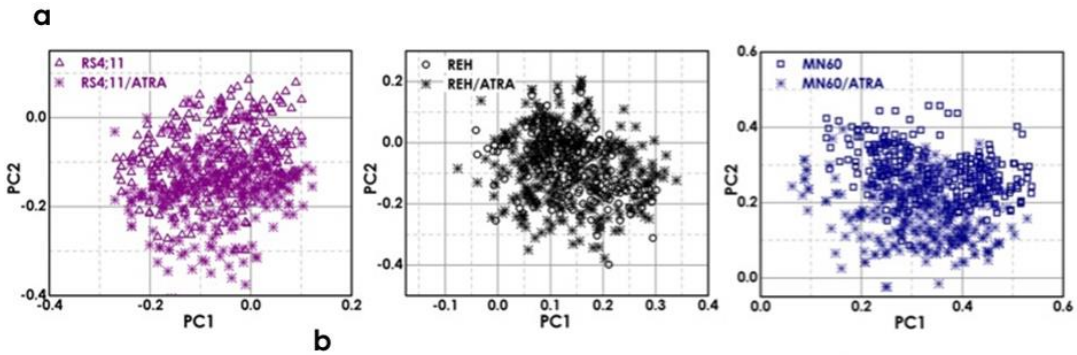

b

	B cells	RS4;11 /ATRA	REH/A TRA	MN60 /ATRA
B cells	297	2	1	0
RS4;11	4	280	16	0
REH	1	12	287	0
MN60	0	0	0	300

Figure 41: Effect of ATRA treatment on Acute lymphocytic leukemia cells. *(a) PCA scatter plots comparing the untreated and ATRA-treated B-leukemia cells. (b) Confusion matrix for the classification of the untreated and ATRA-treated B-leukemia cells.*

5.4 Discussion and conclusions

Using independent and complementary approaches, as immunofluorescence, Western blotting and RS, I identified some biological features that were modified under these B-

ALL specific maintenance therapies. Of note, low-dose treatments were used here to better analyze the accuracy of our approaches for the detection of these specific biochemical changes. In more detail, under both MTX and 6MP treatments, all three of these B-leukemia cell lines showed B-leukemia regression through the reversing of the B-cell differentiation/maturation process, which was identified and classified according to the specific antigen expression profiles, and promoted changes in the nucleic acid contents without any apoptotic effects. These specific modifications should be explained by the mechanisms of action of the chemotherapeutic drugs used in this study.

Interestingly, both MTX and 6MP treatments similarly affected the Raman spectra of these three B-leukemia cells, with reduced intensities of peaks related to DNA, RNA and protein content. To demonstrate the specific ability of this RS approach for the detection of the anti-leukemic effects of MTX and 6MP treatments on these B-leukemia cells we used ATRA treatment as a control. The Raman spectra of the ATRA-treated and nontreated B-leukemia cells did not show any significant differences. Indeed, the relative variations in the Raman band intensities were much smaller than those observed between normal B-lymphocytes and the B-leukemia cells, or between MTX-treated or 6MP-treated and nontreated B-leukemia cells. Additionally, the PCA scatter plots and the cross-validation data demonstrate that although the MTX-treated (or 6MP-treated) B-leukemia cells showed reduced expression of plasma membrane antigens and DNA, their spectra can be separated from the normal B-lymphocytes with an efficiency of about 99%.

6

Proof of principle with B-ALL clinical samples

In this chapter, I will illustrate the application of RS approach to discriminate between normal B-lymphocytes and B-lymphocyte-enriched fractions from patients with B-ALL, Preliminary results from clinical samples indicate high consistency of, and potential applications for, this Raman spectroscopy approach.

6.1 B-ALL clinical samples

I extended the present study to clinical samples, with the analysis of the Raman spectra of B-cell–enriched lymphocyte fractions purified from peripheral blood of three patients with B-ALL. I preliminary analyzed these leukemic clinical cell samples using standard multi-parametric flow cytometry to characterize them based on the immunophenotypic classification (Figure 42). These leukemic cells from patients 1 (Pt-1) and 2 (Pt-2) showed very similar immunological features, including: plasma-membrane expression of CD19, CD10, CD38, and CD45 (intermediate expression level), and of HLA-DR antigens, with low surface expression of CD34 and no surface expression of CD20, and of immunoglobulins (SmIg) (Figure 42). According to this antigenic profile, these leukemia cells of Pt-1 and Pt-2 can both be classified as ‘common B-ALL’ and thus they should have similar Raman spectra to the REH B-leukemia transformed cell line.

Conversely, for the Pt-3–derived cells, in addition to positivity for CD19, CD10, CD38, CD45, and HLA-DR, there was also plasma-membrane expression of CD20, which indicated that their B-ALL was of a more differentiated type than for the Pt-1 and Pt-2 cells (Figure 42). However, these Pt-3–derived cells did not express surface or cytoplasm immunoglobulins (Figure 42), which indicated that they might have originated from B-cell differentiation/ maturation blocked at an intermediate process between the pro-B and the pre-B maturation stages. Thus, according to this immunological feature, the leukemic cells from Pt-3 should have a Raman spectrum with a profile in-between that of the B-leukemia REH and MN60 transformed cell lines.

	Pt-1	Pt-2	Pt-3
CD19	+	+	+
CD10	+	+	+
CD20	-	-	+
CD34	low	low	-
CD38	+	+	+
HLA-DR	+	+	+
CD45	dim	dim	+
SmIg	-	-	-

Figure 42: Immunophenotypes of the B-ALL cells from patients. *The Pt-1 and Pt-2 B-ALL cells show a 'common' B-ALL immunoprofile due to the surface expression of CD19, CD10, CD38, CD45 (intermediate expression level, dim) and HLA-DR, with low surface expression of CD34 (low) and absence of CD20, and surface Immunoglobulins (SmIg). The Pt-3 B-ALL cells were more differentiated than those from Pt-1 and Pt-2, due to the surface membrane presence of CD20 with CD19, CD10, CD38 and HLA-DR, as well as bright intensity of expression for CD45.*

6.2 Raman diagnosis of B-ALL clinical samples

Figure 43a shows the Raman spectra of normal B cells, the B-leukemia REH cells, and those acquired from the three cell samples from the patients with B-ALL. The mean Raman spectra of Pt-1 and Pt-2 cells appear to be similar to each other and similar to the Raman spectrum of the REH cells. Conversely, as illustrated in Figure 43b, there were distinct differences between the Raman spectrum of normal B cells and those of the three patient B-ALL cell samples. The peaks most exclusively related to the ring breathing modes in DNA bases (i.e., 785, 1120, 1370, 1577 cm^{-1}) were significantly reduced in intensity in the Raman spectra of Pt-1 and Pt-2, while the CH2 deformation mode at 1447 cm^{-1} was significantly stronger (Figure 43b). These differences were more

pronounced in the Pt-3 Raman spectrum, as this B-ALL cell sample was more differentiated from the previous two.

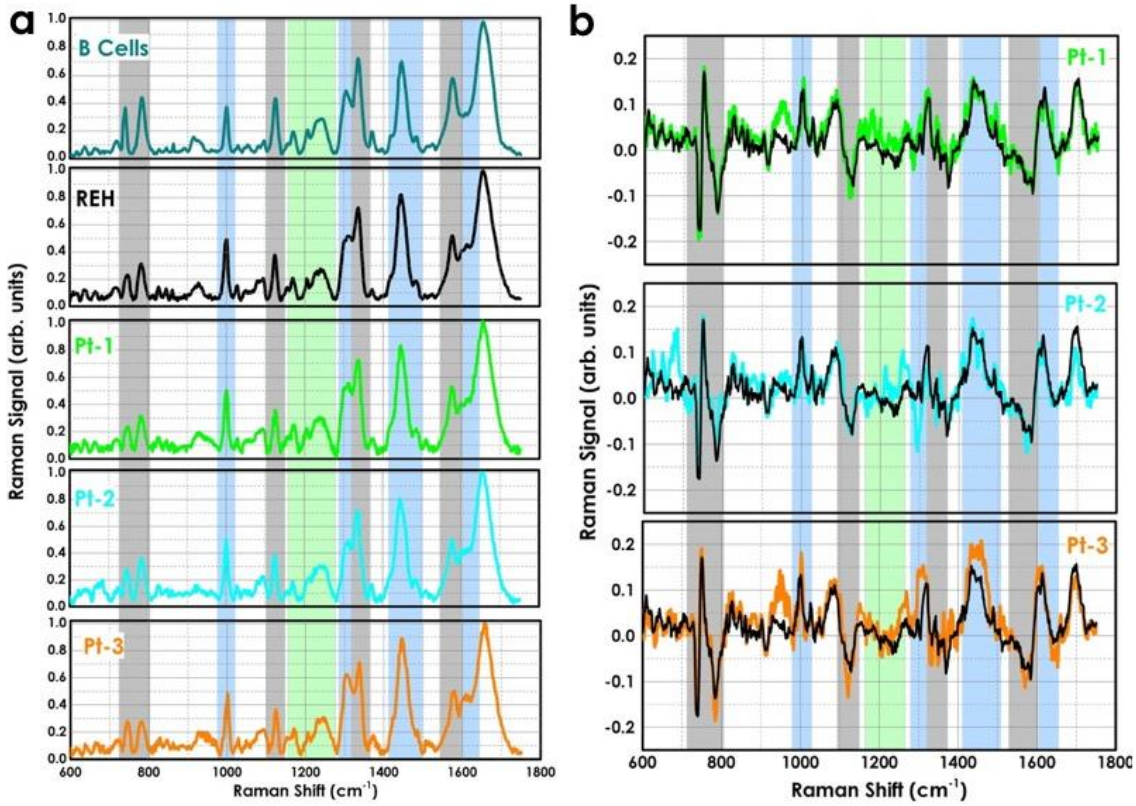

Figure 43: Proof of principle with clinical samples. *(a) Mean Raman spectra from 300 acquisitions of normal B lymphocytes, REH B-leukemia cells, and the three clinical B-ALL cell samples. (b) Difference spectra obtained by subtracting the normal B lymphocyte Raman spectrum from the clinical B-ALL samples and the REH B-leukemia cell spectra (black line).*

6.3 Statistical analysis of B-ALL clinical Raman data

To clarify the biochemical classification and spectral variations for the B-leukemia cells, I used an empirical analysis based on the intensity ratio of two prominent Raman bands, at 1447 cm^{-1} and 785 cm^{-1} (I_{1447}/I_{785}). Figure 44 shows the plot of the I_{1447}/I_{785} ratios according to the cell types. The mean (± s.d.) of the ratio for the normal B cells (RBcell = 1.6 ±0.3) was significantly different from the means of the B-leukemia cells ($R_{RS4;11}$ = 1.98 ± 0.17; R_{REH} = 2.59 ± 0.18; R_{MN60} = 3.45 ± 0.20) and the patient-derived B-ALL cells (R_{Pt-1} = 2.56 ± 0.27; R_{Pt-2} = 2.45 ± 0.25; R_{Pt-3} = 2.93 ± 0.27). These differences reflected the relative changes in the potential biological markers from cell surface antigens, cytoplasmic proteins, and DNA content [129]. Additionally, the spectral variability measured in the clinical samples was much higher compared to the B-leukemia cell lines. The overall spectral intensities varied by 20% about the mean for

normal B cells, by 7% to 8% for the three B-leukemia cell lines, and by 10% to 12% for the clinical samples. The nonparametric intensity ratio provided a diagnostic sensitivity of 98.7% and specificity of 95.7% for separating the normal B cells and B-leukemia REH cells (P <0.00001).

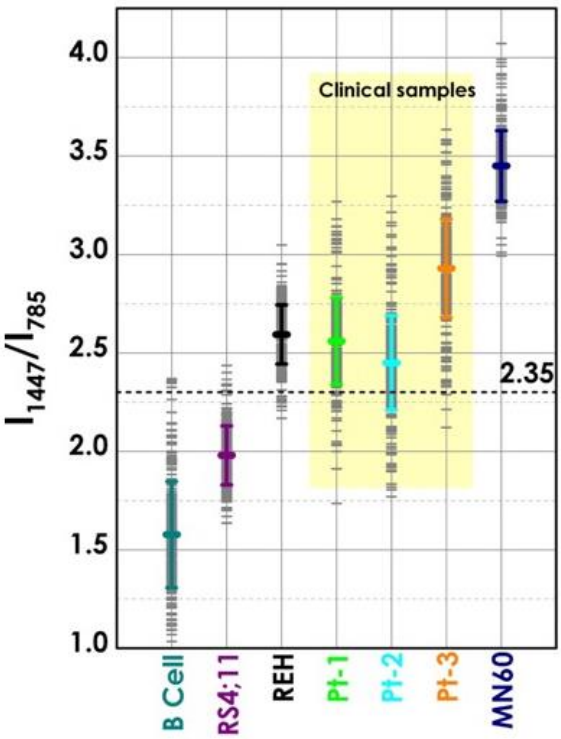

Figure 44: Empirical analysis of clinical samples. *Plot of the intensity ratios of the Raman signals at 1447 cm^{-1} and 785 cm^{-1} (I_{1447}/I_{785}), as indicated.*

With the clinical samples, the measured diagnostic sensitivity and specificity for the intensity ratios and relative to the normal B cells were 79% and 81% for patient 1, 80% and 83% for patient 2, and 87% and 85% for patient 3, respectively.

Table 6: *Diagnostic sensitivity and specificity for clinical samples*

Diagnostic sensitivity and specificity			
	Pt-1 (%)	Pt-2 (%)	Pt-3 (%)
Sensitivity	79	80	87
Specificity	81	83	85

I also used PCA for classification of these clinical samples. These data for the normal B cells, the REH B-leukemia cells, and the three patient samples are shown in the scatter

plots of Figure 45. The PCA algorithm achieved identification of each pathological clinical sample with sensitivities of 88%, 89% and 94% for Pt-1, Pt-2 and Pt-3, respectively, and specificities of 85%, 88% and 90%, again for Pt-1, Pt-2 and Pt-3, respectively, which provides 5% to 10% improvements compared with the empirical methods using the intensity ratios. Therefore, although the spectral variability in the clinical samples is more pronounced compared to the B-leukemia cell lines, analysis of the Raman spectra allows the discrimination of the B-ALL clinical cell samples of these patients from the normal B cells with high sensitivity and specificity.

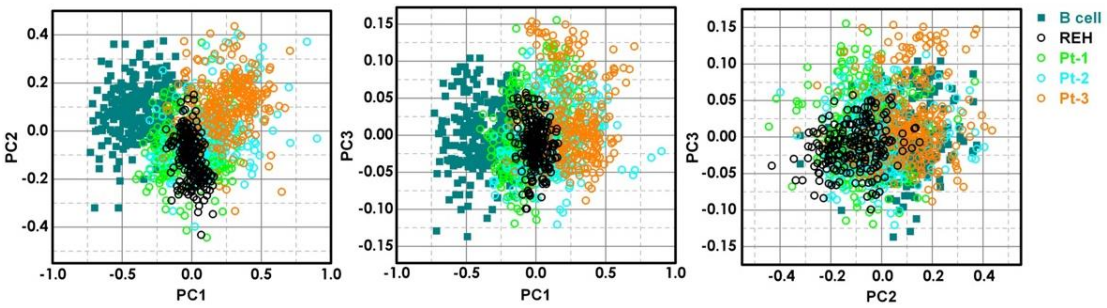

Figure 45: PCA analysis. *PCA scatter plots comparing normal B lymphocytes, REH B-leukemia cells, and the three clinical B-ALL cell samples.*

6.4 Discussion and conclusions

Finally, I extended the Raman approach to three clinical patient samples. Pt-1 and Pt-2 had the preliminary classification of 'common B-ALL', and Pt-3 had B-ALL derived from malignant transformation of a B-cell progenitor that was intermediate between the pro-B and pre-B maturation stages. The distinctive differences in the Raman spectra between the normal and the clinical samples confirmed and further reinforced these observations.

To develop simple but effective algorithms for differentiating B-leukemia cells from normal B-lymphocytes, the nonparametric empirical approach that uses peak intensity ratio measurements of specific Raman bands has been widely applied to evaluate malignant changes in several studies [132][133]. Here, I showed that the nonparametric intensity ratios of the two prominent Raman bands at 1447 cm^{-1} (CH2 mode proteins) and 785 cm^{-1} (ring breathing modes in DNA bases), I1447/I785, provided good diagnostic sensitivity (79%-87%) and specificity (81%-85%). The significant differences in the intensity ratios between the normal B-lymphocytes and the clinical patient B-ALL samples might reflect the relative changes in the concentrations of potential biological markers, as cell surface antigens, and cytoplasmic protein and DNA contents.

Additionally, despite the higher variability in the clinical patient B-ALL samples compared to the three B-leukemia cell lines, this Raman approach allowed significant discrimination between normal B-lymphocytes versus these B-ALL cells.

This relatively simplistic empirical analysis only used a limited number of Raman peaks, and most of the information contained in the Raman spectra is not included. Therefore, I also performed PCA with these clinical samples. In more detail, the PCA algorithm achieved identification of each pathological clinical sample with a sensitivity from 88% to 94% and a specificity from 85% to 90%. These sensitivity and specificity data in this diagnosis provided by RS can now set the stage for more specific clinical studies. Further studies with both clinical samples before and after chemotherapy treatment will still be needed to understand the potential limitations of this RS approach.

7

Classification of white blood cells

In this chapter, I will show the feasibility of using RS and multivariate statistical approaches (PCA) to identify and discriminate leukocytes. We focused on five populations isolated from peripheral blood of several human volunteers via conventional flow cytometry: granulocytes (neutrophils), monocytes, T cells, B cells and NK cells.

7.1 Introduction

The direct identification of cells forms the basis of many analytical laboratory tests including those used in haematology and oncology diagnostics. One of the most important examples is the complete blood count (CBC), which is the most widely used clinical test ordered for almost every disease.

Blood is an important body fluid, which contains three major corpuscular elements: red blood cells (or erythrocyte), white blood cells (or leukocytes) and platelets (or thrombocytes). White blood cells (WBCs), also called leukocytes, are the cells of the immune system that are involved in protecting the body against infectious disease and foreign invaders. All white blood cells are nucleated, which distinguishes them from the anucleated red blood cells and platelets and can be divided into the three main types:

granulocytes, lymphocytes, and monocytes. These types are distinguished by their physical and functional characteristics. Monocytes and granulocytes belong to myeloid lineage whereas lymphocytes belong to lymphoid lineage. Granulocytes can be classified as neutrophils, eosinophils and basophils by their nucleus shape and by the presence of granules in the cytoplasm; lymphocytes include T cells, B cells, and natural killer (NK) cells.

Most existing cell counting methods are based on optical detection techniques due to their minimal invasiveness, high registration speed, high spatial resolution, and ability to detect many physical parameters including scattering, polarization, absorption, and fluorescence.

However, the most commonly used flow cytometers and automated cell counters are sizable, complex, and usually expensive. Moreover, such devices require the use of chemical reagents. The sample preparation process may be complicated and may need to be performed by professional medical personnel.

In this work, I will show the capability of RS in the identification and classification of white blood cells.

7.2 Raman identification of leukocytes

I studied three different types of leukocytes (granulocytes, monocytes and lymphocytes) by Raman spectroscopy. I considered only the polymorphonuclear neutrophils as they form almost the 95% of the granulocyte population (basophils are <1% of the granulocyte population and eosinophils <5% of the granulocyte population). For the lymphocytes cells I preliminary considered only B and T cells as they form the major cellular components of the adaptive immune response.

Table 7: *Main morphological characteristics of the leukocytes.*

Leucocytes	Nuclear shape	Cytoplasm	Dimension (µm)
Monocytes	Lobulated/indented	Occasionally vacuoles and granules	15-30
Lymphocytes (T and B cells)	Large and regular	Small amount	7-8
Granulocytes (neutrophils)	Multilobulated	Presence of fine numerous granules	10-15

The three classes of studied leukocytes can be microscopically discriminate due to their specific shapes of nuclei, sizes and cellular components (Table 7). Granulocytes have a diameter of about 10-15 µm, a multilobulated nucleus and cytoplasmic granules.

Monocytes are large cells 15-30 µm presenting a lobulated nucleus. Lymphocytes are the smaller leukocytes having a typical size of about 7-8 µm and single large nucleus. The three cell populations can be easily separated and identified by measuring the side (SSC) and forward (FSC) scatter of the cells by flow cytometry as shown in Figure 46. More precisely, the FSC provides a rough measure of the cells size, while the SSC is a measure of the complexity of the cell internal structures. The more "granular" a cell is the higher its SSC will be, as confirmed form the results of Figure 46. However, different flow cytometers will provide slightly different FCS and SSC measurements, depending on refractive index mismatches between sheath and sample, beam geometry and polarization, beam stop position and collecting angles. Therefore, the specific labelling of the cell is required to improve the statistic.

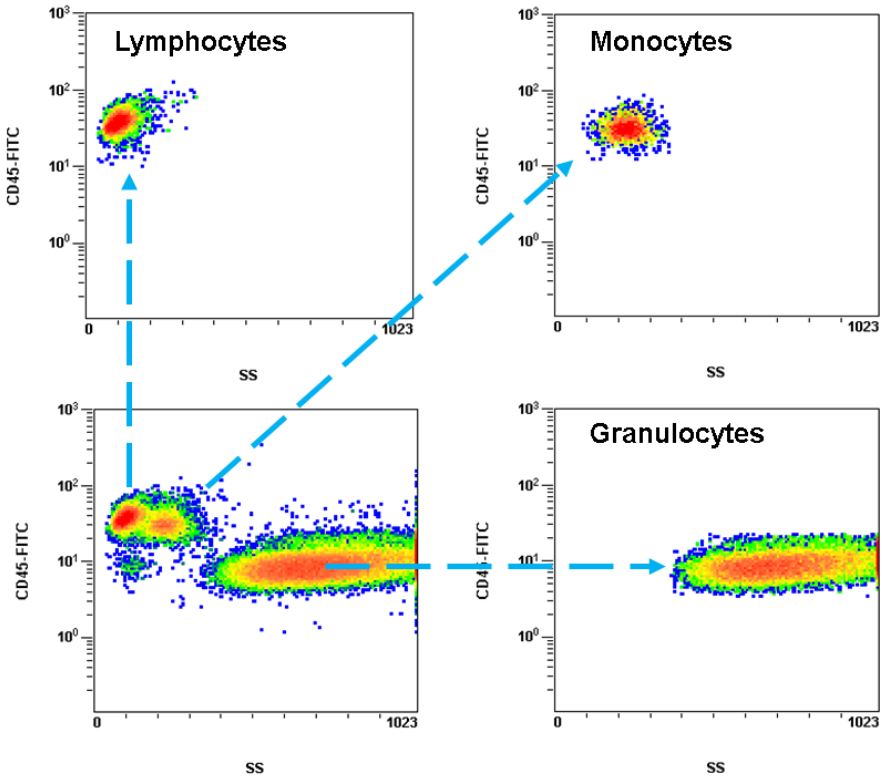

Figure 46: *Differentiation of leukocytes by detection of the CD45-FSC and SSC parameters.*

In our experiments, leucocytes have been isolated from peripheral blood of healthy donors with informant consent according to the Ethics Committee of SDN (See Chapter 3 for more details).

The isolated cells were analysed for purity by flow cytometry. More precisely, CD45+ granulocytes were obtained at a purity level 95% (Figure 47); CD14+ monocytes were obtained at a purity level of 90% (Figure 48); CD3+, CD19+ lymphocytes were obtained

at a purity level of 95%. The fluorescence intensities were measured with a flow cytometer (FC-500; Beckman-Coulter, Milan, Italy), according to the manufacturer instructions. The percentage of granulocytes (CD45+, pan-leucocyte marker) was assessed before and after the Ficoll-Histopaque procedure. Instead, the percentages of lymphocytes and monocytes (CD14+/ CD56+; CD14+/ CD19+) were assessed after the immunomagnetic separation procedure.

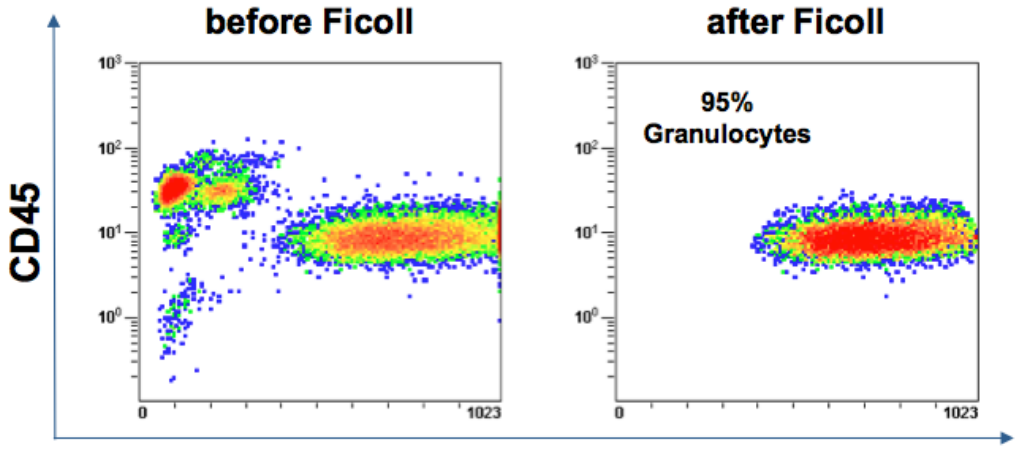

Figure 47: Dot plots for the determination of human granulocytes purification by flow cytometry. *Percentage of granulocytes (CD45+) determined by flow cytometry before and after Ficoll procedure.*

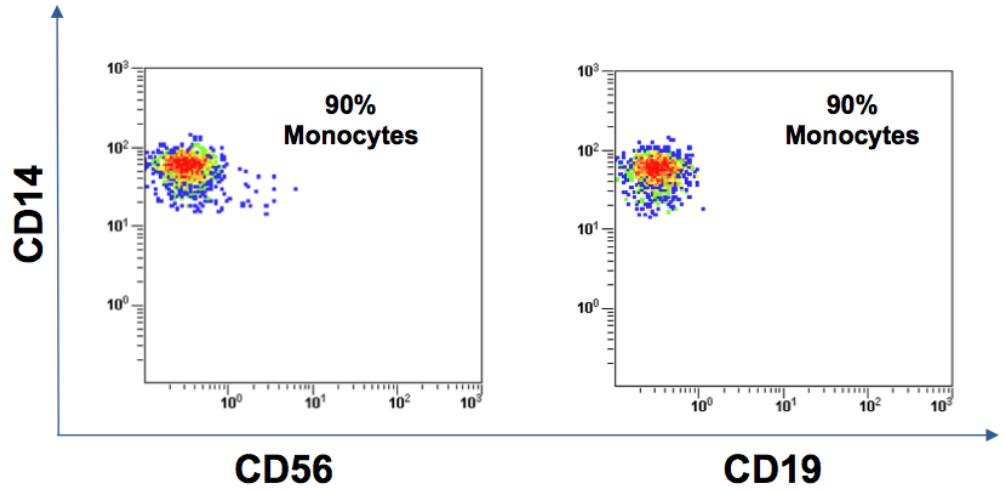

Figure 48: Dot plots for the determination of human monocytes purification by flow cytometry. *Percentage of monocytes (CD14+/CD56+; CD14+/CD19+) determined by flow cytometry, as pre-separation and post-separation through negative immunomagnetic selection.*

For the Raman measurements $1x10^6$ cells were suspended in 1ml of culture medium, a drop of the solution was placed on a quartz slide and the 15 spectra were acquired within 15-20 min of removal from the culture medium. For each cell type, the cells analyzed

were derived from three different donors, to ensure that the observed differences were the result of biological variations rather than variations from donor to donor.

To determine the RS markers that specifically identify differences in the biochemical compositions between the three types of leucocytes, a total of 100 Raman spectra from lymphocytes, monocytes and granulocytes have been acquired and analysed. The mean Raman spectra collected for each population are shown in Figure 49.

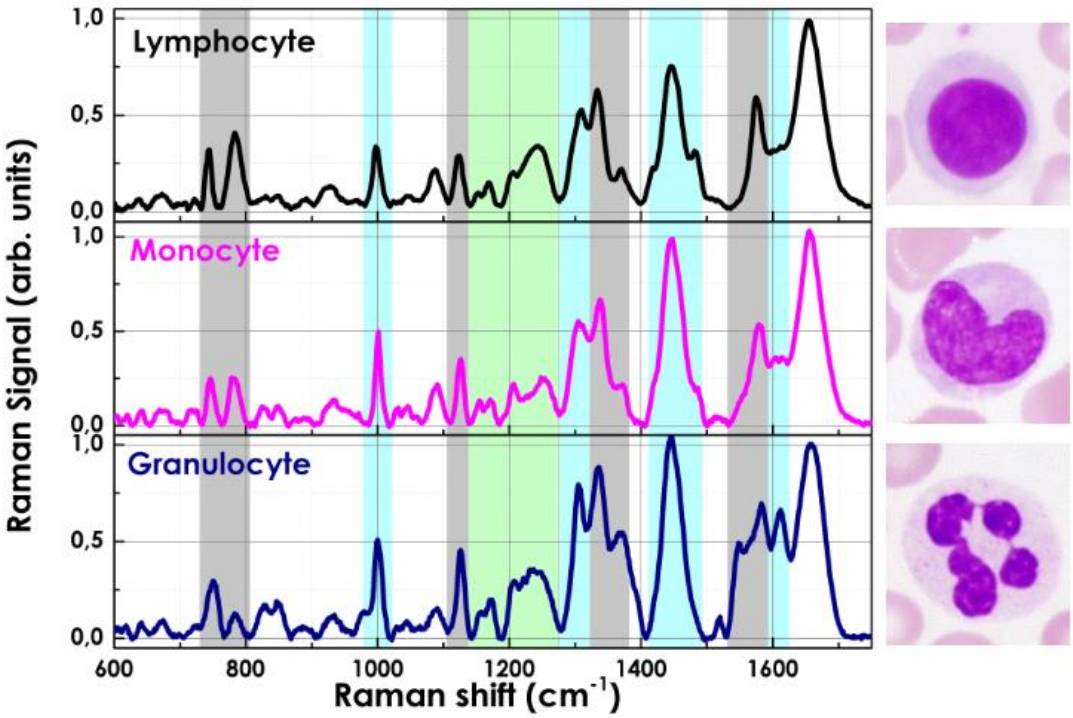

Figure 49: Spectral identification of leucocytes. *The mean Raman spectra of lymphocytes, monocytes and granulocytes are shown. Representative images of the cell morphology using May Grunwald-Giemsa histochemical staining for DNA and RNA molecules are additionally presented.*

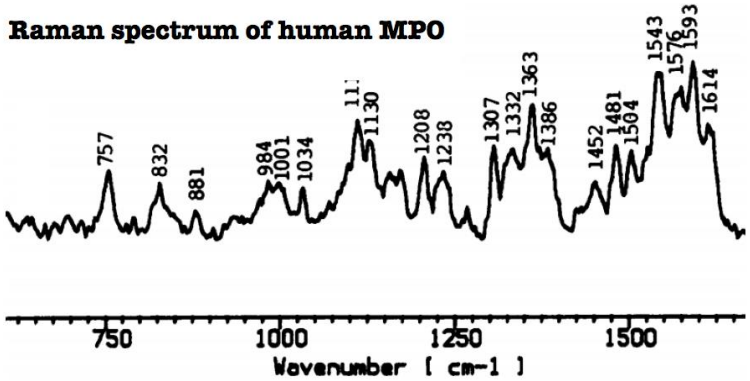

Figure 50: *Raman spectrum of isolated oxidized human myeloperoxidase.*

At first glance, lymphocytes and monocytes Raman spectra show very similar spectral profile. As those spectra are acquired by focusing the laser probe on the cell nucleus nucleic acid contributions are clearly visible, such as ring breathing modes of the nucleic acid bases (730-750 cm^{-1} adenine, thymine ring breathing and at 1576 cm^{-1} guanine and adenine contributions) and from the O−P−O backbone (785 cm^{-1} and 1095 cm^{-1}). However, due to large probed volume, the Raman system should also partially examine the membrane and cytoplasm above and below the nucleus. Indeed, typical vibrational contributions due to proteins such as the amide I band (around 1660 cm^{-1}), the amide II band (around 1257 cm^{-1}) and C-H bond (around 1445 cm^{-1}) are clearly visible. The intense vibrational band around 1341 cm−1 has contributions from proteins and nucleic acids and to a minor extent also from carbohydrates. One of the major differences between monocytes and lymphocytes are the relative intensities of the nucleic acid and protein vibrational bands. This can be explained by a much larger nucleus in the lymphocytes, which almost fills the whole cell compared to a smaller indented nucleus in the monocytes.

The granulocyte Raman spectrum presents some substantial spectral differences in the regions around 750-800 cm^{-1} and around 830, 980, 1350, 1540 cm^{-1} [129]. Indeed, strong signal contributions from myeloperoxidase (MPO), a peroxidase enzyme of the azurophilic granules, are present as is clear from the spectrum of the purified enzyme shown in Figure 50. Neutrophil granulocytes present a lot of cytoplasmic granules of 0.2 μm in diameter (11), which contain a wide variety of oxidative metabolites and digestive enzymes, just as the MPO. MPO contains two covalently bound active site heme groups (47, 48) and therefore its contribution is resonantly enhanced at the excitation wavelength used in this work [134]. Their main functions are phagocytosis, killing, and digestion of bacteria and other microorganisms.

7.3 Leukocyte statistical analysis

To clarify the biochemical classification and spectral variations for monocytes, lymphocytes and granulocytes, I used an empirical analysis based on the intensity ratio of two prominent Raman bands, at 1447 cm^{-1} and 785 cm^{-1} (I_{1447}/I_{785}). Figure 51 shows the plot of the I_{1447}/I_{785} ratios according to the cell types. The mean (± s.d.) of the ratio for the leucocytes ($R_{leucocytes}$ = 1.8 ± 0.3) was significantly different from the means of the monocytes ($R_{monocytes}$= 5.2 ± 0.4) and granulocytes ($R_{granulocytes}$= 8.2 ± 0.6). These differences reflected the relative changes in the potential biological markers from cytoplasmic proteins and DNA content.

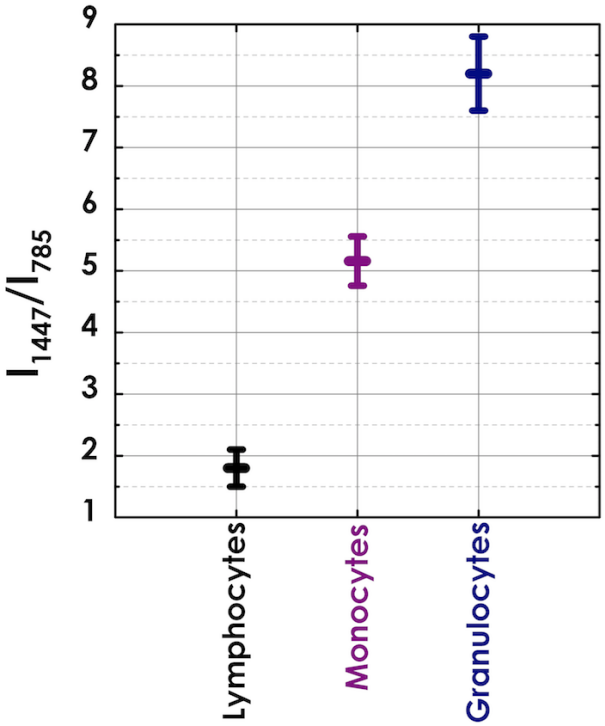

Figure 51: *Plot of the intensity ratios of the Raman signals at 1447 cm^{-1} and 785 cm^{-1} (I_{1447}/I_{785}), for leukocytes, monocytes and granulocytes.*

The good classification results provided by the empirical analysis can be further increased with PCA analysis. Indeed, a very good separation of the three leukocyte subgroups can be achieved by considering the first three PCs. I selected the PC1, PC2 and PC3 as they describe about 73%, 13% and 11% respectively of the total spectral variance. The relative score plot is presented in Figure 52 and clearly it reveals that the three cell populations formed distinct and well defined groups. Finally, the classification model was built with 300 spectra and cross-validated by leaving out each time one spectrum of the entire set. The results are shown in the confusion matrix of Table 8. Out of the totally 100 lymphocytes spectra, 95 spectra were assigned correctly, only 5 were misclassified and assigned to the monocytes. For the monocytes, 96 spectra have been assigned correctly and for the granulocytes 98 spectra have been assigned correctly. This yields an accuracy of 96.3%.

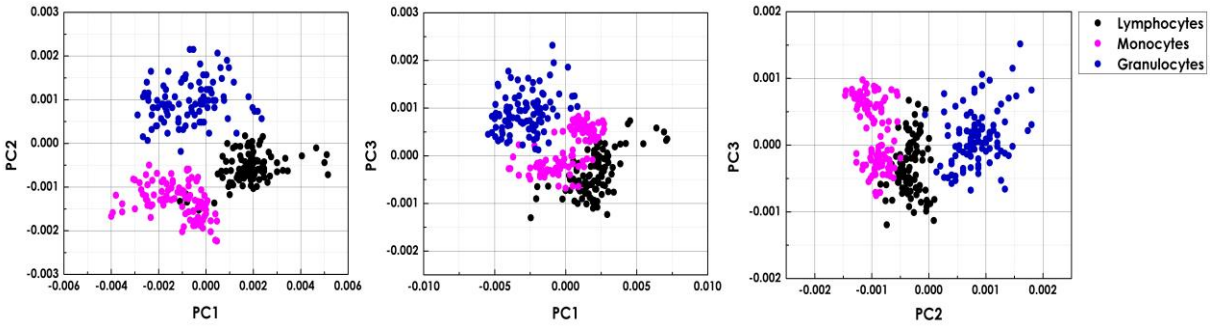

Figure 52: *PCA scatter plot of lymphocytes, monocytes and granulocytes.*

Table 8: *Confusion matrix for the classification of lymphocytes, monocytes and granulocytes.*

	Lymphocytes	Monocytes	Granulocytes
Lymphocytes	95	5	0
Monocytes	4	96	0
Granulocytes	1	1	98

7.4 Raman identification of lymphocytes

This section describes a Raman spectroscopic investigation of human lymphocytes: T cells, B cells and natural killer (NK) cells. T cells (thymus cells) and B cells (bone marrow cells) are the cellular components of the adaptive immune response. T cells are involved in cell-mediated immunity, whereas B cells are involved in antibody-mediated immunity. NK cells are a part of the innate immune system and play an important role in destroying both cancer cells and virally infected cells. NK cells recognize infected cells and cancerous cells by changes of a surface molecule called MHC (major histocompatibility complex) class I [135].

T cells, B cells and natural killer (NK) cells are very similar morphologically and can be identified by their large nucleus. It is impossible to distinguish microscopically between T cells, B cells and NK cells in a peripheral blood smear [136]. Routinely, the flow cytometry procedure is used to determine the percentage of lymphocytes that show specific cell surface proteins (immunoglobulins or CD markers) or that produce particular proteins (cytokines).

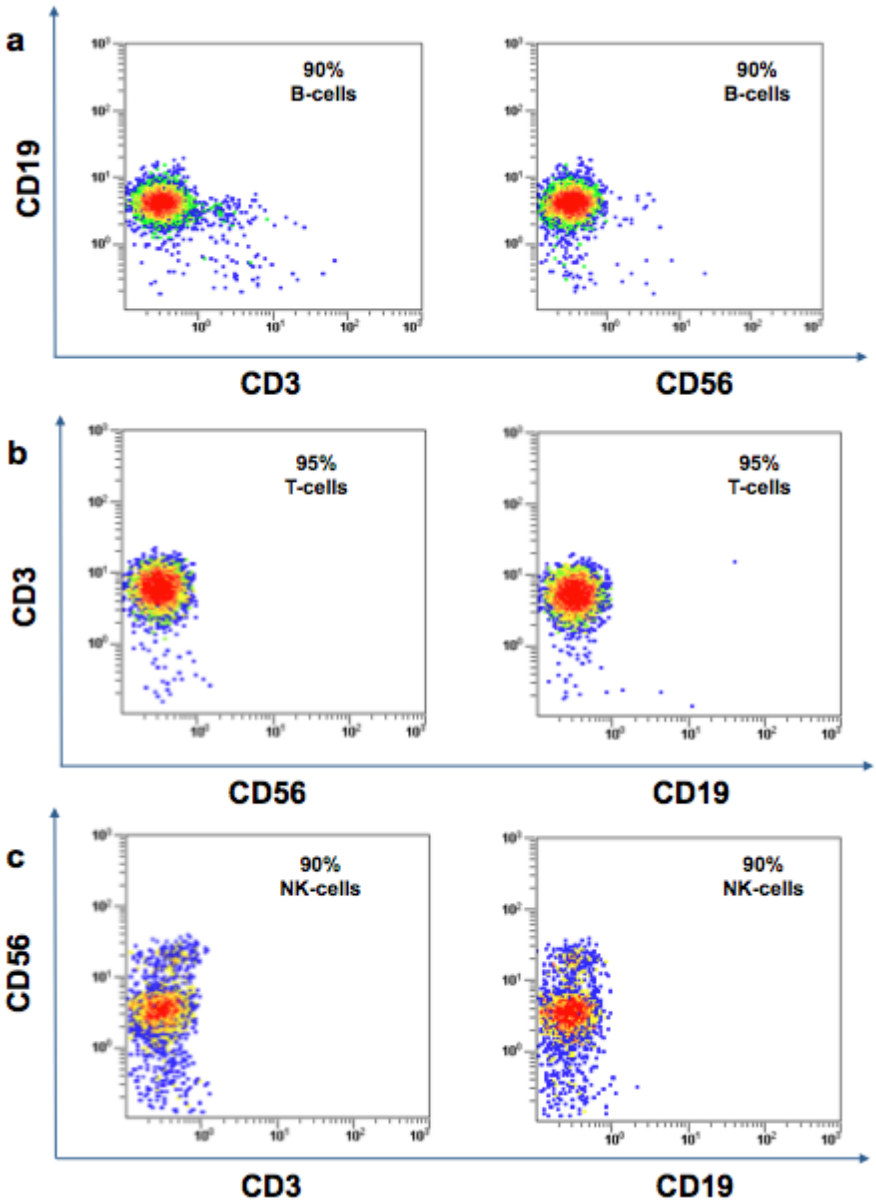

Figure 53: Dot plots for the determination of human lymphocyte purification by flow cytometry. *Percentages of B cells (CD19+/CD3+; CD19+/CD56+), T cells (CD3+/CD56+; CD3+/CD19+) and natural killer cells (CD56+/CD3+; CD56+/CD19+) determined by flow cytometry, after the immunomagnetic separation procedure.*

The lymphocytes samples have been isolated from peripheral blood of three healthy donors (See Chapter 3 for more details). The isolated cells were analysed for purity by flow cytometry. In details, CD19+ B cells were obtained at a purity level of 90% (Figure 53a); CD3+ T cells were obtained at a purity level of 95% (Figure 53b); CD56+ NK cells were obtained at a purity level of 90% (Figure 53c). The fluorescence intensities were measured with a flow cytometer (FC-500; Beckman-Coulter, Milan, Italy),

according to the manufacturer instructions. The percentages of B-cells (CD19+/CD3+; CD19+/CD56+), T-cells (CD3+/CD56+; CD3+/CD19+) NK-cells (CD56+/CD3+; CD56+/CD19+) were assessed after the immunomagnetic separation procedure.

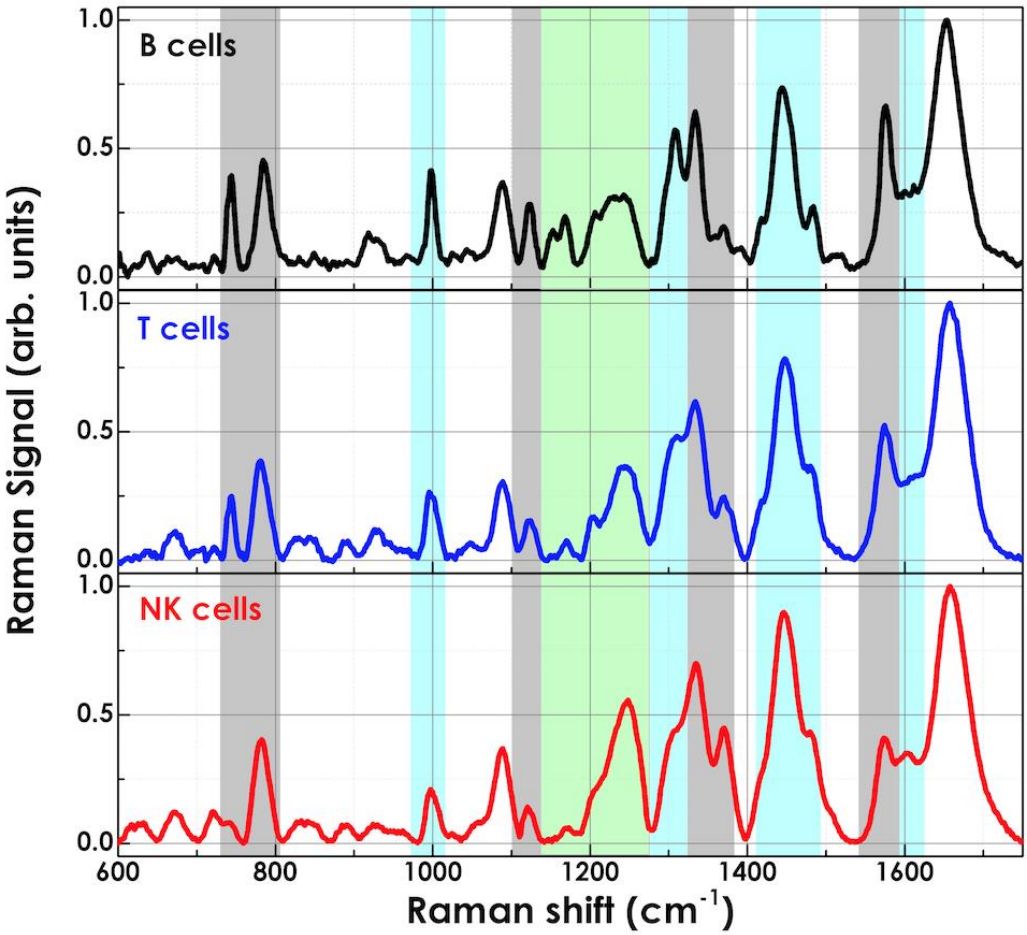

Figure 54: *Mean Raman spectra of B cells, T cells and NK cells.*

The mean Raman spectra on 100 acquisitions of B cells, T cells and NK cells are shown in Figure 54. The spectral profiles confirm that the analysed cell groups are morphological and biochemically very similar. The main differences between B and T cells can be seen in the spectral regions around 1150-1250 cm^{-1} (CN, CC, amide III band, proteins/lipids), 1310 cm^{-1} (amide III band), 1420-1485 cm^{-1} (CH proteins/lipids), 1607-1617 (C=C vibrations) (Figure 54) [13][17][106][120][122]. In this case, the nucleic acid spectral regions are almost invariant. These spectral variations could be due to different expression of specific membrane proteins in B and T cells. The spectral variations it is especially visible by comparing the spectra of T and B cells with NK cells, confirming that NK cells are morphologically different from T and B cells. Indeed, NK

cells present small granules in their cytoplasm containing proteins such as perforin and proteases known as granzymes.

7.5 Lymphocyte statistical evaluations

Finally, I performed PCA to evaluate the discrimination efficiency between the three-lymphocyte subpopulations, according to the RS. Figure 55 shows the PCA scatter plots of the PC1-3 concerning the 100 B cells, 100 T cells and 100 NK cells. The score plots clearly show well-separated and defined cell groups, confirming that our statistical approach allows efficiently identifying even slightly spectral differentiated cell groups. This graphical evaluation is confirmed by the data of the leave-one-out cross validation approach reported in the confusion matrix of Table 9. The mean diagonal values of the confusion matrix provide a total efficiency classification between the three-lymphocyte subpopulations of 94.6%.

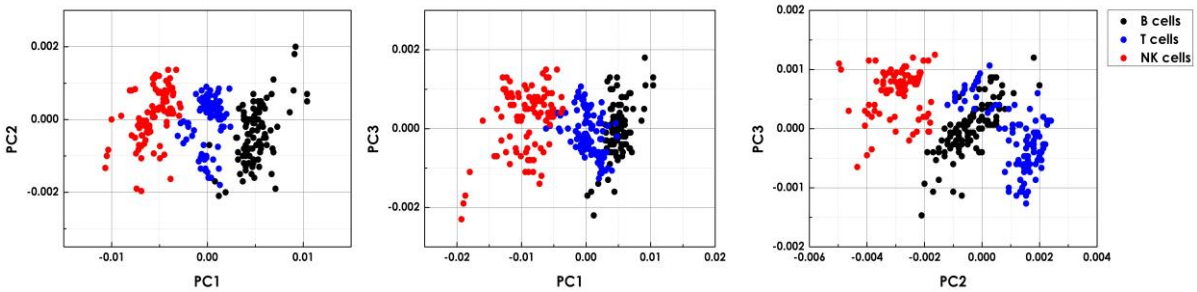

Figure 55: *PCA scatter plots of B cells, T cells and NK cells.*

Table 9: *Confusion matrix for the classification of B cells, T cells and NK cells.*

	B cells	T cells	NK cells
B cells	91	7	2
T cells	5	95	0
NK cells	2	0	98

7.6 Discussion and conclusions

The ability to detect non-disruptively, in completely label-free manner distinct white blood cell subsets would be of significance in both in vivo and in vitro studies of the immune system. In this chapter, I used the Raman spectroscopy to successfully identify a number of important leucocytes subgroups (granulocytes, monocytes and

lymphocytes). One of the major spectral differences between monocytes and lymphocytes are the relative intensities of the nucleic acid and protein vibrational bands: 750 and 785 cm^{-1} DNA bases, 1007 cm^{-1} symmetric ring breathing mode of phenylalanine, 1400-1500 cm^{-1} CH deformation proteins. This can be explained by a much larger nucleus in the lymphocytes, which almost fills the whole cell compared to a smaller indented nucleus in the monocytes. Even more differences were found in the Raman spectra of granulocytes, such as in the regions around 750-800 cm^{-1} and around 830, 980, 1350, 1540 cm^{-1}, due to the strong signal contribution from the myeloperoxidase (MPO), a peroxidase enzyme of the azurophilic granules [130]. Finally, a robust classification model could be built with PCA. This model was tested using the laving-one-out cross validation approach using leucocytes isolated in different days from the peripheral blood of three different healthy donors. Only 11 leucocytes have been misclassified over the 300 analysed giving an overall accuracy of about 97%.

The Raman spectroscopy and PCA combined approach has been additionally used to provide the biochemical signatures that could be used to specifically (up to 95%) identify T cells, B cells and NK cells.

These are very promising results for future spectroscopic assignment of leucocytes subpopulations without the need of any staining solution.

Conclusion

The research presented in this thesis was motivated by the need for label-free characterization methods of cells for diagnostic applications. This work described the development and application of a combination of single-cell Raman spectroscopy (RS) and principal component analysis (PCA) for investigation of leukocytes (hemogram) from peripheral blood of healthy donors as well as the identification and classification of cancer B-ALL cells.

The developed Raman spectroscope has been preliminary validated by analysing three transformed B-leukemia cell lines (RS4;11, REH and MN60) cultured *in vitro*, which are useful model systems to study the pathophysiology of hematopoietic diseases. As these cell lines belong to the human B lymphoid lineage, their Raman spectra appear very similar. However, since RS4;11 and REH are L2 subtype, while MN60 is a L3 B-ALL subtype, their spectra show subtle differences in the intensities of defined Raman peaks. In combination with immunofluorescence and Western blotting, I showed that these Raman markers reflect the relative changes in the potential biological markers from cell surface antigens, cytoplasmic proteins, and DNA content and correlate with the lymphoblastic B-cell maturation/differentiation stages. Additionally, the magnitude of the peak variations increased from the RS4;11 cells to the MN60 cells, in agreement with the extent of expression of plasma-membrane antigens, nucleus/cytoplasm ratio and cytoplasmic immunoglobulins during the B-cell differentiation/maturation process (Figure 30). Of note, the Raman spectrum of the MN60 B-leukemia cells was slightly different from those of both the RS4;11 and REH B-leukemia cells, which also confirmed that these MN60 B-leukemia cells can be classified as a distinct B-leukemia cell subtype, as indeed is the case based on its more differentiated maturation stage. Therefore, the distinctive differences in the Raman spectra between the normal B-lymphocytes and the B-leukemia cells suggests that RS can be used to reveal molecular changes associated with these pathological transformations. I also explored PCA, together with a leave-one-out cross-validation approach, for B-leukemia cell identification and classification, which provided a diagnostic efficiency of 97.3% for separating B-leukemia *versus* normal B-lymphocytes. Notably, only two of 300 control cells were predicted incorrectly, and five of the B-leukemia cells were incorrectly

assigned to the normal B-lymphocyte group (Figure 32), and therefore the risk of false positives with this model appears to be minimal.

The detection and classification of leukemia cells are only the first steps in the clinical management of leukemia patients. Constant cell monitoring of the chemotherapy effect could be crucial for improving treatment strategies and for the detection of minimal residual disease. For this purpose, I focused the present study on the maintenance therapies for patients with B-ALL, with the aim to suppress the drug-resistant population of B-leukemia cells. Using independent and complementary approaches, as immunofluorescence, Western blotting and RS, I identified some biological features that were modified under these B-ALL specific maintenance therapies (Figure 36, Figure 37, Figure 38). Of note, low-dose treatments were used here to better analyze the accuracy of our approaches for the detection of these specific biochemical changes. In more detail, under both MTX and 6MP treatments, all three of these B-leukemia cell lines showed B-leukemia regression through the reversing of the B-cell differentiation/maturation process, which was identified and classified according to the specific antigen expression profiles, and promoted changes in the nucleic acid contents without any apoptotic effects. These specific modifications should be explained by the mechanisms of action of the chemotherapeutic drugs used in this study. Interestingly, both MTX and 6MP treatments similarly affected the Raman spectra of these three B-leukemia cells, with reduced intensities of peaks related to DNA, RNA and protein content. To demonstrate the specific ability of this RS approach for the detection of the anti-leukemic effects of MTX and 6MP treatments on these B-leukemia cells we used ATRA treatment as a control. The Raman spectra of the ATRA-treated and nontreated B-leukemia cells did not show any significant differences.

Additionally, the PCA scatter plots and the cross-validation data demonstrated that although the MTX-treated (or 6MP-treated) B-leukemia cells showed reduced expression of plasma membrane antigens and DNA, their spectra could be separated from the normal B-lymphocytes with an efficiency of about 99%. These findings confirmed that specific Raman markers could be used to discriminate normal from both leukemia cells and leukemia cells under maintenance treatment and suggested that RS could be used in the detection of minimal residual disease.

I additionally extended the Raman approach to three clinical patient samples. Two patients had the preliminary classification of ‘common B-ALL’, the third patient was preliminary classified in between the pro-B and pre-B maturation stages. The distinctive differences in the Raman spectra between the normal and the clinical samples confirmed and further reinforced these observations. I also performed PCA with these clinical

samples. From this PCA analysis, several considerations arose: (i) the spectral variability in these clinical samples was more pronounced compared to the B-leukemia cell lines; (ii) the REH B-leukemia cell data fell within a smaller region defined by the B-ALL cells from Pt-1 and Pt-2; (iii) the data for the B-ALL cells from Pt-3 showed better demarcation from normal B-lymphocytes, and thus these B-ALL cells from Pt-3 were more differentiated than those from Pt-1 and Pt-2, and showed an intermediate behavior to that of the REH and MN60 B-leukemia cell lines; and (iv) RS can be used to differentiate between normal B-lymphocytes and clinical samples from patients with B-ALL with high sensitivity and specificity. In more detail, the PCA algorithm achieved identification of each pathological clinical sample with a sensitivity from 88% to 94% and a specificity from 85% to 90%. These sensitivity and specificity data in this diagnosis provided by RS can now set the stage for more specific clinical studies.

Finally, I showed that RS has been able to identify and distinguish leukocytes. In this proof-of-principle study, I focused on the most important white blood cells populations isolated from peripheral blood of several human volunteers via conventional flow cytometry: granulocytes (neutrophils), monocytes and lymphocytes (T cells, B cells and NK cells). I demonstrated the capability of Raman spectroscopy in the identification and classification of leukocytes and, more in details, of the three lymphocytes groups (Figure 49, Figure 54). With the aid of statistical models, it was possible to discriminate between cell types based on the specific information present in the Raman spectra. The high identification accuracy (about 97%) indicates that the heterogeneity due to person-to-person variability and sample preparations on different days has minimum influence.

In conclusion, this study shows that RS and PCA allow differentiation between normal B-lymphocytes and B-ALL cells at different maturation stages, which has important implications for clinical practice. The feature-rich and specific Raman spectra offers the possibility of highly multi-parameter measurements that could represent a major step forward towards the realization of a non-destructive, label-free Raman-based flow cytometer for blood cell identification. Further studies with both clinical samples before and after chemotherapy treatment will still be needed to understand the potential limitations of this RS approach.

References

[1] Zhou, Y. et al., “Advances in the molecular pathobiology of B-lymphoblastic leukemia”, Human Pathology 43, 1347–1362 (2012).

[2] Brearley, R., Johnson, S.A., Lister, T.A., “Acute lymphoblastic leukaemia in adults: clinicopathological correlations with the french-american-british (fab) co-operative group classification”, Eur J Cancer 15, 909–914 (1979).

[3] Vardiman, J.W. et al., “The 2008 revision of the world health organization (who) classification of myeloid neoplasms and acute leukemia: rationale and important changes”, Blood 114, 937–951 (2009).

[4] Neugebauer, U., Clement, J.H., Bocklitz, T., Krafft, C., Popp, J., “Identification and differentiation of single cells from peripheral blood by Raman spectroscopic imaging”, J Biophoton 3, 579-587 (2010).

[5] Kong, K., Kendall, C., Stone, N., Notingher, I., “Raman spectroscopy for medical diagnostics - From in-vitro biofluid assays to in-vivo cancer detection”, Adv Drug Deliv Rev 89, 121-34 (2015).

[6] Baena, J.R., and Lendl, B., “Raman spectroscopy in chemical bioanalysis,” Curr. Opin Chem Biol 8, 534–539 (2004).

[7] Shetty, G., Kendall, C., Shepherd, N., Stone, N., Barr, H., “Raman spectroscopy: elucidation of biochemical changes in carcinogenesis of oesophagus”, Br J Cancer 94, 1460-1464 (2006).

[8] Krishna, C.M. et al., “Raman spectroscopy studies for diagnosis of cancers in human uterine cervix”, Vib Spectrosc 41, 136-141 (2006).

[9] Utzinger, U. et al., “Near-infrared Raman spectroscopy for in vivo detection of cervical precancers”, Appl Spectrosc 55, 955-959 (2001).

[10] Molckovsky, A., Song, L.M., Shim, M.G., Marcon, N.E., Wilson, B.C., “Diagnostic potential of near-infrared Raman spectroscopy in the colon: differentiating adenomatous from hyperplastic polyps”, Gastrointest Endosc 57, 396-402 (2003).

[11] Konga, K. et al., “Diagnosis of tumors during tissue-conserving surgery with integrated autofluorescence and Raman scattering microscopy”, Proc Natl Acad Sci USA 110, 15189–15194 (2013).

[12] Haka, A.S. et al., “Diagnosing breast cancer by using Raman spectroscopy”, Proc Natl Acad Sci USA 102, 12371–12376 (2005).

[13] Canetta, E. et al., “Modulated Raman spectroscopy for enhanced identification of bladder tumor cells in urine samples”, J Biomed Opt 16, 037002 (2011).

[14] Mariani, M.M. et al., “Micro-Raman detection of nuclear membrane lipid fluctuations in senescent epithelial breast cancer cells”, Anal Chem 82, 4259–4263 (2012).

[15] Chan, J.W., “Recent advances in laser tweezers Raman spectroscopy (ltrs) for label-free analysis of single cells”, J Biophoton 6, 36–48 (2013).

[16] Neugebauer, U., Clement, J.H., Bocklitz, T., Krafft, C., Popp, J., “Identification and differentiation of single cells from peripheral blood by Raman spectroscopic imaging”, J Biophoton 3, 579-587 (2010).

[17] Chan, J.W. et al., “Non-destructive identification of individual leukemia cells by laser trapping Raman spectroscopy”, Anal Chem 80, 2180-2187 (2008).

[18] Eaves, C.J., “Hematopoietic stem cells: concepts, definitions, and the new reality”, Blood, 125(17), 2605–2613 (2015).

[19] Morrison, J., Kimble, J., "Asymmetric and symmetric stem-cell divisions in development and cancer", Nature 441, 1068–74 (2006).

[20] Foon, K.A., and Todd, R.F. 3d, “Immunologic classification of leukemia and lymphoma”, Blood 68 (1), 1-31 (1986).

[21] Bennet, J.M. et al., “Proposals for the classification of the acute leukaemias. French-american- british (fab) co-operative group”, Br J Haematol 33, 451–458 (1976).

[22] Peters, J.M., Ansari, M.Q., “Multiparameter flow cytometry in the diagnosis and management of acute leukemia”, Arch Pathol Lab Med 135, 44–54 (2011).

[23] Noto, R.D., Mirabelli, P. & Vecchio, L.D., “Flow cytometry analysis of acute promyelocytic leukemia: the power of surface hematology”, Leukemia 21, 4–8 (2007).

[24] Cortes J, Albitar M., “In Atlas of Cancer”, edited by M Markman and M Kalaycio. Philadelphia, Current Medicine, 2002.

[25] Kusenda, J., Fajtova, M. & Kovarikova, A., “Monitoring of minimal residual disease in acute leukemia by multiparametric flow cytometry”, Neoplasma 61, 119–127 (2014).

[26] Walter, R.B. et al., “Impact of pretransplantation minimal residual disease, as detected by multiparametric flow cytometry, on outcome of myeloablative hematopoietic cell transplantation for acute myeloid leukemia”, J Clin Oncol 29, 1190–1197 (2011).

[27] Al-mawali, A., Gillis, D. & Lewis, I., “The role of multiparameter flow cytometry for detection of minimal residual disease in acute myeloid leukemia”, Am J Clin Pathol 131, 16–26 (2009).

[28] Paspaliaris, B., Pamio, M. & Savige, J., “Indirect immunofluorescence (iif) of normal washed peripheral blood cells to demonstrate antineutrophil cytoplasmic antibodies (anca)”, J Clin Pathol 53, 774–777 (2000).

[29] Faulds, K., Barbagallo, R.P., Keer, J.T., Smith, W.E., Graham, D., “SERRS as a more sensitive technique for the detection of labelled oligonucleotides compared to fluorescence”, Analyst 129, 567–568 (2004).

[30] Smekal, A., “Zur quantentheorie der dispersion”, Naturwiss 11, 873-875 (1923).

[31] Raman, C.V., and Krishnan, K.S., “A New Type of Secondary Radiation”, Nature 121, 501–502 (1928).

[32] Landsberg, G., and Mandelstam, L., “A novel effect of light scattering in crystals”, Naturwissenchaften 16, 557–558 (1928).

[33] Spiro, T.G., “Resonance Raman spectroscopy as a probe of heme protein structure and dynamics”, Adv Protein Chem 37, 111-159 (1985).

[34] Kataoka, H., Maeda, S., and Hirose, C., “Effects of Laser Linewidth on the Coherent Anti-Stokes Raman Spectroscopy Spectral Profile,” Appl Spectrosc 36, 565 (1982).

[35] Braiman, M., and Mathies, R., “Resonance Raman spectra of bacteriorhodopsin’s primary photoproduct: evidence for a distorted 13-cis retinal chromophore,” PNAS 79, 403 (1982).

[36] Mahadevan-Jansen, A., Richards-Kortum, R., “Raman spectroscopy for the detection of cancers and precancers”, J Biomed Opt 1, 31-70 (1996).

[37] Duguid, J., Bloomfield, V.A., Benevides, J., and Thomas, G.J., “Raman spectroscopy of DNA-metal complexes. I. Interactions and conformational effects of the divalent cations: Mg, Ca, Sr, Ba, Mn, Co, Ni, Cu, Pd, and Cd”, Biophys J 65, 1916 (1993).

[38] Puppels, G.J., de Mul. F.F.M., Otto, C. Greve, J., Robert-Nicoud, M., Arndt-Jovin, D.J., and Jovin, T.M., “Studying single living cells and chromosomes by confocal Raman microspectroscopy,” Nature 347, 301 (1990).

[39] Shim, M.G., Wilson, B.C., Marple, E., and Wach, M., “Study of Fiber-Optic Probes for in Vivo Medical Raman Spectroscopy”, Appl Spectrosc 53, 619 (1999).

[40] Jorio, A., Saito, R., Hafner, J.H., Lieber, C.M., Hunter, M., McClure, T., Dresselhaus, G., and Dresselhaus, M.S., “Structural (n,m) Determination of Isolated Single-Wall Carbon Nanotubes by Resonant Raman Scattering”, Phys Rev Lett 86, 1118 (2001).

[41] Walker, S., and Straw, H., “Spectroscopy2: Ultra-violet, vVisible, Infra-red and Raman spectroscopy”, Chapman & Hall, London (1962).

[42] Demtroder, W., “Laser spectroscopy,” Springer, 1996. R. Loudon, “The quantum theory of light”, Clarendon press-Oxford (1997).

[43] Herzberg, G., “Molecular Spectra and Molecular structure”, van Nostrand Reinhold, New York (1945).

[44] Weber, A., “Raman spectroscopy of gases and liquids”, Topics Curr Phys, Springer 11 (1979).

[45] Byrne, H. J., Knief, P., Keating, M.E., Bonnier, F., “Spectral pre and post processing for infrared and Raman spectroscopy of biological tissues and cells”, Chem Soc Rev, 45, 1865 (2016).

[46] Schrader, B., “Infrared and Raman Spectroscopy - Methods and Applications”, VCH, Weinheim, DM 298 (1995).

[47] PerkinElmer, Inc., “An Introduction to Fluorescence Spectroscopy” (2000).

[48] Xie, C.A., Li, Y.Q., “Confocal micro-Raman spectroscopy of single biological cells using optical trapping and shifted excitation difference techniques”, J Appl Phys 93, 2982–2986 (2003).

[49] Notingher, I., “Raman spectroscopy cell-based biosensors”, Sensors 7, 1343–1358 (2007).

[50] Gremlich, H.U., and Yan, B., “Infrared and Raman spectroscopy of biological materials”, CRC Press vol. 24, New York (2000).

[51] Koljenovic, S., "Towards Clinico-Pathological Application of Raman Spectroscopy", Erasmus Universiteit Rotterdam (2008).

[52] Reisner, L.A., et al., "A prototype biosensor-integrated image-guided surgery system", Int J Med Robotics Comput Assist Surg 3, 82-88 (2007).

[53] Short, K.W., et al., "Raman Spectroscopy Detects Biochemical Changes Due to Proliferation in Mammalian Cell Cultures", Biophys J 88, 4274-4288 (2005).

[54] Harvey, T.J., et al., "Classification of fixed urological cells using Raman tweezers", J Biophoton 2, 47–69 (2009).

[55] Chan, J.W., et al., "The effect of cell fixation on the discrimination of normal and leukemia cells with laser tweezers Raman spectroscopy", Biopolymers 91, 132-139 (2009).

[56] Schuster, K.C., et al., "Single-cell analysis of bacteria by Raman microscopy: spectral information on the chemical composition of cells and on the heterogeneity in a culture", Journal of Microbiological Methods 42, 29-38 (2000).

[57] Swain, R.J., et al., "Non-invasive analysis of cell cycle dynamics in single living cells with Raman micro-spectroscopy", Journal of Cellular Biochemistry 104, 1427-1438 (2008).

[58] Notingher, I., et al., "New detection system for toxic agents based on continuous spectroscopic monitoring of living cells", Biosensors & Bioelectronics 20, 780-789 (2004).

[59] Puppels, G.J., et al., "Studying single living cells and chromosomes by confocal Raman microspectroscopy", Nature 347, 301-303 (1990).

[60] Uzunbajakava, N., et al., "Nonresonant confocal Raman imaging of DNA and protein distribution in apoptotic cells", Biophysical Journal 84, 3968-81 (2003).

[61] Notingher, I., et al., "Discrimination between ricin and sulphur mustard toxicity in vitro using Raman spectroscopy", Journal of the Royal Society Interface 1, 79-90 (2004).

[62] Verrier, S., et al., "In situ monitoring of cell death using Raman microspectroscopy", Biopolymers 74, 157-162 (2004).

[63] Hamaguchi, H., "Linear and Non-Linear Raman Spectroscopy and Imaging of Living Cells; Life and Death at the Cellular Level", Pacific Rim Conference on Lasers and Electro-Optics, 191-192 (2007).

[64] Owen, C.A., et al., "In vitro toxicology evaluation of pharmaceuticals using Raman micro-spectroscopy", Journal of Cellular Biochemistry 99, 178-186 (2006).

[65] Brown, K.L., et al., "Raman spectroscopic differentation of activated versus non-activated T lymphocytes: An in vitro study of an acute allograft rejection model", Journal of Immunological Methods 340, 48-54 (2008).

[66] Notingher, I., and Hench, L.L., "Raman microspectroscopy: a noninvasive tool for studies of individual living cells in vitro", Expert Review of Medical Devices 3, 215-234 (2006).

[67] Harz, M., et al., "Vibrational spectroscopy- a powerful tool for the rapid identification of microbial cells at the single-cell level," Cytometry A 75, 104-113 (2009).

[68] Chen, J.W., et al., "Detection of adenosine using surface-enhanced Raman scattering based on structure-switching signaling aptamer", Biosensors & Bioelectronics 24, 66-71 (2008).

[69] Fujita, K., and Smith, N., "Label-free molecular imaging of living cells", Molecules and Cells 26, 530-535 (2008).

[70] Wachsmann-Hogiu, S., et al., "Chemical analysis in vivo and in vitro by Raman spectroscopy-from single cells to humans", Current Opinion in Biotechnology 20, 63-73 (2009).

[71] Swain, R., and Stevens, M., "Raman microspectroscopy for non-invasive biochemical analysis of single cells", Biochemical Society Transactions 35, 544-549 (2007).

[72] Movasaghi, Z., et al., "Raman spectroscopy of biological tissues", Applied Spectroscopy Reviews 42, 493-541 (2007).

[73] Choo-Smith, L. P., Edwards, H. G. M., Endtz, H. P., Kros, J. M., Heule, F., Barr, H., Robinson, J. S., Bruining, H. A. and Puppels, G. J., "Medical applications of Raman spectroscopy: From proof of principle to clinical implementation", Biopolymers 67. 1–9 (2002).

[74] Huang, Z., McWilliams, A., Lui H., McLean, D.I., Lam, S., Zeng, H., "Near-infrared Raman spectroscopy for optical diagnosis of lung cancer", Int J Cancer 107, 1047–1052 (2003).

[75] Haka, A.S., Shafer-Peltier, K.E., Fitzmaurice, M., et al., "Diagnosing breast cancer by using Raman spectroscopy", Proc Natl Acad Sci USA 102, 12371-6 (2005).

[76] Ghomi, M., "Applications of Raman Spectroscopy to Biology", Advances in Biomedical Spectroscopy 5 (2012).

[77] Halina Abramczyk and Beata Brozek-Pluska, "Raman Imaging in Biochemical and Biomedical Applications. Diagnosis and Treatment of Breast Cancer", Chem Rev 113 (8), 5766–5781 (2013).

[78] Anuradha Ramoji, Ute Neugebauer , Thomas Bocklitz , Martin Foerster , Michael Kiehntopf Michael Bauer and Jürgen Popp, "Toward a Spectroscopic Hemogram: Raman Spectroscopic Differentiation of the Two Most Abundant Leukocytes from Peripheral Blood", Anal Chem 84 (12), 5335–5342 (2012).

[79] De Luca, A.C., et al. Reproducible surface-enhanced Raman quantification of biomarkers in multicomponent mixtures. ACS Nano 8, 2575–2583 (2014).

[80] De Luca, A.C., et al., "Non-invasive sex assessment in bovine semen by Raman spectroscopy", Laser Phys Lett 11, 055604(1-8) (2014).

[81] Stong, R.C., Korsmeyer, S.J., Parkin, J.L., Arthur, D.C., Kersey, J.H., "Human acute leukemia cell line with the t(4;11) chromosomal rearrangement exhibits b lineage and monocytic characteristics", Blood 65, 21–31 (1985).

[82] Rosehfeld, C. et al., "Phenotypic characterisation of a unique non-T, non-B acute lymphoblastic leukaemia cell line", Nature 267, 841–843 (1977).

[83] Craig, F.E., Foon, K.A., "Flow cytometric immunophenotyping for hematologic neoplasms", Blood 111, 3941–3967 (2008).

[84] Mahadevan-Jansen, A., Richards-Kortum, R., "Raman spectroscopy for the detection of cancers and precancers" J Biomed Opt 1, 31-70 (1996).

[85] Collins, S.J., Ruscetti, F.W., Gallagher, R.E., Gallo, R.C., "Terminal differentiation of human promyelocytic leukemia cells induced by dimethyl sulfoxide and other polar compounds", Proc Natl Acad Sci 75, 2458-2462 (1978).

[86] Dumont, N., Aubin, E., Proulx, D.P., Lemieux, R., Bazin, R., "Increased secretion of hyperimmune antibodies following lipopolysaccharide stimulation of CD40-activated human B cells in vitro", Immunology 126, 588-595 (2008).

[87] Mc Creery, R.L., "Raman Shift Frequency Standards: Polystyrene", http://www.chem.ualberta.ca/~mccreery/ramanmaterials.html.

[88] Johnson, R.A., Wichem, D.W., "Applied Multivariate Statistical Analysis, 6th Edition", Pearson (2008).

[89] Canetta, E. et al., "Modulated Raman spectroscopy for enhanced identification of bladder tumor cells in urine samples", J Biomed Opt 16, 037002 (2011).

[90] The, S.K. et al., "Raman spectroscopy for precancer disgnosis of stomach", Br J Cancer 98, 457- 465 (2008).

[91] Fritschy, J. M., Härtig. W., "Immunofluorescence", eLS (2001).

[92] Tahrin Mahmood, Ping-Chang Yang, "Western Blot: Technique, Theory, and Trouble Shooting", N Am J Med Sci 4(9), 429–434 (2012).

[93] BD Biosciences, "Introduction to Flow Cytometry: A Learning Guide, Manual Part Number: 11-11032-01" (2000).

[94] Shapiro, H.M., "Practical flow cytometry. 4th edition", Wiley-Liss (2003).

[95] Jennings, D.C., and Foon, K.A., "Recent Advances in Flow Cytometry: Application to the Diagnosis of Hematologic Malignancy", Blood 90 (8), 1997.

[96] Haka, A. et al., "In vivo margin assessment during partial mastectomy breast surgery using RS", Cancer Res 66, 3317–3322 (2006).

[97] Chyan, W., Zhang, Y.Z., Lippard, S.J., Radford, R.J., "Reaction-based fluorescent sensor for investigating mobile zn2+ in mitochondria of healthy versus cancerous prostate cells", Proc Natl Acad Sci USA 111, 143–148 (2014).

[98] Gaedicke, S., et al., "Noninvasive positron emission tomography and fluorescence imaging of cd133+ tumor stem cells", Proc Natl Acad Sci USA 111, E692– E701 (2014).

[99] Agrawal, A., Deo, R., Wang, G.D., Wang, M.D., Nie, S., “Nanometer-scale mapping and single-molecule detection with color-coded nanoparticle probes”, Proc Natl Acad Sci USA 105, 3298–3303 (2008).

[100] Schultz, S., Smith, D.R., Mock, J.J., Schultz, D.A., “Single-target molecule detection with nonbleaching multicolor optical immunolabels”, Proc Natl Acad Sci USA 97, 996–1001 (2000).

[101] Perrault, S.D., Chan, W.C.W., “In vivo assembly of nanoparticle components to improve targeted cancer imaging”, Proc Natl Acad Sci USA 107, 11194–11199 (2010).

[102] Jungst, C., Klein, M., Zumbusch, A., “Long-term live cell microscopy studies of lipid droplet fusion dynamics in adipocytes”, J Lipid Res 54, 3419–3429 (2013).

[103] Kosmeier, S., et al., “Nonredundant Raman imaging using optical eigenmodes”, Optica 1, 257–263 (2014).

[104] Raman, C.V. & Krishnan, K.S., “A new type of secondary radiation”, Nature 121, 501–502 (1928).

[105] Klein, K., et al., “Label-free live-cell imaging with confocal Raman microscopy”, Biophys J 102, 360–368 (2012).

[106] Nothingher, I., Verrier, S., Haque, S., Polak, J.M., Hench, L.L., “Spectroscopic study of human lung epithelial cells (a549) in culture: living cells versus dead cells”, Biopolymers 72, 230–240 (2003).

[107] Neugebauer, U., Heinemann, S.H., Schmitt, M., Popp, J., “Combination of patch clamp and Raman spectroscopy for single-cell analysis”, Anal Chem 83, 344–350 (2011).

[108] Wu, H., et al., “In vivo lipidomics using single-cell Raman spectroscopy”, Proc Natl Acad Sci USA 108, 3809–3814 (2011).

[109] Rusciano, G., De Luca, A.C., Pesce, G., Sasso, A., “Raman tweezers as a diagnostic tool of hemoglobin-related blood disorders”, Sensors 8, 7818–7832 (2008).

[110] De Luca, A.C., et al., “Spectroscopical and mechanical characterization of normal and thalassemic red blood cells by Raman tweezers”, Opt Express 16, 7943–7957 (2008).

[111] Okada, M., et al., “Label-free Raman observation of cytochrome c dynamics during apoptosis”, Proc Natl Acad Sci USA 109, 28–32 (2012).

[112] Ichimura, T., et al., “Visualizing cell state transition using Raman spectroscopy”, PloS ONE 9, e84478 (2014).

[113] Calvo, K.R., Mccoy, C.S., Stetler-Stevenson, M., “Methods in molecular biology”, Methods Mol Biol 699, 295–316 (2010).

[114] Drexler, H.G., Macleod, R.A., “History of leukemia-lymphoma cell lines”, Human Cell 23, 75–82 (2010).

[115] Roos, G., et al., “Establishment and characterization of a human ebv-negative B cell line (MN 60)”, Leuk Res 6, 685–693 (1982).

[116] Bene, M. C., et al., “Proposals for the immunological classification of acute leukemias. European group for the immunological characterization of leukemias (egil)”, Leukemia 9, 1783–1786 (1995).

[117] Loken, B.M.R., Shah, V., Dattilio, K.L., Curt, C., “Flow cytometric analysis of human bone marrow. II. Normal B lymphocyte development”, Blood 70, 1316–1324 (1987).

[118] Durig, J., et al., “CD38 expression is an important prognostic marker in chronic lymphocytic leukaemia”, Leukemia 16, 30–35 (2002).

[119] Jess, P.R., Mazilu, M., Dholakia, K., Riches, A.C., Herrington, C.S., “Optical detection and grading of lung neoplasia by Raman microspectroscopy”, Int J Cancer 124, 376–380 (2009).

[120] Chan, J.W., et al. Micro-Raman spectroscopy detects individual neoplastic and normal hematopoietic cells. Biophys. J. 90, 648–656 (2006).

[121] Stone, N., Kendall, C., Smith, J., Crow, P., Barr, H., “Raman spectroscopy for identification of epithelial cancers”, Faraday Discuss 126, 141–157 (2004).

[122] Johnson, R.A., Wichem, D.W., “Applied Multivariate Statistical Analysis, 6th Edition”, (2007).

[123] Yao, H., et al., “Raman spectroscopic analysis of apoptosis of single human gastric cancer cells”, Vib Spectrosc 50, 193-197 (2008).

[124] Matthews, Q., Jirasek, A., Lum, J., Duan, X., Brolo, A.G., “Variability in Raman spectra of single human tumor cells cultured in vitro: correlation with cell cycle and culture confluency”, Appl Spectrosc 64, 871-887 (2010).

[125] Venuat, A.M., Testu, M.J., Rosenfeld, C., “Cytogenetic abnormalities in a human null cell leukemia line (REH)”, Cancer Genet Cytogenet 3, 327–334 (1981).

[126] Nair, S.S., Kumar, R., “Chromatin remodeling in cancer: A gateway to regulate gene transcription”, Mol Oncol 6, 611–619 (2012).

[127] Loffler, H., Gassmann, W., “Morphology and cytochemistry of acute lymphoblastic leukaemia”, Baillieres Clin Haematol 7, 263- 72 (1994).

[128] Lin, T., et al., “Induction of acute lymphocytic leukemia differentiation by maintenance therapy”, Leukemia 21, 1915–1920 (2007).

[129] Puppels, G.J., Garritsen, H.S.P., Segers-Nolten, G.M.J., de Mul, F.F.M., Greve, J., “Raman microspectroscopic approach to the study of human granulocytes”, Biophys J 60, 1046-1056 (1991).

[130] Fotoohi, A.K., Albertioni, F., “Mechanisms of antifolate resistance and methotrexate efficacy in leukemia cells”, Leuk Lymphoma 49, 410-26 (2008).

[131] Schmiegelow, K., Nielsen, S.N., Frandsen, T.L., Nersting, J., “Mercaptopurine/Methotrexate maintenance therapy of childhood acute lymphoblastic leukemia: clinical facts and fiction”, J Pediatr Hematol Oncol 36, 503-17 (2014).

[132] Mahadevan-Jansen, A., Richards-Kortum, R., “Raman spectroscopy for the detection of cancers and precancers”, J Biomed Opt 1, 31-70 (1996).

[133] The, S.K. et al., “Raman spectroscopy for precancer diagnosis of stomach”, Br J Cancer 98, 457-465 (2008).

[134] Sibbett, S. S., and J. K. Hurst, “Structural analysis of myeloperoxidase by resonance Raman spectroscopy”, Biochemistry 23, 3007-3013. Bolscher, B.G.J.M. (1986).

[135] Janeway, C.A. Jr, Travers, P., Walport, M., and Shlomchik, M.J., “Immunobiology, 5th edition The Immune System in Health and Disease”, Garland Science, New York (2001).

[136] Abbas, A.K., and Lichtman, A.H., “Cellular and Molecular Immunology (5th ed.)”, Saunders, Philadelphia, (2003).

List of publications

Publications related to PhD research activity

1. A reliable Raman-spectroscopy-based approach for diagnosis, classification and follow-up of B-cell acute lymphoblastic leukemia

S. Managò, C. Valente, P. Mirabelli, D. Circolo, F. Basile, D. Corda, A. C. De Luca

Scientific Reports (accepted 9 March 2016)

ABSTRACT

Acute lymphoblastic leukemia type B (B-ALL) is a neoplastic disorder that shows high mortality rates due to immature lymphocyte B-cell proliferation. B-ALL diagnosis requires identification and classification of the leukemia cells. Here, we demonstrate the use of Raman spectroscopy to discriminate normal lymphocytic B- cells from three different B-leukemia transformed cell lines (i.e., RS4;11, REH, MN60 cells) based on their biochemical features.

Our study demonstrates the potential of this technique for classification of B-leukemia cells into the different differentiation/maturation stages, as well as for the identification of key biochemical changes under chemotherapeutic treatments. Finally, preliminary results from clinical samples indicate high consistency of, and potential applications for, this Raman spectroscopy approach.

Other publications

2. Non-invasive sex assessment in bovine semen by Raman spectroscopy

A. C. De Luca, S. Managò, M. A. Ferrara, L. Sirleto, R. Puglisi, D. Balduzzi, A. Galli, I. Rendina, P. Ferraro, G. Coppola

Laser Physics Letters, Volume 11, Number 5 (2014)

ABSTRACT

X- and Y-chromosome-bearing sperm cell sorting is of great interest, especially for animal production management systems and genetic improvement programs. Here, we demonstrate an optical method based on Raman spectroscopy to separate X- and Y-chromosome-bearing sperm cells, overcoming many of the limitations associated with current sex-sorting protocols. A priori Raman imaging of bull spermatozoa was utilized to select the sampling points (head-neck region), which were then used to discriminate cells based on a spectral classification model. Main variations of Raman peaks associated with the DNA content were observed together with a variation due to the sex membrane proteins. Next, we used principal component analysis to determine the efficiency of our device as a cell sorting method. The results (>90% accuracy) demonstrated that Raman spectroscopy is a powerful candidate for the development of a highly efficient, non-invasive, and non-destructive tool for sperm sexing.

3. Label-free imaging and biochemical characterization of bovine sperm cells

M. A. Ferrara, G. Di Caprio, S. Managò, A. De Angelis, L. Sirleto, G. Coppola, A. C. De Luca

Biosensors 5(2), 141-157 (2015)

ABSTRACT

A full label-free morphological and biochemical characterization is desirable to select spermatozoa during preparation for artificial insemination. In order to study these fundamental parameters, we take advantage of two attractive techniques: digital holography (DH) and Raman spectroscopy (RS). DH presents new opportunities for studying morphological aspect of cells and tissues non-invasively, quantitatively and without the need for staining or tagging, while RS is a very specific technique allowing the biochemical analysis of cellular components with a spatial resolution in the sub-micrometer range. In this paper, morphological and biochemical bovine sperm cell alterations were studied using these techniques. In addition, a complementary DH and RS study was performed to identify X- and Y-chromosome-bearing sperm cells. We demonstrate that the two techniques together are a powerful and highly efficient tool elucidating some important criterions for sperm morphological selection and sex-identification, overcoming many of the limitations associated with existing protocols.

4. Normal State Optical Features Study of Nd123 and Gd1212 HTSC Materials for Photonics and MetaMaterials Fabrication

S. Managò, A. C. De Luca, I. Rendina, V. Mocella, S. Romano, G. Carapella, R. Ciancio, M. Gombos

IEEE Transactions on Applied Superconductivity, Volume PP, Issue 99 (2016)

ABSTRACT

YBCO-like Nd123 and Gd1212 superconductors in the normal state, in visible and infrared regime, have been analyzed in this work.

Superconductors, and particularly High Temperature Superconductors (HTSC), hold indeed a great interest in the highly innovative research field of Metamaterials and Photonics with important applications. Indeed nano-structured devices suffer from the increasing resistivity with frequency in metals, and SC materials provide a viable route to approach this problem. Moreover HTSC are plasmonic materials at nonzero temperature and their features, not available in conventional materials, make them very attractive for metamaterials use.

In particular we investigate Nd123, for its high Tc, and Gd1212 for the coexistence, in its unitary cell, of magnetic order and superconductivity. Samples were extracted from TSG bulk pellets and bars.

FTIR analysis, performed in the far-infrared (FIR) shows articulated peak structures with $k < k_{min}$ and a plateau for higher k, allowing Nd123 and Gd1212 pseudogap measurement.

Raman spectroscopy and microscopy provided a structural mapping of our Nd123 samples, allowing to distinguish superconducting matrix from non-superconducting phases inclusions (precipitates) and providing an instrument to discriminate among optical responses of the different compounds.

Proceedings of conferences

5. A.C. De Luca, S. Managò, M. A. Ferrara, L. Sirleto, R. Puglisi, D. Balduzzi, A. Galli, I. Rendina, P. Ferraro, G. Coppola "Label-free biochemical characterisation of bovine sperm cells using Raman microscopy" Proc. SPIE 8792 (2013).

6. A.C. De Luca, P. Reader-Harris, M. Mazilu, S. Managò, S. Mariggiò, D. Corda, A. Di Falco, "Biomolecular sensing of cancer diagnostic using highly reproducible SERS substrate" Proc. SPIE 8957-8 (2014).

7. A.C. De Luca, S. Managò, M. A. Ferrara, L. Sirleto, R. Puglisi, D. Balduzzi, A. Galli, I. Rendina, P. Ferraro, G. Coppola "Label-free biochemical characterisation of sperm cells using Raman Spectroscopy" Proc. SPIE 8938-42 (2014).

8. S. Managò, G. Coppola, M. A. Ferrara, L. Sirleto, R. Puglisi, D. Balduzzi, A. Galli, I. Rendina, P. Ferraro, A.C. De Luca "Raman Sex Sorting of Bovine Spermatozoa" IEEExplore DOI: 10.1109/Fotonica.2014.6843968 (2014).

9. A.C. De Luca, S. Managò, S. Mariggiò, D. Corda, P. Reader-Harris, M. Mazilu, A. Di Falco. "SERS sensing of cancer biomarkers", IEEExplore DOI:10.1109/Fotonica.2014.6843927 (2014).

10. S. Managò, C. Valente, P. Mirabelli, A.C. De Luca, "Discrimination and classification of acute lymphoblastic leukemia cells by Raman spectroscopy", Proc. SPIE Optical Sensors 2015, 95060Z (2015).

11. A. De Angelis, M.A. Ferrara, G. Di Caprio, S. Managò, L. Sirleto, G. Coppola, A.C. De Luca, “Spermatozoa quality assessment: a combined holographic and Raman microscopy approach”, Proc. SPIE 9529, Optical Methods for Inspection, Characterization, and Imaging of Biomaterials II, 952916 (2015).

12. A. De Angelis, M.A. Ferrara, G. Di Caprio, S. Managò, L. Sirleto, G. Coppola, A.C. De Luca, “A combined holographic and Raman microscopy approach for the assessment of spermatozoa”, IET Digital Library DOI: 10.1049/cp.2015.0167 (2015).

Ringraziamenti

Premesso che non amo sentimentalismi e non considero un lavoro di tesi alla stregua del libro Cuore di de Amicis, in questo caso farò un'eccezione per ringraziare, sinceramente, tutti coloro che hanno condiviso con me questo lungo e intenso percorso di studi.

Ringrazio, innanzitutto, Anna Chiara De Luca, il tutor "tascabile" come osai definirla dopo solo pochi giorni averla conosciuta, ricevendo in cambio un'occhiataccia che non faceva presagire nulla di buono. Ma non è stato così, anzi. E' solo grazie a lei che ho iniziato a muovere i primi passi nel mondo della ricerca e imparato a lavorare con passione e dedizione in laboratorio. Sempre pronta a dare utili consigli e preziosi suggerimenti, a incoraggiarmi con la sua positività e la sua spontaneità, a tirare fuori le giuste motivazioni in ogni situazione. Oltre ad essere una tutor è stata una sorella maggiore. Per tutto questo le sarò sempre grato.

Un grandissimo ringraziamento va anche a Carmen Valente e Peppino Mirabelli, i miei due consulenti di biologia di fiducia. Li ringrazio per la loro appassionata collaborazione, per essere stati sempre pazienti e disponibili nel darmi spiegazioni su tutto ciò che riguardasse la parte biologica del mio lavoro di dottorato. E lo hanno fatto veramente bene perché ho imparato tantissimo da loro, sperando in futuro di poter contare ancora su di loro. E un affettuoso ringraziamento a Diego Circolo, per la meticolosa assistenza tecnica nei laboratori di biologia che ha fatto di me un essere ibrido, a metà tra il fisico e il biologo.

Non possono mancare, infine, i ringraziamenti ai tanti amici e colleghi del CNR con cui ho trascorso tanto tempo insieme negli ultimi tre anni: amici di pranzo e di "pausetta", di partite di calcetto e di terzo tempo in pizzeria, di stadio San Paolo e di commenti "tennico-tattici". L'onnipresente Silvia, l'amica da tempo immemore, che ha sempre da raccontarti almeno 7 cose al giorno...un vero incubo; il mitico Edoardo, una fucina di "stravaganze" e di simpatia, con lui le risate sono all'ordine del giorno; il voluminoso Vito, l'azzeccagarbugli amante della cucina vegetariana e di papiri ercolanesi; la laziale Annalisa, romana de Tivoli, transalpina di adozione, folle pendolare ossessionata dallo spinning e dagli orari della Frecciarossa; la new entry Michela, appassionata di cupcake, torte di zucchero e allestimenti per feste fino a 12 anni; Gaetano, il re della mela annurca, raffinato conoscitore del giuoco del calcio e grande estimatore del Napoli di mister Sarri;

Fabrizio, il “Pobbà” dei poveri, l’ingegnere fasanese alla continua ricerca di se stesso; Alessandro, il bomber della Sila, la risposta calabrese al talento di Van Basten; Jane, il prontuario umano farmaceutico, database vivente di principi attivi e impact factor; Stefania, celebre per il mangiar sano fatto di verdure bollite e succulenti brodini serali; e Shom, l’indiano partenopeo, la cui lingua è un mix di inglese, italiano, bengalese, hindi e, forse, qualche accenno di sanscrito.